5-2010

Theoretical Models for Wall Injected Duct Flows

Tony Saad
University of Tennessee Space Institute, saadtony@gmail.com

To the Graduate Council:

I am submitting herewith a dissertation written by Tony Saad entitled "Theoretical Models for Wall Injected Duct Flows." I have examined the final electronic copy of this dissertation for form and content and recommend that it be accepted in partial fulfillment of the requirements for the degree of Doctor of Philosophy, with a major in Mechanical Engineering.

Joseph Majdalani, Major Professor

We have read this dissertation and recommend its acceptance:

Basil N. Antar, Bruce W. Bomar, Boris A. Kupershmidt, Roy J. Schulz

Accepted for the Council:

Carolyn R. Hodges

Vice Provost and Dean of the Graduate School

(Original signatures are on file with official student records.)

To the Graduate Council:

I am submitting herewith a dissertation written by Tony Saad entitled "Theoretical Models for Wall Injected Duct Flows." I have examined the final electronic copy of this dissertation for form and content and recommend that it be accepted in partial fulfillment of the requirements for the degree of Doctor of Philosophy, with a major in Mechanical Engineering.

Joseph Majdalani, Major Professor

We have read this dissertation
and recommend its acceptance:

Basil N. Antar

Bruce W. Bomar

Boris A. Kupershmidt

Roy J. Schulz

Accepted for the Council:

Carolyn R. Hodges

Vice Provost and Dean of the Graduate School

(Original signatures are on file with official student records.)

Theoretical Models
for
Wall Injected Duct Flows

A Dissertation

Presented for the

Doctor of Philosophy

Degree

The University of Tennessee, Knoxville

Tony Saad

May 2010

I dedicate this dissertation to my parents:

Georgette and Youssef Saad

and to my Godparents:

Lily and Albert Sara

Acknowledgements

I am deeply grateful to my advisor, Dr. Joseph Majdalani, for his guidance and support throughout my graduate research at UTSI. I thank him for sharing with me several ideas that were at the foundation of this dissertation. He introduced me to asymptotic theory and encouraged me to pursue new techniques in analytical modeling. His thorough feedback and systematic subdivision of project milestones made the various difficulties in handling research problems easier to tackle. Rigor and high quality work are some of the many things that I learned from him.

I wish to thank all the members of my committee for taking the time to review this work. I am particularly grateful to Dr. Basil Antar for his comments on the vorticity of the Taylor–Culick problem and to Dr. Roy Schulz for his helpful feedback on vorticity and entropy production. I also thank Dr. Jie-Zhi Wu for his comments on Kelvin's theorem and Dr. Michel El Hayek for his input on the entropy analysis for the variational solutions.

My utmost gratitude and appreciation is conveyed to Nancy Daher for her relentless support and encouragement in all aspects of my life and particularly in my career. She has constantly played a central role in all my endeavors and I truly thank her for helping me find the strength to follow through many projects and important decisions. She has always been up to date with my doctoral work and gracefully helped in reviewing this dissertation. I am sincerely grateful and indebted to her.

I am very thankful to Brenda Brooks from the UTSI library for her persistent efforts in providing me with the required references.

I wish to thank Eric Jacob and Joshua Batterson for their support and collaboration throughout many academic and scientific projects; Timothy Barber for many creative discussions and for his sense of humour; and Rawad Saleh for several inspiring conversations and for providing me with some references.

I am grateful to Dr. Boris Kupershmidt for giving me the opportunity to help him with some number theory problems. I also thank Dr. Bruce Bomar for his career advice and encouragement.

I thank my parents Georgette and Youssef Saad, and my Godparents Lily and the late Albert Sara, for their moral support throughout my life. I also extend my sincere gratitude to my *parrains* Philippe de Geelhand Delerscem and Daniel Letiesche for their support throughout my education. I am truly indebted to my sister Jocelyne who is partly responsible for the person that I currently am. I also thank my brothers Elie and Charbel for their support.

I thank all my colleagues and friends at UTSI for an excellent graduate experience. Specifically, I would like to acknowledge the following people: Michel Akiki, Matthew Duran, Erin Halpenny, Benjamin Klamm, Brian Maicke, William Robinson, Paula Sanematsu, Scott Van Zandbergen, Andrew Wilson, and Nadim Zgheib.

Finally, I would like to thank the University of Tennessee Space Institute for providing me with tuition waiver and stipend support throughout my doctoral work. I wish to thank the Lloyd W. Crawford fellowship program that partially supported my stipend in 2005 and 2007. I would also like to acknowledge the International Research and Education in Engineering program sponsored by the National Science Foundation for funding my trip to Peking University, China, in the summer of 2008.

Nullius in verba

(Motto of the Royal Society of London)

Abstract

This dissertation is concerned with the mathematical modeling of the flow in a porous cylinder with a focus on applications to solid rocket motors. After discussing the historical development and major contributions to the understanding of wall injected flows, we present an inviscid rotational model for solid and hybrid rockets with arbitrary headwall injection. Then, we address the problem of pressure integration and find that for a given divergence free velocity field, unless the vorticity transport equation is identically satisfied, one cannot find an analytic expression for the pressure by direct integration of the Navier-Stokes equations. This is followed by the application of a variational procedure to seek novel solutions with varying levels of kinetic energies. These are found to cover a wide spectrum of admissible motions ranging from purely irrotational to highly rotational fields. Subsequently, a second law analysis as well as an extension of Kelvin's energy theorem to open boundaries are presented to verify and corroborate the variational model. Finally, the focus is shifted to address the problem of laminar viscous flow in a porous cylinder with regressing walls. This is tackled using two different analytical techniques, namely, perturbation and decomposition. Comparisons with numerical Runge–Kutta solutions are also provided for a variety of wall Reynolds numbers and wall regression speeds.

Contents

List of Tables

List of Figures

Nomenclature

$\alpha = \dfrac{a\dot{a}}{\nu}$	Wall permeability
α_n	Sidewall injection sequence
β_n	Headwall injection sequence
$\mathscr{C} \approx 0.915965$	Catalan's constant
$\chi_n \equiv \frac{1}{2}(2n+1)\pi r^2$	Action variable
$\dot{a} = \dfrac{\mathrm{d}a}{\mathrm{d}t}$	Wall regression speed
$\mathcal{E} \equiv \dfrac{E_{\mathcal{V}}}{L^3}$	Kinetic energy density
μ	Dynamic viscosity
$\Omega = \Omega_\theta$	Tangential component of vorticity
$\boldsymbol{\Omega}$	Vorticity vector
ϕ	Velocity potential
ψ	Stream function
ρ	Density
$\bar{\rho}$	Density of irrotational motion
$\mathcal{S}$	Surface

$\mathrm{Re} \equiv \dfrac{U_{\mathrm{w}} a}{\nu}$	Injection Reynolds number based on the sidewall velocity
θ	Tangential coordinate (cylindrical)
$\mathbf{u}$	Velocity field
$\bar{\mathbf{u}}$	Irrotational velocity field
$\tilde{\mathbf{u}} = \mathbf{u} - \bar{\mathbf{u}}$	Vortical component of motion
U_{w}	Sidewall injection velocity
$\mathcal{V}$	Volume
*	Denotes a dimensional variable
$^+$	Type II variable
$^-$	Type I variable
a	Chamber radius (cylindrical) or channel half height (planar)
D_n	Residual error control sequence
p	Pressure
p_{c}	Centerline pressure
$Q(r, z)$	Residual error
r	Radial coordinate (cylindrical)
u	Radial velocity (denotes axial velocity in planar configurations)
v	Tangential velocity (denotes transverse velocity in planar configurations)
w	Axial velocity (denotes spanwise velocity in planar configurations)

$w_0(r)$	Headwall injection profile in cylindrical configurations
x	Axial coordinate (planar)
y	Transverse coordinate (planar)
z	Axial coordinate (cylindrical)
ADM	Adomian Decomposition Method
HAM	Homotopy Analysis Method
ODE	Ordinary Differential Equation
PDE	Partial Differential Equation
SRM	Solid Rocket Motor

Chapter 1

Introduction

The flow in regions bounded by porous surfaces has received much attention during the second half of the 20^{th} century due to its pertinence to a variety of industrial applications. The ensuing motion, driven by either injection or suction at the boundaries, can be used to model a variety of practical problems such as paper manufacturing (Taylor 1956), isotope separation (Berman 1953), mass transfer in the respiratory system, filtration, irrigation, ablation cooling, surface sublimation, and solid rocket gas dynamics (Culick 1966).

Wall injected flows are initiated by the injection or suction of a fluid through the boundaries of a conduit having an arbitrary shape and cross sectional area as illustrated in Figure 1.1 for the special case of a porous channel. In general, one is required to solve the partial differential equations (PDEs) governing the motion of a fluid in order to obtain a meaningful solution (Terrill and Thomas 1969). This is a formidable task that has proven to be impossible in a general three dimensional setting. Fortunately, for the practical cases of incompressible flow in a channel or pipe with uniform injection or suction, Berman (1953) has shown that the governing equations can be reduced to a third order nonlinear ordinary differential equation (ODE) whose analytical solution can be made amenable by a variety of analytical procedures. He did this by assuming that the transverse velocity component v is

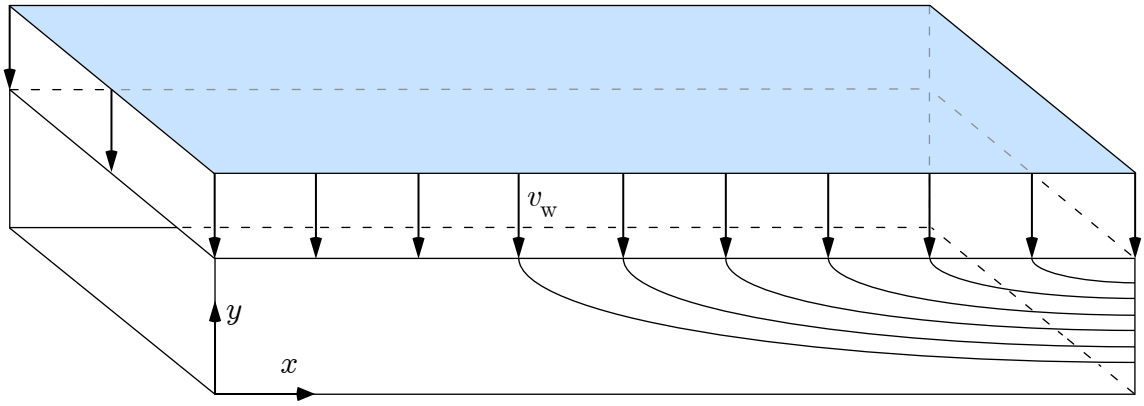

Figure 1.1: Schematic illustrating the flow in a porous channel with sidewall injection.

axially independent thus recovering a streamfunction that varies linearly in the axial direction of motion, i.e. $\psi(x, y) = xF(y)$ (Berman 1953; White 2005). By considering the limiting case of a small suction Reynolds number, Re $\sim \varepsilon$, Berman used a regular perturbation expansion in Re to solve for the mean flow function $F(y)$. The Reynolds number is based on the fluid velocity at the wall, v_w, and the channel half height, a. As for the case of large suction Reynolds numbers, Berman argues that the limit of the reduced ODE cannot be used to resolve that case due to the reduction in order of the governing equation (Berman 1953). Later, however, Sellars (1955) and Terrill (1964) were able to extract an analytical solution for that case by using the fact that the boundary layer is shifted towards the sidewall thus requiring a proper change of variables.

It is generally believed that Berman (1953) was the first to examine the problem of laminar viscous flow bounded by porous surfaces (see Majdalani and Zhou 2003). Although his similarity transform was applied to a planar configuration with suction at the walls, it set forth the foundation for most subsequent analytical and numerical investigations in a variety of geometries for either injection, suction, or both (Proudman 1960).

Chronologically, these start with Sellars (1955) who was successful in extending Berman's solution to large suction Reynolds numbers. He accomplished this by discarding the no-slip boundary condition for this limiting case thus uncovering a

leading order approximation that corresponded to uniform axial motion, i.e. $F(y) = y$. He then integrated the governing equation by making appropriate substitutions of the leading order approximation. In fact, his model is compatible with the outer solution in a standard boundary layer treatment. Sellars' observation of the existence of a thin boundary layer at the wall for the large suction case will prove crucial for the subsequent development of the solutions for this problem.

Of particular interest to this dissertation is the work of Taylor (1956) who derived an inviscid rotational solution for both planar and axisymmetric configurations. The absence of viscosity in his model is congruent with a leading order solution of Berman's problem with a large injection Reynolds number, i.e. $F(y) = \sin(\frac{1}{2}\pi y)$. The most peculiar characteristic of Taylor's model is that it observed the no-slip boundary condition at the sidewall. This is due to the normal velocity requirement that causes the axial flow to vanish at the injecting boundary.

Returning to the viscous flow problem in a porous channel, Yuan (1956) was the first to develop a solution for moderate to large Reynolds numbers for both injection or suction. His solution approaches Taylor's in the limit of large injection Reynolds numbers. However, Yuan's model suffered from a singularity in the third derivative at the centerline which pointed out the existence of a thin boundary layer (Terrill 1965). This was remedied by Terrill (1965) whose work stood out thanks to the numerical solutions that he provided for this problem.

White et al. (1958) were the first to advance a treatment of the porous channel problem for all ranges of the Reynolds number. To accomplish this task, they used a power series expansion centered around $\mathrm{Re} = 0$. They were also among the first to supply a numerical solution for this problem. Albeit very accurate, their power series depended on two arbitrary constants that required the use of a computer for trial and error evaluation. According to Terrill (1964), this would be a suitable method for intermediate values of Re ($15 \leq \mathrm{Re} \leq 35$). Otherwise, a proper transformation of the governing equation allows for direct numerical integration. Nonetheless, it is

gratifying to know that one can obtain a single analytical expression for the entire range of Re, a feat that perturbation methods fail to accomplish.

Finally, Terrill (Terrill 1964, 1965) compiled a comprehensive and detailed résumé of the perturbation solutions of this problem for all ranges of the Reynolds number. He derived and discussed the solutions for all limiting cases (i.e. $\mathrm{Re} = 0$, $|\mathrm{Re}| \ll 1$, $\mathrm{Re} \to +\infty$, $\mathrm{Re} \to -\infty$) and compared the various solutions with numerical simulations based on Runge–Kutta integration. For the numerical integration scheme, he used a clever transformation by allowing the Reynolds number to be determined a posteriori, i.e. at the end of the calculation. Of note also is the work of Eckert et al. (1957) who, as far as the author can verify, were the first to present a numerical solution of the laminar viscous flow in a porous channel.

The variety of analytical models for the planar case appeared to be unique and stable (Terrill and Thomas 1969; White 2005). However, Robinson (1976) showed that dual solutions exist for large suction while Zaturska et al. (1988) furnished a detailed stability analysis and rigorously showed that (at least) three types of solutions exist. The intricacies of wall injected flows arise in the case of axisymmetric flow in a porous pipe. Terrill and Thomas (1969) have rigorously shown that, at least, dual solutions exist for the entire range of injection and suction Reynolds numbers while no steady solutions exist whatsoever for $2.3 < \mathrm{Re} < 9.1$.

1.1 Impact on propulsion systems

In the meantime, the propulsion community had just started addressing the combustion instability problem in rocket motors (Culick 2006). The traditional modus operandi to handle this complicated problem is to treat the internal motion of the gases in solid rocket motors as the superposition of a steady average flow and a conglomeration of unsteady fields (Majdalani et al. 2002; Culick 2006). The average flow, also commonly known as the mean flow, represents the bulk motion of the gases in the rocket and can be approximated by the steady flow in a porous pipe or

channel. On the other hand, an unsteady field corresponds to any perturbed signal that propagates within the mean flow throughout the domain. Typical unsteady fields amount to acoustic, pressure, vorticity, and entropy waves. The importance of the mean flow is therefore evident due to the tight coupling between the steady and unsteady motions.

Although the earliest studies on the stability of rockets treated them as porous ducts, these failed to consider a satisfactory mean flow due to the complexity of the ensuing analysis. For example, the first theoretical study that addresses the acoustic instabilities in rockets was presented by Grad (1949) (see Culick 2006, for historical information). However, Grad assumes that the mean flow velocity field is negligible, i.e. a stagnant fluid, thus reducing the study to that of aeroacoustic instability in a cylinder.

McClure and coworkers were instrumental in the understanding of rocket motor instabilities, albeit their earliest studies focused on the thin region near the injecting surface (Hart and McClure 1959; Hart et al. 1960; McClure et al. 1960; Hart and Cantrell 1963; Hart and McClure 1965). McClure et al. (1963) were the first to use a mean flow solution in their study of the aeroacoustic field in SRMs*. Their model of choice corresponded to the irrotational motion of a fluid between two parallel porous plates. This was a substantial improvement over previous studies and showed the importance and intimate dependence of the unsteady field on the average flow.

It was not until Culick (1966) that an adequate representation of the mean flow in cylindrical port motors was proposed. Culick's model is inviscid and rotational and is able to secure all the boundary conditions including no-slip at the sidewall. Although similar to the one obtained by Taylor (1956) a decade earlier, Culick's solution received much welcome in the propulsion community and is now at the foundation of combustion instability studies, particle-mean-flow interactions, and other related analyses in solid propellant rocket motors. It is usually referred to as the Taylor–Culick profile and is one of the most ubiquitous mean flow models

*Definition may be found in the nomenclature section.

in rocket motor instability studies. Subsequently, Flandro (1967, 1983, 1985, 1986, 1995a,b) made extensive use of the Taylor–Culick model as a basis for developing his combustion instability framework.

1.2 Further improvements

Majdalani and coworkers are amidst the leading investigators to amend the Taylor–Culick profile by providing novel solutions of varying degrees of accuracy, complexity, and applicability. For example, they provided models for the flow in SRMs with tapered bores for both slab (Saad et al. 2006) and cylindrical (Sams et al. 2007) configurations. Their method consisted of a regular perturbation expansion of the mean flow based on the work of Clayton (1996). The resulting solutions can be used to model realistic geometries by accounting for the effects of the tapered walls.

The next important improvement in this area consists of the derivation of a compressible Taylor–Culick profile by Majdalani (2007). His solution faithfully retained the essential ingredients of Culick's model, but included the effects of compressibility by using a Rayleigh-Janzen expansion at higher orders. The Rayleigh-Janzen expansion is a regular perturbation expansion in even (or odd) powers of the Mach number (Rayleigh 1916; Janzen 1913). Subsequently, Maicke and Majdalani (2008) submitted a similar study but in a planar configuration. Both analyses resulted in velocity fields that exhibited steep streamline curvatures reminiscent of time averaged turbulent profiles.

Other improvements include the work of Kurdyumov (2006) who extended the Taylor–Culick solution to ducts with a complex geometry. Tsangaris et al. (2007) extended Terrill's work for a porous pipe to include unsteady injection or suction at the sidewall. Finally, Erdogan and Imrak (2008) derived a novel laminar solution for the flow in a porous pipe. Their solution consisted of expanding the velocity field as a series in terms of the modified Bessel function of order n.

Recent work includes the extension of the Taylor and Taylor–Culick models to hybrid rockets by allowing for an arbitrary injection profile at the headwall (Majdalani and Saad 2007; Saad and Majdalani 2009b). This will be the topic of Chapter 2 where the solutions for the Taylor–Culick flow with arbitrary injection will be thoroughly derived and compared to fourth order inviscid CFD* simulations. Later, Saad and Majdalani (2010) proposed a variational procedure using Lagrangian multipliers to seek solutions with minimum kinetic energy. That helped to uncover a wide array of motions ranging from purely irrotational to highly rotational fields. Their method was also applied in the context of slab rocket motors (Saad and Majdalani 2008a) and the bidirectional vortex with single (Saad and Majdalani 2008b) and multiple mantles (Saad and Majdalani 2009a).

Probably the most significant amelioration of the mean flow in rocket motors was the manuscript presented by Goto and Uchida (1990). Their study consisted of allowing the porous sidewalls of a cylindrical rocket motor to expand or contract radially thus closely mimicking the practical burning of solid propellant grain. Their technique employed a similarity in space and time first introduced by Uchida and Aoki (1977) who studied the effect of wall expansion or contraction on the flow in a non porous pipe. In essence, they incorporated Berman's space similarity (Berman 1953) with Uchida's time similarity (Uchida and Aoki 1977) and recovered a third order ODE in the wall Reynolds number and the wall expansion parameter α. The wall expansion parameter is a dimensionless number that characterizes the regression speed and can be thought of as a wall regression Reynolds number. The resulting ODE is then solved numerically using a fourth order Runge–Kutta method. Dauenhauer and Majdalani (2003) later applied this method in the context of a slab rocket motor (see also Dauenhauer and Majdalani 1999). Since this approach requires the use of a shooting method for both the first and third derivatives, they proposed a systematic technique for computing the initial guesses using a two dimensional Newton-Raphson method. The analytical solution for the problem

*Definition may be found in the nomenclature section.

with wall regression was subsequently presented by Majdalani and Zhou (2003) who provided perturbation solutions for all ranges of the Reynolds number. Majdalani et al. (2002) also applied the same approach in the context of a cylindrical geometry where the solution for large injection was discussed (see also Majdalani et al. 2009, for correct form).

1.3 Scope

This work is concerned with the general mathematical nature of the flow in a porous cylinder with a focus on applications to solid rocket motors. It can be divided into two parts:

(a) Inviscid rotational models

(b) Viscous models with regressing walls

In the first part, we focus on solutions in the limit of a large injection Reynolds number. The assumption of an inviscid flow allows one to find exact as well as approximate rotational solutions with headwall injection. These can be used to extend the applicability of mean flow models to hybrid rocket engines* as well as solid rocket motors with burning fore end. These solutions are uncovered by solving the vorticity equation after determining a proper relation between the vorticity and the streamfunction. This relation can be extracted from the steady vorticity transport equation. The resulting governing PDE is linear and can be readily solved by using separation of variables. Being linear, one can employ superposition to resolve the effects of an axisymmetric injection profile at the headwall. The ensuing solutions are approximate in general except for profiles that are similar to the inert sinusoidal Taylor–Culick motion.

*Hybrid rockets are engines in which one component of the propellant is stored in liquid phase while the other is stored in solid phase. The most common variation consists of a uniformly laid solid fuel on the inner surface of a cylinder with the liquid oxidizer being injected at the headend (Sutton and Biblarz 2000).

For the approximate solutions corresponding to headwall injection, certain difficulties are encountered in trying to extract an analytical expression for pressure. To understand this behavior, a thorough mathematical treatment of integrating the Navier-Stokes equations is sought after in Chapter 3. By proceeding systematically, a nonlinear set of constraints is recovered that, if satisfied, will guarantee the existence of an analytical pressure field. We discuss the implications of these constraints on the physicality of divergence free velocity fields and their effect on the pressure.

In Chapter 4, a variational procedure is applied to seek solutions with minimum or maximum total kinetic energy. The method of Lagrangian multipliers is utilized to help expose a wide spectrum of possible motions with varying energy levels. Specifically, two families of solutions are derived that bear increasing or decreasing energy content with respect to the Taylor–Culick model. These are found to cover the entire range of vortical motions: from purely irrotational to highly rotational fields. Interestingly, the least kinetic energy solution corresponds to the irrotational motion. To understand the behavior and physicality of these profiles, a second law analysis is pursued and it is found that the Taylor–Culick model corresponds to a stable local equilibrium point for the inviscid flow in a porous pipe.

The first part is then concluded with an extension of Kelvin's minimum energy theorem to regions with open boundaries. This allows us to apply Kelvin's theorem to the variational model and verify independently, that indeed, the irrotational motion does carry the least kinetic energy. Finally, a few examples and implications of this extension are presented and discussed.

In the second part of this work, we direct our attention to the problem of laminar viscous flow in a porous pipe with radially regressing walls. In particular, we concentrate on providing an exposé of the mathematical techniques that can be used to handle the nonlinearities in this kind of problem. Two analytical methods are engaged, namely, perturbation and decomposition. These are systematically implemented and compared to Runge–Kutta integration of the governing equation.

Chapter 2

Arbitrary Injection

In this chapter, we derive a model for the mean flow in a solid rocket motor that captures the effects of headwall injection. The ability of the present solution to account for arbitrary headwall injection allows us to tackle a wider range of problems from both theoretical and practical perspectives. It also bears the potential to handle both solid and hybrid rocket motors in a unified analysis, the difference being only in the relative magnitudes of the injection streams. The approach is based on the vorticity streamfunction formulation in which the vorticity transport equation is used to obtain a functional relation between the streamfunction and the vorticity. Then, the solution is obtained by solving the vorticity equation. In the process, a multitude of injection profiles may be solved for by using superposition. The solutions are then tested using three representative injection profiles and compared to finite volume CFD simulations of the Euler equations.

2.1 Mathematical model

A rocket motor can be idealized as a cylindrical chamber of porous length L^* and radius a with both a reactive headwall and a nozzleless aft end as shown in Figure 2.1. The radial and axial velocities are represented by u^* and w^*, respectively, while r^* and z^* stand for the radial and axial coordinates used to describe the solution

from the headwall to the typical nozzle attachment point at the chamber outlet. At the headwall, a fluid stream (which may denote an oxidizer or gaseous propellant mixture) is injected into the chamber at a prescribed velocity $w_0^*(r^*)$. This could be given by

$$w_0^*(r^*) = w^*(r^*, z^* = 0) = \begin{cases} W_c^* = \text{const}; & \text{uniform} \\ W_c^* \cos(\frac{1}{2}\pi r^{*2}/a^2); & \text{cosine} \\ W_c^*[1 - (r^*/a)^m]; & \text{laminar and turbulent} \\ W_c^*(1 - r^*/a)^{1/m}; & \text{turbulent} \end{cases} \tag{2.1}$$

where $W_c^* = w^*(0, 0)$ is the centerline speed at the headwall (a constant), m is some integer, and the superscript denotes a dimensional variable. The incoming stream merges with the cross flow sustained by uniform mass addition along the porous sidewall. Naturally, the sidewall injection velocity $U_w = -u^*(a, z^*)$ is commensurate with propellant or fuel regression rates. In hybrids, U_w can be appreciably smaller than W_c^* due to slow fuel pyrolysis; in SRM analysis, these two values are identical.

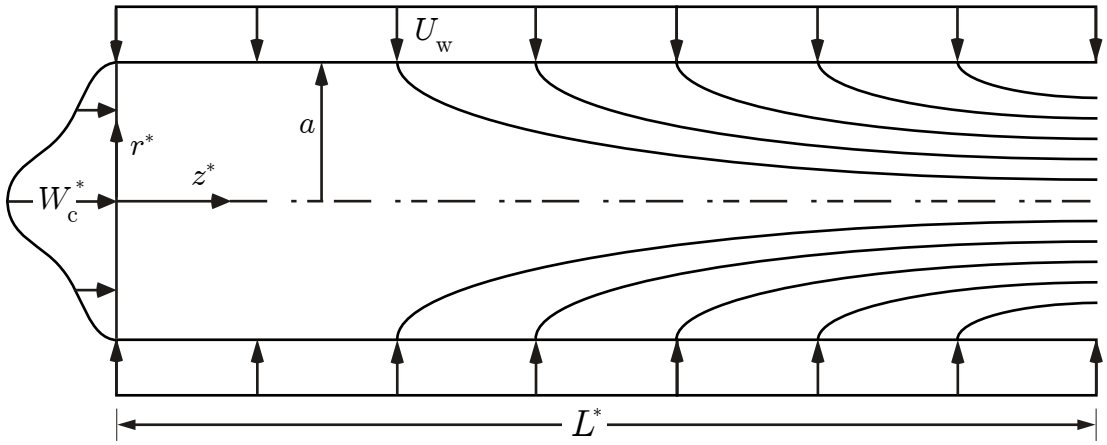

Figure 2.1: Schematic of an idealized solid rocket motor with sidewall injection.

2.1.1 Normalization

It is useful to normalize all recurring variables and operators. This can be done by setting (see Majdalani and Saad 2007)

$$\begin{gathered} r=\frac{r^*}{a};\ z=\frac{z^*}{a};\ \nabla=a\nabla^*;\ p=\frac{p^*}{\rho U_{\mathrm{w}}^2};\ \psi=\frac{\psi^*}{a^2U_{\mathrm{w}}}; \\ u=\frac{u^*}{U_{\mathrm{w}}};\ w=\frac{w^*}{U_{\mathrm{w}}};\ \boldsymbol{\Omega}=\frac{\boldsymbol{\Omega}^*a}{U_{\mathrm{w}}};\ W_{\mathrm{c}}=\frac{W_{\mathrm{c}}^*}{U_{\mathrm{w}}};\ L=\frac{L^*}{a}; \end{gathered} \tag{2.2}$$

Note that this normalization applies to all subsequent analyses presented in this dissertation.

2.1.2 Governing equations

A non-reactive flow may be assumed, prompted by the thin reactive zone above the grain surface. Following Culick (1966), the flow can be taken to be steady, inviscid, incompressible, rotational, and axisymmetric. It should be noted that Majdalani (2007) and Maicke and Majdalani (2008) derived compressible Taylor–Culick solutions under isentropic flow conditions. These confirm the suitability of the present model for a variety of applications in which the effects of compressibility are small. At the outset, the normalized Euler equations with no swirl are written as

$$\frac{1}{r}\frac{\partial(ru)}{\partial r}+\frac{\partial w}{\partial z}=0 \tag{2.3a}$$

$$u\frac{\partial u}{\partial r}+w\frac{\partial u}{\partial z}=-\frac{\partial p}{\partial r} \tag{2.3b}$$

$$u\frac{\partial w}{\partial r}+w\frac{\partial w}{\partial z}=-\frac{\partial p}{\partial z} \tag{2.3c}$$

or, in vector form

$$\nabla\cdot\mathbf{u}=0 \tag{2.4a}$$

$$\mathbf{u}\cdot\nabla\mathbf{u}=-\nabla p \tag{2.4b}$$

One may now invoke the dyadic vector identity (Karamcheti 1966)

$$\mathbf{u}\cdot\nabla\mathbf{u} \equiv \nabla(\tfrac{1}{2}\mathbf{u}\cdot\mathbf{u}) - \mathbf{u}\times\nabla\times\mathbf{u} \tag{2.5}$$

and substitute it into (2.4b). Then, by taking the curl of the resulting expression, one obtains the vorticity transport equation for steady, inviscid motion

$$\nabla\times(\mathbf{u}\times\boldsymbol{\Omega}) = 0 \tag{2.6}$$

where

$$\boldsymbol{\Omega} = \nabla\times\mathbf{u} \tag{2.7}$$

Note that by taking the curl of (2.4b), the gradient of the kinetic energy $\nabla(\frac{1}{2}\mathbf{u}\cdot\mathbf{u})$ and that of the pressure ∇p vanish since $\nabla\times\nabla\phi = 0$ given that ϕ is a continuous and twice differentiable function. Finally, four boundary conditions can be prescribed by writing

$$\begin{cases} u(0,z) = 0; & \text{no flow across centerline} \\ w(1,z) = 0; & \text{no slip at sidewall} \\ u(1,z) = -1; & \text{constant radial inflow at sidewall} \\ w(r,0) = w_0(r); & \text{axial inflow at headwall} \end{cases} \tag{2.8}$$

where the headwall injection profile may take any of the following forms

$$w_0(r) = \begin{cases} W_\mathrm{c} = \text{const} \\ W_\mathrm{c}\cos(\frac{1}{2}\pi r^2) \\ W_\mathrm{c}(1-r^m) \end{cases} \tag{2.9}$$

2.1.3 Vorticity-streamfunction approach

Continuity is fulfilled by the Stokes streamfunction (Karamcheti 1966) when it is written as

$$u = -\frac{1}{r}\frac{\partial \psi}{\partial z}; \quad w = \frac{1}{r}\frac{\partial \psi}{\partial r} \tag{2.10}$$

Having a single nonzero component in the azimuthal direction, the vorticity simplifies to

$$\boldsymbol{\Omega} = \Omega_\theta \mathbf{e}_\theta \equiv \Omega \mathbf{e}_\theta \tag{2.11}$$

Then, substitution into the vorticity transport equation (2.6) yields

$$\frac{\partial \psi}{\partial r}\frac{\partial}{\partial z}\left(\frac{\Omega}{r}\right) - \frac{\partial \psi}{\partial z}\frac{\partial}{\partial r}\left(\frac{\Omega}{r}\right) = 0 \tag{2.12}$$

or

$$\frac{(\Omega/r)_z}{(\Omega/r)_r} = \frac{\psi_z}{\psi_r} \tag{2.13}$$

where the subscripts denote differentiation with respect to r or z, respectively. Equation (2.13) requires that

$$\Omega = rF(\psi) \tag{2.14}$$

since

$$\frac{(\Omega/r)_z}{(\Omega/r)_r} = \frac{[F(\psi)]_z}{[F(\psi)]_r} = \frac{F_\psi \psi_z}{F_\psi \psi_r} = \frac{\psi_z}{\psi_r} \tag{2.15}$$

So we follow Culick (1966) and set

$$\Omega = C^2 r \psi \tag{2.16}$$

Despite the non-uniqueness of this relation, it enables us to satisfy (2.6). Straightforward substitution into the vorticity equation (2.7) yields the characteristic PDE of the Taylor–Culick problem,

$$\frac{\partial^2 \psi}{\partial z^2} + \frac{\partial^2 \psi}{\partial r^2} - \frac{1}{r}\frac{\partial \psi}{\partial r} + C^2 r^2 \psi = 0 \tag{2.17}$$

with the particular set of constraints,

$$\lim_{r\to 0} \frac{1}{r}\frac{\partial \psi(r,z)}{\partial z} = 0 \tag{2.18a}$$

$$\frac{\partial\, \psi(1,z)}{\partial r} = 0 \tag{2.18b}$$

$$\frac{\partial \psi(1,z)}{\partial z} = 1 \tag{2.18c}$$

$$\frac{1}{r}\frac{\partial\, \psi(r,0)}{\partial r} = w_0(r) \tag{2.18d}$$

By virtue of L'Hôpital's rule, removing the singularity in (2.18a) requires that both

$$\frac{\partial \psi(0,z)}{\partial z} = 0 \tag{2.19a}$$

$$\frac{\partial^2\, \psi(0,z)}{\partial r \partial z} = 0 \tag{2.19b}$$

Being linear, (2.17) is solvable by separation of variables; it yields

$$\psi(r,z) = (\bar{\alpha} z + \bar{\beta})[A\cos(\tfrac{1}{2}Cr^2) + B\sin(\tfrac{1}{2}Cr^2)] \tag{2.20}$$

This expression satisfies (2.19b) identically. Thus, from this point forward, (2.18a) may be superseded by (2.19a). We may now proceed to implement the problem's constraints so that a unique solution may be attained.

2.2 Solution by eigenfunction expansion

Application of the boundary conditions is carried out in the order in which they appear. Starting with (2.19a), we obtain:

$$\frac{\partial \psi(0,z)}{\partial z} = \bar{\alpha} A\cos(\tfrac{1}{2}Cr^2) + \bar{\alpha} B\sin(\tfrac{1}{2}Cr^2)\big|_{r=0} = 0 \tag{2.21}$$

or $A = 0$. Without loss of generality, we set $B = 1$ and rewrite (2.18b) as

$$\frac{\partial\,\psi(1,z)}{\partial r} = rC(\bar{\alpha}z + \bar{\beta})\,\cos(\tfrac{1}{2}Cr^2)\big|_{r=1} = 0; \quad \forall\, z \in \mathbb{R}_0^+ \tag{2.22}$$

and so $\cos(\frac{1}{2}C) = 0$. This is satisfied if

$$C = C_n = (2n+1)\pi;\ \forall\, n \in \mathbb{N}_0 \tag{2.23}$$

Using $C_n = (2n+1)\pi$, we obtain an infinite series solution to (2.17). This process introduces an error term in (2.6) that will be examined in §2.4. We now put

$$\psi_n(r,z) = (\alpha_n z + \beta_n)\,\sin[(n+\tfrac{1}{2})\pi r^2] \tag{2.24}$$

For convenience, we introduce $\chi_n = \frac{1}{2}(2n+1)\pi r^2$ so that the total streamfunction is written as

$$\psi(r,z) = \sum_{n=0}^{\infty}(\alpha_n z + \beta_n)\,\sin\chi_n \tag{2.25}$$

The sidewall injection condition, (2.18c) gives

$$\frac{\partial\psi(1,z)}{\partial z} = \sum_{n=0}^{\infty}\alpha_n\,\sin[(n+\tfrac{1}{2})\pi] = 1 \quad \text{or} \quad \sum_{n=0}^{\infty}(-1)^n\alpha_n = 1 \tag{2.26}$$

This constraint may exhibit several outcomes depending on the behavior of α_n. One such case corresponds to Taylor's family of solutions for which

$$\alpha_0 = 1 \quad \text{and} \quad \alpha_n = 0; \quad \forall n \neq 0 \tag{2.27}$$

from which, by setting $\beta_n = 0$, we recover Culick's original solution (Culick 1966)

$$\psi(r,z) = z\,\sin(\tfrac{1}{2}\pi r^2) \tag{2.28}$$

Other forms of α_n will be discussed in Chapter 4. At the outset, (2.25) reduces to

$$\psi(r,z) = z\sin(\tfrac{1}{2}\pi r^2) + \sum_{n=0}^{\infty}\beta_n \sin\chi_n \tag{2.29}$$

Lastly, the headwall condition (2.18d) may be satisfied by employing orthogonality. Starting with

$$\frac{1}{r}\frac{\partial\psi(r,0)}{\partial r} = \pi\sum_{n=0}^{\infty}(2n+1)\beta_n\cos\chi_n = w_0(r) \tag{2.30}$$

one can apply orthogonality to secure

$$\beta_n\int_0^1(2n+1)\cos^2\chi_n\, r\,dr = \frac{1}{\pi}\int_0^1 w_0(r)\cos\chi_n\, r\,dr \tag{2.31}$$

or

$$\beta_n = \frac{4}{(2n+1)\pi}\int_0^1 w_0(r)\cos\chi_n\, r\,dr \tag{2.32}$$

The total solution is now at hand. Starting with the streamfunction

$$\psi(r,z) = z\sin(\tfrac{1}{2}\pi r^2) + \sum_{n=0}^{\infty}\beta_n \sin\chi_n \tag{2.33}$$

The radial and axial velocities are given by

$$u(r) = -r^{-1}\sin(\tfrac{1}{2}\pi r^2) \tag{2.34}$$

$$w(r,z) = \pi z\cos(\tfrac{1}{2}\pi r^2) + \pi\sum_{n=0}^{\infty}(2n+1)\beta_n\cos\chi_n \tag{2.35}$$

Note that the radial velocity is independent of β_n. Finally, the vorticity is

$$\Omega(r,z) = \pi^2 rz\sin(\tfrac{1}{2}\pi r^2) + \pi^2 r\sum_{n=0}^{\infty}(2n+1)^2\beta_n\,\sin\chi_n \tag{2.36}$$

This general form of the Taylor–Culick profile represents a solution for an arbitrary headwall injection pattern $w_0(r)$ that can be captured by the equation for β_n from

(2.32). The classical Taylor–Culick solution with inert headwall is easily recovered by setting $\beta_n = 0$. Its streamlines are shown in Figure 2.2.

2.3 Variable headwall injection profiles

The analysis may be illustrated using a variable headwall injection profile. For instance, one may use

$$w_0(r) = \begin{cases} W_{\mathrm{c}} = \text{const}; & \text{uniform} \\ W_{\mathrm{c}} \cos(\frac{1}{2}\pi r^2); & \text{cosine} \\ W_{\mathrm{c}}(1 - r^2); & \text{parabolic} \end{cases} \tag{2.37}$$

These are prescribed by classic profiles used by Berman (i.e. cosine) (Berman 1953), Poiseuille (White 2005), and others.

2.3.1 Uniform injection

In this case, the headwall injection sequence β_n takes the form

$$\beta_n = \frac{4(-1)^n W_{\mathrm{c}}}{\pi^2(2n+1)^2} \tag{2.38}$$

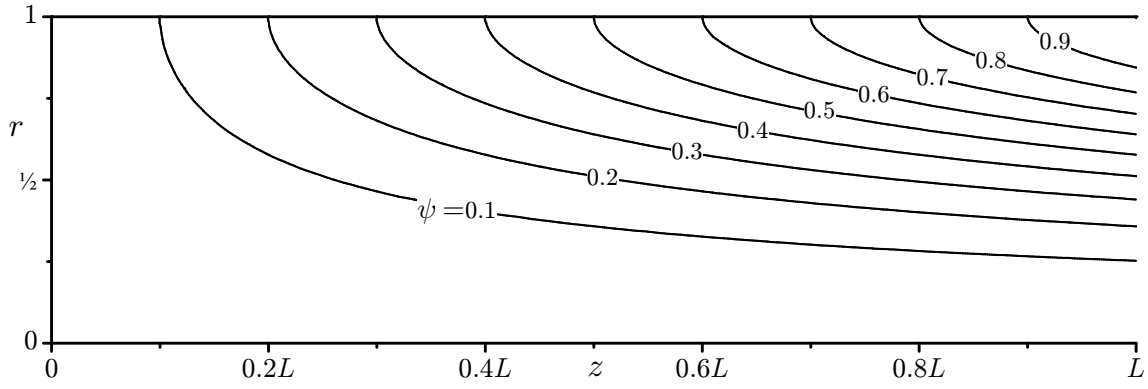

Figure 2.2: Streamlines corresponding to the Taylor–Culick flow with an inert headwall.

The streamfunction is

$$\psi(r,z) = z\sin(\tfrac{1}{2}\pi r^2) + \frac{4W_\mathrm{c}}{\pi^2}\sum_{n=0}^{\infty}\frac{(-1)^n}{(2n+1)^2}\sin\chi_n \tag{2.39}$$

while the axial velocity and vorticity are given by, respectively

$$w(r,z) = \pi z\cos(\tfrac{1}{2}\pi r^2) + \frac{4W_\mathrm{c}}{\pi}\sum_{n=0}^{\infty}\frac{(-1)^n}{(2n+1)}\cos\chi_n \tag{2.40}$$

$$\Omega(r,z) = \pi^2 rz\sin(\tfrac{1}{2}\pi r^2) \tag{2.41}$$

The character of (2.39) is illustrated in Figure 2.3. Using $W_\mathrm{c} = U_\mathrm{w} = 1$, a balance between sidewall and headwall injection causes the streamline originating at the corner $(r = 1, z = 0)$ to bisect the flow field at an angle of $\pi/4$ as shown in Figure 2.3b. By concentrating on specific areas as in Figure 2.3c, it may be seen that the solution conforms to the stated boundary conditions. It is also evident that $w_0(r) = W_\mathrm{c} = 1$ corresponds to a simulated solid propellant grain that is burning evenly along its surfaces.

2.3.2 Cosine injection

For the cosine injection profile, we use (2.32) to get

$$\beta_n = \begin{cases} \dfrac{W_\mathrm{c}}{\pi} \equiv W_\mathrm{h}; & n = 0 \\ 0; & \text{otherwise} \end{cases} \tag{2.42}$$

Using (2.10), the streamfunction is then given by

$$\psi(r,z) = (z + W_\mathrm{h})\cos(\tfrac{1}{2}\pi r^2) \tag{2.43}$$

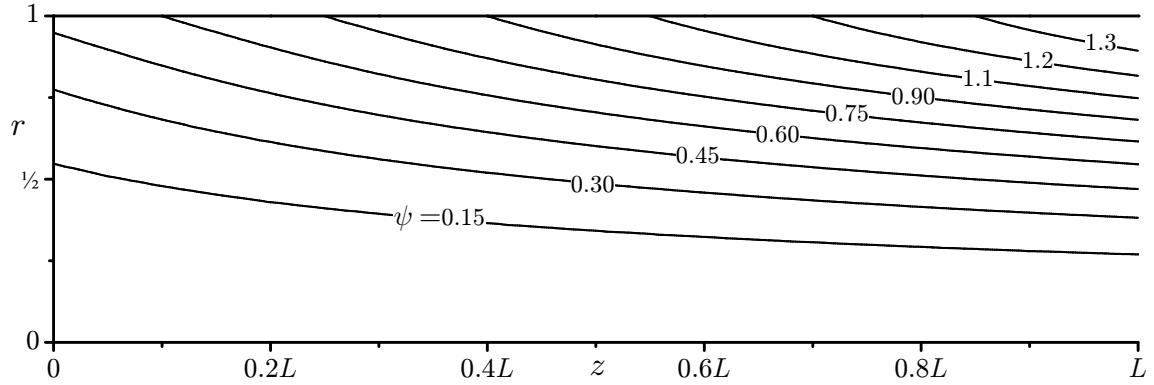

(a) Overall streamline pattern

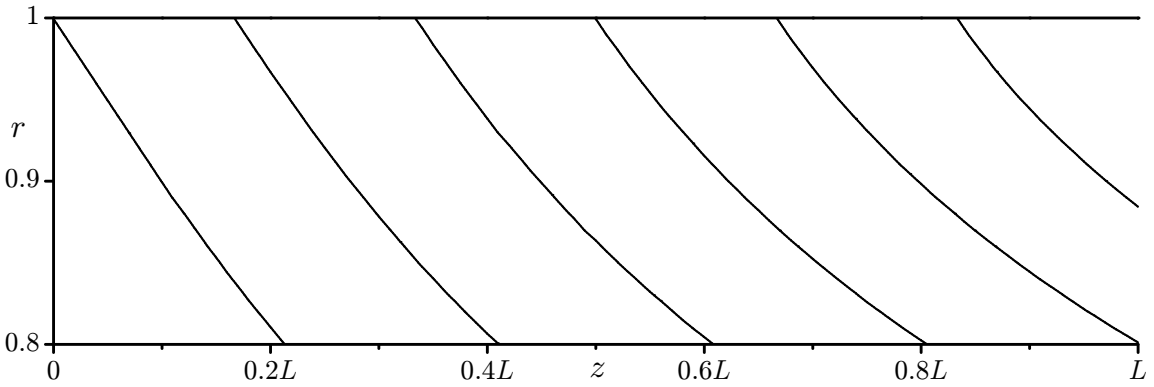

(b) Streamline bisector at the upper left corner

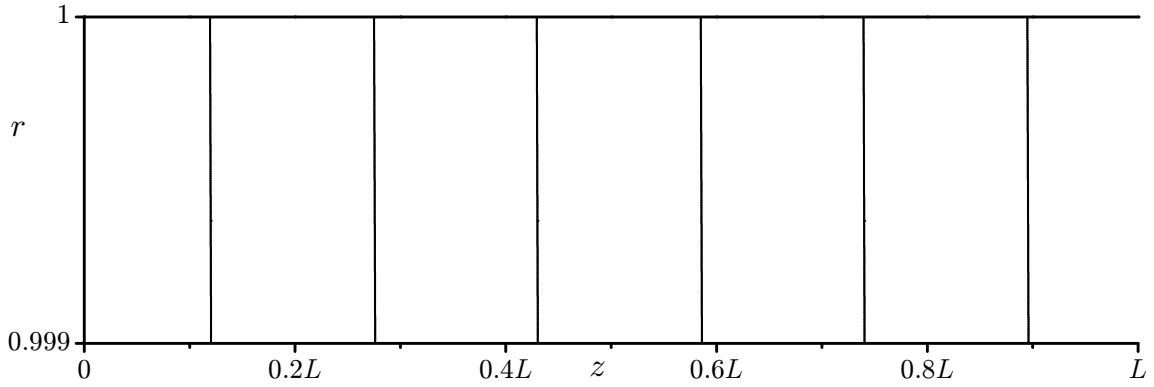

(c) Showing no-slip boundary condition

Figure 2.3: Streamlines corresponding to uniform headwall injection with $W_c = 1$.

The streamlines for the cosine headwall injection case are shown in Figure 2.4. The axial velocity and vorticity are given by

$$w(r,z) = \pi(z + W_{\rm h})\cos(\tfrac{1}{2}\pi r^2) \tag{2.44}$$

$$\Omega(r,z) = \pi^2 r(z + W_{\rm h})\sin(\tfrac{1}{2}\pi r^2) \tag{2.45}$$

It is to be noted that while the solution for other injection profiles is approximate, the one corresponding to similarity type headwall injection is exact, such as the case for the cosine injection. The reason for this behavior will be discussed at length in §2.4.

2.3.3 Parabolic injection

For the parabolic profile, one may use $w_0(r) = W_{\rm c}(1 - r^2)$ in (2.32) to obtain

$$\beta_n = \frac{8W_{\rm c}}{(2n+1)^3\pi^3} \tag{2.46}$$

Subsequently, the streamfunction, axial velocity, and vorticity are

$$\psi(r,z) = z\sin(\tfrac{1}{2}\pi r^2) + \frac{8W_{\rm c}}{\pi^3}\sum_{n=0}^{\infty}\frac{1}{(2n+1)^3}\sin\chi_n \tag{2.47}$$

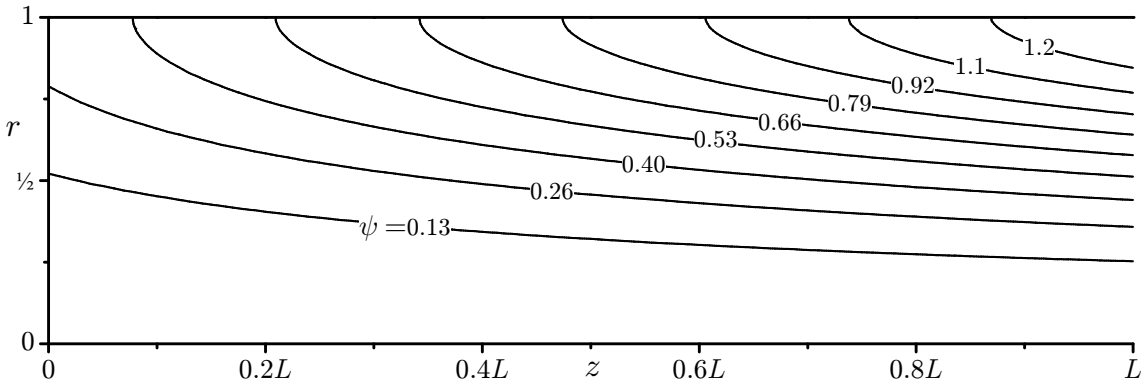

Figure 2.4: Streamlines corresponding to cosine headwall injection with $W_{\rm c} = 1$.

$$w(r,z) = \pi z\cos(\tfrac{1}{2}\pi r^2) + \frac{8W_{\rm c}}{\pi^2}\sum_{n=0}^{\infty}\frac{1}{(2n+1)^2}\cos\chi_n \tag{2.48}$$

$$\Omega(r,z) = \pi^2 rz\sin(\tfrac{1}{2}\pi r^2) + \frac{8W_{\rm c}}{\pi}r\sum_{n=0}^{\infty}\frac{1}{(2n+1)}\sin\chi_n \tag{2.49}$$

The streamlines corresponding to this case are shown in Figure 2.5.

2.4 Nonlinear residual error

To test the accuracy of the solutions presented in this chapter, we substitute (2.29) into (2.6). Terms that do not entirely cancel are hereafter referred to as the residual error $Q(r,z)$. At the outset, Q may be calculated from

$$Q(r,z) = \|\nabla\times\mathbf{u}\times\boldsymbol{\Omega}\| = -\frac{\partial}{\partial r}(u\Omega) - \frac{\partial}{\partial z}(w\Omega) \tag{2.50}$$

In terms of the streamfunction and the vorticity, we have

$$Q(r,z) = -\frac{\Omega}{r^2}\frac{\partial\psi}{\partial z} + \frac{1}{r}\frac{\partial\psi}{\partial z}\frac{\partial\Omega}{\partial r} - \frac{1}{r}\frac{\partial\psi}{\partial r}\frac{\partial\Omega}{\partial z} \tag{2.51}$$

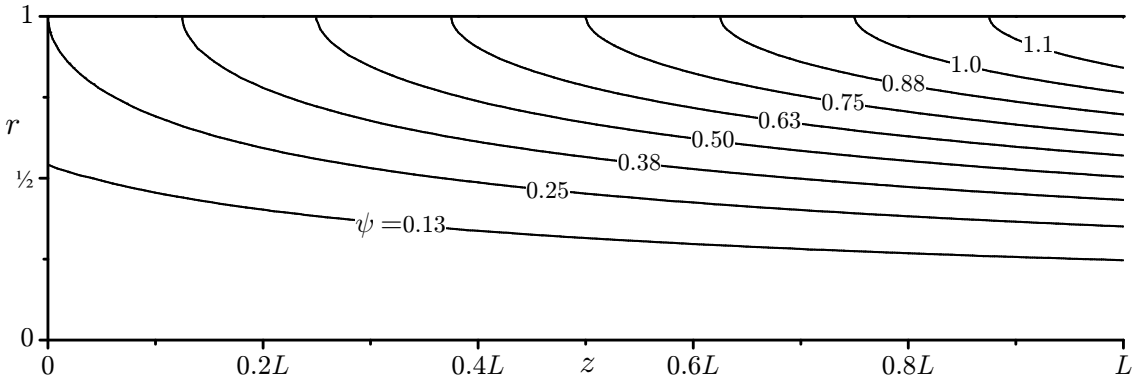

Figure 2.5: Streamlines corresponding to parabolic headwall injection with $W_{\rm c} = 1$.

For each eigensolution given by (2.33), the vorticity transport equation vanishes upon substitution and the corresponding residual is identically zero. Using

$$\Omega = \Omega_n = C_n^2 r \psi_n \tag{2.52}$$

Equation (2.51) becomes

$$\begin{aligned} Q_n &= -\frac{C_n^2\psi_n}{r}\frac{\partial\psi_n}{\partial z} + \frac{1}{r}\frac{\partial\psi_n}{\partial z}\frac{\partial}{\partial r}(C_n^2 r\psi_n) - \frac{1}{r}\frac{\partial\psi_n}{\partial r}\frac{\partial}{\partial z}(C_n^2 r\psi_n) \\ &= -\frac{C_n^2\psi_n}{r}\frac{\partial\psi_n}{\partial z} + \frac{1}{r}\frac{\partial\psi_n}{\partial z}C_n^2\psi_n + C_n^2\frac{\partial\psi_n}{\partial z}\frac{\partial\psi_n}{\partial r} - C_n^2\frac{\partial\psi_n}{\partial r}\frac{\partial\psi_n}{\partial z} = 0 \end{aligned} \tag{2.53}$$

The summation of (2.53) over all eigenmodes is identically zero if a hypothetical case may be considered for which all eigensolutions coexist independently. However, when coupling between eigenmodes is considered, the total vorticity and streamfunction must be accounted for in the vorticity transport equation. Substitution into (2.51) requires evaluating

$$Q = -\frac{1}{r^2}\sum_{n=0}^{\infty}\Omega_n\sum_{n=0}^{\infty}\frac{\partial\psi_n}{\partial z} + \frac{1}{r}\sum_{n=0}^{\infty}\frac{\partial\psi_n}{\partial z}\sum_{n=0}^{\infty}\frac{\partial\Omega_n}{\partial r} - \frac{1}{r}\sum_{n=0}^{\infty}\frac{\partial\psi_n}{\partial r}\sum_{n=0}^{\infty}\frac{\partial\Omega_n}{\partial z} \tag{2.54}$$

Then, by taking into account that

$$\begin{cases} \psi_n = (\alpha_n z + \beta_n)\sin\chi_n; & \dfrac{\partial\psi_n}{\partial z} = \alpha_n\sin\chi_n \\ \dfrac{\partial\psi_n}{\partial r} = rC_n(\alpha_n z + \beta_n)\cos\chi_n; & \dfrac{\partial\Omega_n}{\partial z} = rC_n^2\alpha_n\sin\chi_n \end{cases} \tag{2.55}$$

and, for the Taylor–Culick class of solutions, $\alpha_0 = 1$ and $\alpha_n = 0$ ($\forall\, n \neq 0$), one is left with

$$\frac{\partial\psi_n}{\partial z} = \frac{\partial\psi_0}{\partial z} = \sin(\tfrac{1}{2}\pi r^2); \quad \frac{\partial\Omega_n}{\partial z} = \frac{\partial\Omega_0}{\partial z} = C_0^2 r\frac{\partial\psi_0}{\partial z} \tag{2.56}$$

Note that the axial derivatives are solely due to the zeroth eigenmode. This reduces (2.54) into

$$Q = \frac{\partial \psi_0}{\partial z}\left(-\frac{1}{r^2}\sum_{n=0}^{\infty}\Omega_n + \frac{1}{r}\sum_{n=0}^{\infty}\frac{\partial \Omega_n}{\partial r} - C_0^2\sum_{n=0}^{\infty}\frac{\partial \psi_n}{\partial r}\right) \tag{2.57}$$

Finally, noting that

$$\frac{\partial \Omega_n}{\partial r} = C_n^2\psi_n + C_n^2 r\frac{\partial \psi_n}{\partial r} \tag{2.58}$$

we retrieve

$$Q(r) = \frac{\partial \psi_0}{\partial z}\sum_{n=0}^{\infty}\left(C_n^2 - C_0^2\right)\frac{\partial \psi_n}{\partial r} \tag{2.59}$$

or

$$Q(r) = \sin(\tfrac{1}{2}\pi r^2)\, r\sum_{n=1}^{\infty} C_n\beta_n(C_n^2 - C_0^2)\cos\chi_n \tag{2.60}$$

Equation (2.60) represents the net residual of the vorticity transport equation due to nonlinear coupling; it is not necessarily zero except for inert ($\beta_n = 0$) or sinusoidal headwall injection profiles ($\beta_n = 0\ \forall n \geq 1$).

To shed more light into the behavior of the residual error, we first expand the product of the various sequences in (2.60) as

$$C_n\beta_n(C_n^2 - C_0^2) = 4\pi^3 n(n+1)(2n+1)\beta_n = 4\pi^3 D_n \tag{2.61}$$

$$D_n \equiv n(n+1)(2n+1)\beta_n \tag{2.62}$$

We then rewrite (2.60) as

$$Q(r) = 4\pi^3 r\sin(\tfrac{1}{2}\pi r^2)\sum_{n=1}^{\infty} D_n\cos\chi_n \tag{2.63}$$

Clearly, the residual error is controlled by the behavior of D_n. This sequence represents the deviation from the exact solution corresponding to cosine headwall injection since, in that instance, $C_n^2 - C_0^2 = 0$. In the case of an inert headwall, $\beta_n = D_n = 0$, and the solution is exact. As $D_n \to 0$, the solutions become more

accurate. However, since $\beta_n \neq 0$ in general, D_n will only vanish when $C_n^2 = C_0^2$. To illustrate this, we present two examples, namely, those corresponding to parabolic and uniform injection.

First, for parabolic injection, one gets

$$D_{n,\text{parabolic}} \sim n(n+1)(2n+1)^{-2} \xrightarrow[n\to\infty]{} \frac{1}{4} \tag{2.64}$$

This term quickly converges to 1/4. In this case, the residual is sufficiently small, but nonzero because of the first few terms in (2.64).

Second, for the case of uniform injection, one collects

$$D_{n,\text{uniform}} \sim (-1)^n n(n+1)(2n+1)^{-1} \xrightarrow[n\to\infty]{} \infty \tag{2.65}$$

In this case, the residual is undefined because the alternating sequence of increasing terms in (2.65) diverges. This may be corroborated by the nature of the uniform profile due to its well known discontinuity at the sidewall.

In all cases, when the residual error converges, it is identically zero both along the centerline and at the chamber sidewall. Moreover, being independent of z, the residual becomes relatively smaller as we move away from the headwall. This relative decrease of the residual in the streamwise direction makes the approximation appropriate for long SRMs. The behavior is also consistent with the Taylor–Culick model which is known for its subtle discontinuity at $z = 0$. In all cases, the core flow approximations become increasingly more accurate away from the headwall, a condition that is compatible with the parallel flow assumption used in many stability studies of SRM flow fields.

2.5 Pressure evaluation

The steady momentum equations (2.4b) may be readily solved for the pressure distribution. One may start with $\mathbf{u}\cdot\nabla\mathbf{u} = -\nabla p$ and integrate in two spatial directions to retrieve, at length,

$$p = p_0 - \tfrac{1}{2}\mathbf{u}\cdot\mathbf{u} - \int u\frac{\partial w}{\partial r}\,dz \tag{2.66}$$

where $p_0 = p(0,0)$ represents the centerline pressure at the headwall. To guarantee an anlytical expression for the pressure, the total differential of the pressure must be exact, i.e.

$$\frac{\partial^2 p}{\partial r\partial z} = \frac{\partial^2 p}{\partial z\partial r} \tag{2.67}$$

This will be discussed at length in Chapter 3. In terms of the velocity field, (2.67) yields

$$u\frac{\partial^2 w}{\partial r^2} + w\frac{\partial^2 w}{\partial r\partial z} - \frac{u}{r}\frac{\partial w}{\partial r} = 0 \tag{2.68}$$

Therefore, (2.66) will produce an anlytical expression for the pressure whenever (2.68) is valid. For example, for the classic Taylor–Culick solution, (2.68) is identically satisfied and the pressure can be integrated to obtain

$$p(r,z) = p_0 - \tfrac{1}{2}\pi^2 z^2 - \tfrac{1}{2}r^{-2}\sin^2(\tfrac{1}{2}\pi r^2) \tag{2.69}$$

For the solution with a cosine injection profile,

$$\mathbf{u} = -r^{-1}\sin(\tfrac{1}{2}\pi r^2)\mathbf{e}_r + \pi(z+\mathrm{W}_h)\cos(\tfrac{1}{2}\pi r^2)\mathbf{e}_z \tag{2.70}$$

and (2.68) is also identically satisfied. Integration of the momentum equations yields

$$p(r,z) = p_0 - \tfrac{1}{2}\pi^2 z^2 - W_c\pi z - \tfrac{1}{2}r^{-2}\sin^2(\tfrac{1}{2}\pi r^2) \tag{2.71}$$

For uniform or parabolic injection, with axial velocities given by (2.40) and (2.48) respectively, the integrability constraint (2.68) is no longer satisfied. This is due

to the fact that the solutions are approximate. However, along the centerline, the constraint remains valid. Setting $r = 0$, the radial velocity shared by both injection profiles vanishes since

$$u(0, z) = \lim_{r \to 0} r^{-1} \sin(\tfrac{1}{2}\pi r^2) = 0 \tag{2.72}$$

while the axial velocities are equal at $r = 0$

$$w_{\text{uniform}}(0, z) = w_{\text{parabolic}}(0, z) = \pi z + W_{\text{c}} \tag{2.73}$$

Finally, the pressure may be integrated using (2.66) to yield

$$p(0, z) = p_0 - \tfrac{1}{2}\pi^2 z^2 - W_{\text{c}} \pi z \tag{2.74}$$

Interestingly, all injection profiles yield the same expression for the centerline pressure.

To overcome the pitfalls of the pressure integrability, approximate solutions of the pressure field can be obtained if one uses the following expansion

$$p(r, z) = \sum_{n=0}^{\infty} p_n(r, z) \tag{2.75}$$

where p_n is the pressure corresponding to the n^{th} eigenmode of the series solutions (2.24). Integration of the pressure in this case is possible because each eigensolution given by $\psi_n(r, z)$ is an exact solution of the Euler equations and thus satisfies (2.68). In other words,

$$u_n = -\alpha_n r^{-1} \sin \chi_n; \quad w_n = (2n + 1)\pi(\alpha_n z + \beta_n) \cos \chi_n \tag{2.76}$$

identically satisfy (2.68). Using Eqs. (2.3), one can integrate for the pressure to find, at length, and after using (2.29)

$$p_n(r, z) = p_0 - \tfrac{1}{2}(2n + 1)^2 \pi^2 \alpha_n^2 z^2 - (2n + 1)^2 \pi^2 \alpha_n \beta_n z - \tfrac{1}{2}\alpha_n^2 r^{-2} \sin^2 \chi_n \tag{2.77}$$

or

$$p(r,z) = \sum_{n=0}^{\infty} p_n = p_0 - \tfrac{1}{2}\pi^2 z^2 - \beta_0 \pi^2 z - \tfrac{1}{2} r^{-2} \sin^2(\tfrac{1}{2}\pi r^2) \tag{2.78}$$

As shown in Figure 2.8, this approximate expression stands in better agreement with the numerical data than the result obtained in (2.74) for the pressure based on the total velocity.

2.6 Origin of vorticity in the Taylor–Culick problem

An often unaddressed issue is the origin of vorticity in the Taylor–Culick inviscid model. While in practice, vorticity is produced by the action of viscosity at the injecting boundary, the inviscid model cannot account for such a mechanism in the absence of vorticity input through the sidewall (irrotational uniform injection). Helmholtz's vortex theorems are clear in that vorticity cannot be generated in an inviscid flow. Why then is there vorticity in the Taylor–Culick problem? The answer is very simple but it would be instructive to first revisit Helmholtz's theorems. We start by writing the incompressible vorticity transport equation for a fluid element (Panton 2005). This is

$$\frac{D\boldsymbol{\Omega}}{Dt} = \boldsymbol{\Omega} \cdot \nabla \mathbf{u} + \nu \nabla^2 \boldsymbol{\Omega} \tag{2.79}$$

In the absence of viscosity, we recover an ordinary differential equation

$$\frac{D\boldsymbol{\Omega}}{Dt} = \boldsymbol{\Omega} \cdot \nabla \mathbf{u} \tag{2.80}$$

Assuming that $\nabla \mathbf{u}$ is a known continuous function, then, (2.80) means that if $\boldsymbol{\Omega} = \mathbf{0}$ at $t = 0$, then it is zero at all times owing to the uniqueness of solutions for ordinary differential equations (Panton 2005). To show this more rigorously, Sommerfeld (1950) proves that, for a fluid element

$$\frac{D}{Dt} \left(\boldsymbol{\Omega} \cdot \mathbf{n} \, \mathrm{d}\mathcal{S} \right) = 0 \tag{2.81}$$

where $\mathbf{n}$ and $\mathrm{d}\mathcal{S}$ represent the normal unit vector and surface area of the fluid element, respectively. Equation (2.81) states that, *in an inviscid flow, the rate of change of the outflow of vorticity through the surface of a fluid element is zero.* Alternatively, if the outflow of vorticity through the surface of a fluid element is nonzero at some time t, then it will remain so for all subsequent times. This means that, in an incompressible inviscid flow, vorticity is convected with the fluid (Karamcheti 1966). This is the case in the inviscid Taylor–Culick problem where the vorticity field is initialized throughout the fluid domain by setting $\Omega = C^2 r\psi$ a priori in (2.16). In this respect, vorticity will remain unchanged at all subsequent times. There is no mechanism in this model to generate vorticity, neither at the sidewall, nor at the centerline.

2.7 Numerical verification

So far we have described an approximate Euler solution for the Taylor–Culick flow with variable headwall injection. By way of confirmation, we now present an inviscid numerical solution for the mean flow field using three illustrative headwall injection profiles. Our simulations are carried out using FLUENT, a commercial CFD code. The targeted flow is that corresponding to a rocket motor with an average sidewall Mach number of 0.03 and purely inviscid conditions. For the sake of comparison, the working fluid is taken to be ambient air. The aspect ratio of the domain is set at $L = 16$. The actual length and radius are taken at $1.6\,\mathrm{m} \times 0.1\,\mathrm{m}$ and the wall injection velocity is taken at 10 m/s for the simulated SRM. The boundary condition at the sidewall is specified as a velocity inlet to closely mimic the mathematical model where injection is imposed uniformly along the grain surface. The headwall is also specified as an inlet. On the right-hand-side of the domain, a pressure outlet boundary condition is prescribed where the exit pressure is set to be the atmospheric pressure corresponding to a firing at sea level. Although an outflow boundary condition can also be imposed at the downstream section, it is discounted here to avoid the possible case of partially developed flow (White 2005). The difference between an

outflow and a pressure outlet boundary condition is that, in the latter case, the exit pressure is fixed at the boundary. The domain is meshed into 589,824 equally spaced control volumes (3072×192). While the QUICK (Quadratic Upwind Interpolation for Convection Kinematics) scheme is called upon for spatial discretization, the SIMPLE (Semi Implicit Method for Pressure Linked Equation) algorithm is used to resolve the pressure–velocity coupling.

Results for the inviscid simulations are shown in Figures 2.6–2.8. These are carried out for $W_c = 1$ and 10 and show the streamwise evolution of the axial velocity, vorticity, and centerline pressure at $z/L = 0.1, 0.3, \ldots, 0.9$. It may be seen that the agreement with the computations is excellent except in the case of uniform injection with a large W_c. This may be attributed to the fact that the uniform injection profile carries a discontinuity at the sidewall. Furthermore, according to (2.65), we expect the residual error to be very large. These limited numerical experiments reaffirm the viability of the analytical approximations described above.

2.8 Summary

In this chapter we revisit the incompressible Taylor–Culick flow problem with arbitrary headwall injection. Several solutions are obtained that satisfy the principal constraints including the no slip requirement at the sidewall. Their behavior is illustrated for the cases of small and large headwall injection pertaining, for example, to SRM and hybrid rocket models, respectively. We find that the effect of varying the headwall injection profile to be small in sufficiently long chambers as they all evolve to the self-similar Taylor–Culick sinusoidal motion. However, it plays a key role in short chambers and T-burners where the foregoing formulations may be applied. The expressions presented here increase our repertoire of engineering approximations for the modeling of injection-driven porous tubes.

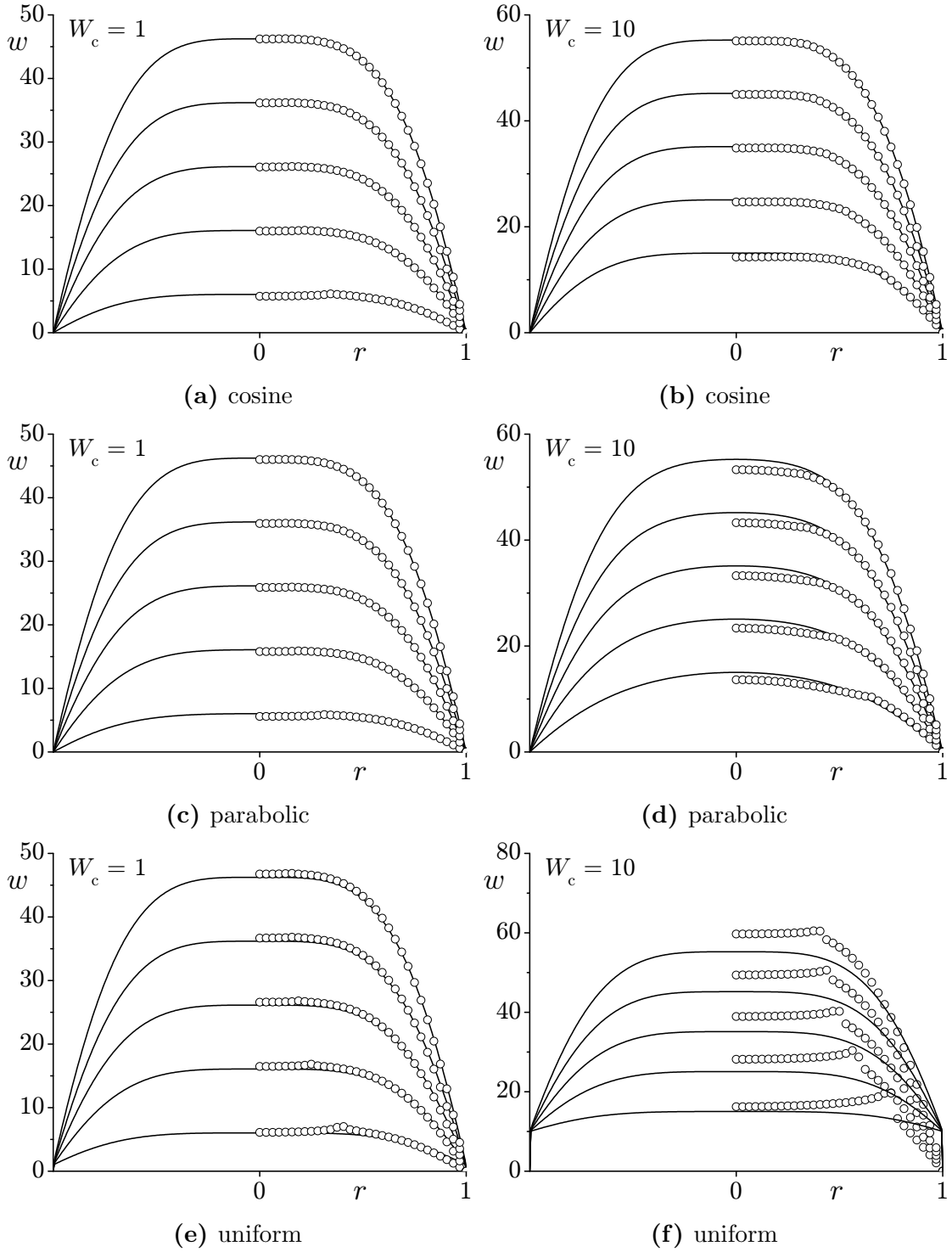

Figure 2.6: Comparison between analytical (—) and numerical simulations (○) for the axial velocity using (a, b) cosine, (c, d) parabolic, and (e, f) uniform injection. Curves are shown for $z/L = 0.1$, 0.3, 0.5, 0.7, and 0.9.

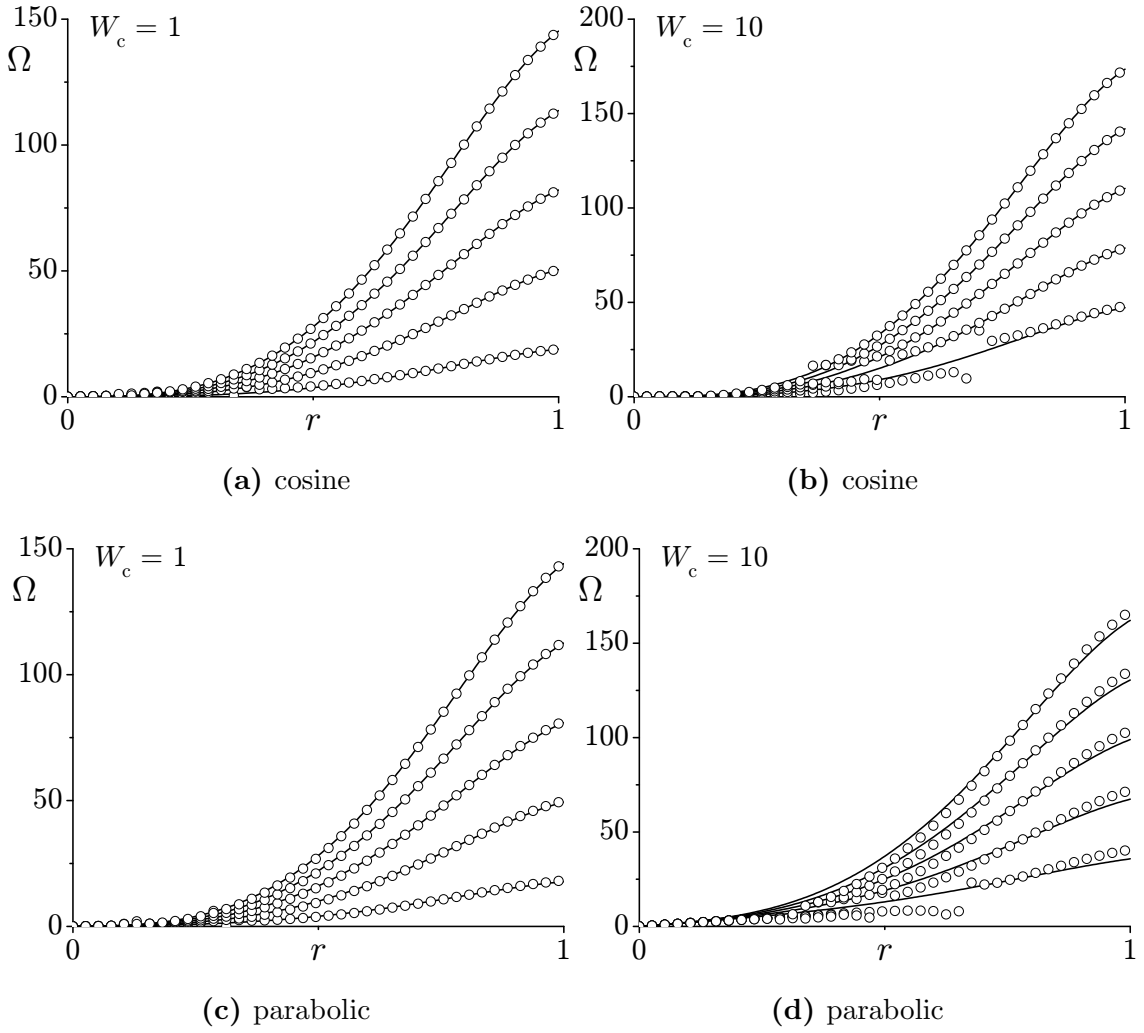

(a) cosine **(b)** cosine

(c) parabolic **(d)** parabolic

Figure 2.7: Comparison between analytical (—) and numerical simulations (○) for the vorticity magnitude using (a, b) cosine and (c, d) parabolic injection. Curves are shown for $z/L = 0.1$, 0.3, 0.5, 0.7, and 0.9.

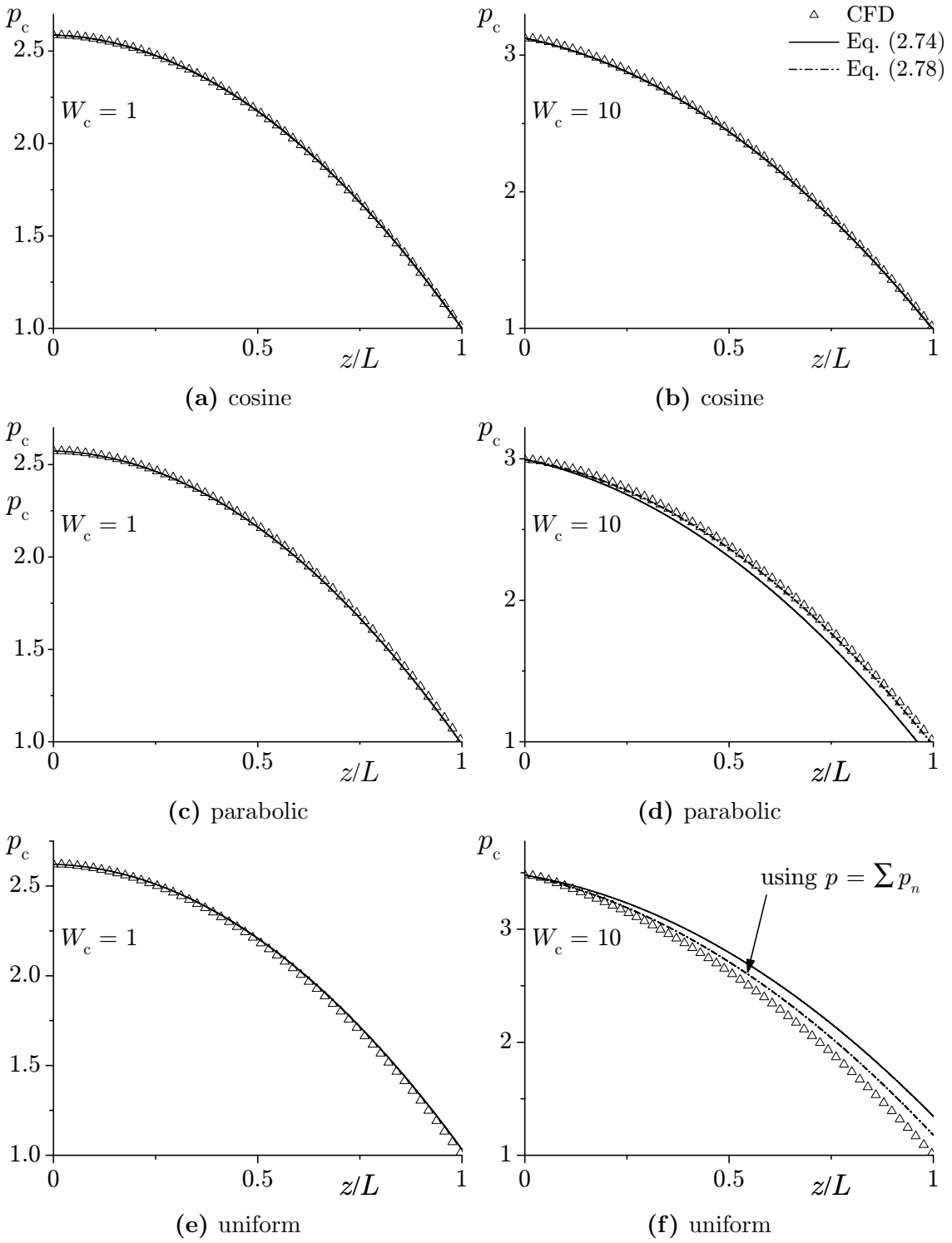

Figure 2.8: Comparison between analytical (—) for (2.74), (− · −) for (2.78) and numerical simulations (△) for the centerline pressure using (a, b) cosine, (c, d) parabolic, and (e, f) uniform injection. Curves are shown for $z/L = 0.1$, 0.3, 0.5, 0.7, and 0.9.

Chapter 3

Pressure Integration Constraints for the Navier-Stokes Equations

In §2.5, evaluation of the pressure required the use of a series expansion and the integration of each eigensolution independently due to the approximate nature of the solution. In this chapter, we discuss the details of pressure integration of the Navier-Stokes equations. The general problem can be formulated as follows: *given a velocity field that satisfies the continuity equation, we seek to identify the conditions under which the Navier-Stokes equations can be integrated to determine an analytical expression for the pressure.* The resulting constraints on the velocity field constitute necessary and sufficient conditions for obtaining an analytical expression for the pressure using direct integration. From a physical standpoint, these constraints represent a necessary condition for a given motion to be physically plausible. In this vein, a velocity field that does not satisfy the integrability constraints may be either unphysical or approximate.

3.1 Introduction

The equations of fluid motion represent a fascinating system of partial differential equations that has intrigued and challenged mathematicians and scientist alike over decades. The inherent nonlinearity and strong coupling embedded in these equations make it nearly impossible to tackle a traditional closed form solution except within the edifices of simplified models such as pipe flow, flows in porous channels, and similarly simple, nonetheless important configurations. To partially alleviate these difficulties, a multitude of flow regimes have been distinguished in an attempt to tackle the flow equations so that a practical solution may be attained. For instance, one may consider the flow to be irrotational, isentropic, inviscid rotational, diffusive (creeping flows), viscous with a prescribed pressure gradient, or of the boundary layer type. Of course, each of these approximations bears certain deficiencies, but is still able to capture the essential physics of the flow under examination. These idealizations are usually accompanied by specific solution methodologies such as the use of a velocity potential for irrotational flows, vorticity-streamfunction formulations when the motion is inviscid and rotational, similarity transforms for boundary layers and so on.

Our current understanding of the mechanics of fluids eclipses quite a turbulent yet engaging history. Although most of the hydrostatic principles were known by the early 18th century thanks to a host of scientists such as Evangelista Torricelli, Christiaan Huygens, Edme Mariotte, Isaac Newton, and Daniel Bernoulli; the theoretical formulation was very timidly treated and had to wait until the middle of the 18th century. Four key figures play the central role in advancing the theory of fluid mechanics: Alexis Clairaut for his work on differential forms, Jean le Rond d'Alembert for his propositions of the differential treatment of fluids, Leonhard Euler for his synthesis, notation, and rigorous generalizations of the previous works, and finally Joseph Louis Lagrange for proposing some techniques for the resolution of these equations such as perturbation methods.

Starting with Clairaut's attempts to find the curvature of the earth and solve the problem of whether there is flattening at the poles (Clairaut 1739, 1740), his theorem on exact differentials proved to be essential for the subsequent studies. In essence, he derived the constraints for a total differential to be exact. In fact, he is well known in differential calculus for his theorem on the continuity of mixed derivatives. About a decade later, in 1749, d'Alembert presented his research on the theory of fluid mechanics to the Academy of Sciences of Berlin. But it was not until 1755 that he officially published his manuscript. Euler was the first to ever address the problem of fluid mechanics in a *pure* and problem independent manner (Calero 2008). In this regard, he is most famous for four manuscripts (Euler 1752, 1755a,b,c), all published in the early 1750's and contain the theoretical foundation of fluid mechanics. In fact, most of the fundamental theory of fluids that is taught today was handed down to us by Euler. Finally, Lagrange, a pupil of Euler, presents his work on the motion of fluids. His focus was no longer on a theoretical treatment, but rather, on the resolution of the governing equations. Hence, he presented several scenarios for which the flow equations may be solved. He is also credited for being the first to use perturbation methods to solve fluid mechanics problems (Calero 2008).

In their most general form, the equations of fluid motion cover the effects of accumulation (time dependence), viscous forces, compressibility, and body forces. They consist of four equations; the continuity equation that expresses the kinematic condition for the fluid or simply conservation of mass and three momentum equations that embody the dynamical effects and assert the balance of internal and external forces on the evolution of the flow field.

The most remarkable feature of these equations is the wealth of physics that they consolidate. For example, they can be used for both laminar and turbulent flows although the physical processes that accompany these flow regimes are quite dissimilar. In this chapter, we focus on the incompressible fluid flow equations, i.e. the Navier-Stokes equations, and investigate one of their physical features. Specifically, we state our problem as follows: *given a velocity field that satisfies the continuity*

equation, we seek to identify the conditions under which the Navier-Stokes equations can be integrated to determine an analytic expression for the pressure. The resulting nonlinear constraints constitute a necessary and sufficient condition for obtaining the pressure via direct integration when possible.

This chapter is organized as follows. First, we illustrate the process of integrating the two dimensional Euler equations from which we are able to extract the pressure integrability principle. Then, this principle is applied to the three dimensional Navier-Stokes equations from which three constraints are obtained in a rigorous and generalized manner. Finally, a list of implications and pertinent examples is presented.

3.2 Integration of the Euler equations

The two dimensional steady state Euler equations are written in normalized form as

$$\frac{\partial u}{\partial x} + \frac{\partial v}{\partial y} = 0 \tag{3.1}$$

$$\frac{\partial p}{\partial x} = -u\frac{\partial u}{\partial x} - v\frac{\partial u}{\partial y} = -\mathbf{u}\cdot\nabla u \tag{3.2}$$

$$\frac{\partial p}{\partial y} = -u\frac{\partial v}{\partial x} - v\frac{\partial v}{\partial y} = -\mathbf{u}\cdot\nabla v \tag{3.3}$$

Given a velocity field that satisfies (3.1), we wish to solve (3.2) and (3.3) for the pressure. One may first integrate (3.2) with respect to the axial coordinate

$$p(x,y) = \int \frac{\partial p}{\partial x}\,\mathrm{d}x = -\int u\frac{\partial u}{\partial x}\,\mathrm{d}x - \int v\frac{\partial u}{\partial y}\,\mathrm{d}x + \mathcal{G}(y) \tag{3.4}$$

where $\mathcal{G}(y)$ is an arbitrary function of y. Substitution of (3.4) into (3.3) yields the differential equation for $\mathcal{G}(y)$

$$\frac{\partial \mathcal{G}}{\partial y} = -u\frac{\partial v}{\partial x} - v\frac{\partial v}{\partial y} + \frac{\partial}{\partial y}\int u\frac{\partial u}{\partial x}\,\mathrm{d}x + \frac{\partial}{\partial y}\int v\frac{\partial u}{\partial y}\,\mathrm{d}x \tag{3.5}$$

A necessary condition to be able to carry out the integration is that (3.5) is a function of y only. Therefore, this may be enforced by taking the partial derivative of (3.5) with respect to x and setting it equal to zero

$$\frac{\partial^2 \mathcal{G}}{\partial x \partial y} = -\frac{\partial}{\partial x}\left(u\frac{\partial v}{\partial x}\right) - \frac{\partial}{\partial x}\left(v\frac{\partial v}{\partial y}\right) + \frac{\partial}{\partial y}\left(u\frac{\partial u}{\partial x}\right) + \frac{\partial}{\partial y}\left(v\frac{\partial u}{\partial y}\right) = 0 \tag{3.6}$$

or

$$\frac{\partial}{\partial x}\left(\mathbf{u}\cdot\nabla v\right) - \frac{\partial}{\partial y}\left(\mathbf{u}\cdot\nabla u\right) = 0 \tag{3.7}$$

The constraint given by (3.7) guarantees an anlytic expression for the pressure field provided that the velocity field satisfies the continuity equation. Using (3.2) and (3.3), we write (3.7) as

$$\frac{\partial^2 p}{\partial x \partial y} = \frac{\partial^2 p}{\partial y \partial x} \tag{3.8}$$

Equation (3.8) is known as Clairaut's theorem (Blank and Krantz 2006, pp. 226) also referred to as Schwarz theorem by some scholars (Doussineau and Levelut 2002). Clairaut's theorem states that *'the mixed second derivatives of a continuous function f on a domain $\mathcal{D}$ are equal iff its mixed derivatives f_{xy} and f_{yx} are continuous on $\mathcal{D}$'* (Rogawski 2008, pp. 814). Therefore, (3.8) is satisfied when p_{xy} and p_{yx} are continuous on all points of the fluid domain. Equation (3.8) also implies that the total differential of the pressure

$$\mathrm{d}p = \frac{\partial p}{\partial x}\,\mathrm{d}x + \frac{\partial p}{\partial y}\,\mathrm{d}y \tag{3.9}$$

should be exact (Price 1857, pp. 349). This simple, yet powerful result may now be easily generalized to three dimensions for viscous flows.

3.3 Integrability of the Navier-Stokes equations

The results given in §3.2 are now extended to the three dimensional Navier-Stokes equations with constant properties. These are given by (see Hughes and Gaylord

1964)

$$\nabla \cdot \mathbf{u} = 0 \tag{3.10}$$

and

$$\rho \frac{\partial \mathbf{u}}{\partial t} + \rho \mathbf{u} \cdot \nabla \mathbf{u} = -\nabla p + \mu \nabla^2 \mathbf{u} + \mathbf{B} \tag{3.11}$$

where ρ is the fluid density, μ is the molecular viscosity, and $\mathbf{B}$ is the body force vector per unit volume.

Theorem 3.1. *Given a velocity field* $\mathbf{u}$ *of class* C^2 *in a fluid region* $\mathcal{V}$ *that satisfies the continuity equation (3.10), then the momentum equations (3.11) can be integrated for the pressure to within a constant if the following constraints are satisfied*

$$\frac{\partial^2 p}{\partial x_1 \partial x_2} = \frac{\partial^2 p}{\partial x_2 \partial x_1}; \quad \frac{\partial^2 p}{\partial x_2 \partial x_3} = \frac{\partial^2 p}{\partial x_3 \partial x_2}; \quad \frac{\partial^2 p}{\partial x_1 \partial x_3} = \frac{\partial^2 p}{\partial x_3 \partial x_1} \tag{3.12}$$

Proof. For convenience, we write 3.11 in general curvilinear orthogonal coordinates as

$$\frac{\partial p}{\partial x_i} = \mathscr{F}_i(x_1, x_2, x_3, t); \quad i = 1, 2, 3 \tag{3.13}$$

Integration of (3.13) in the x_1 direction yields

$$p = \int \frac{\partial p}{\partial x_1} \, \mathrm{d}x_1 = \int \mathscr{F}_1 \, \mathrm{d}x_1 + \mathcal{G}_1(x_2, x_3, t) \tag{3.14}$$

upon substitution into the x_2 momentum equation, we get

$$\frac{\partial p}{\partial x_2} = \mathscr{F}_2 = \frac{\partial}{\partial x_2} \int \mathscr{F}_1 \, \mathrm{d}x_1 + \frac{\partial \mathcal{G}_1(x_2, x_3, t)}{\partial x_2} \tag{3.15}$$

however, $\mathcal{G}_1$ is a function of x_2, x_3, and t only, one may therefore impose the following constraint

$$\frac{\partial^2 \mathcal{G}_1}{\partial x_1 \partial x_2} = 0 \tag{3.16}$$

in other words, and by using (3.15)

$$\frac{\partial^2 \mathcal{G}_1}{\partial x_1 \partial x_2} = \frac{\partial \mathscr{F}_2}{\partial x_1} - \frac{\partial \mathscr{F}_1}{\partial x_2} = 0 \tag{3.17}$$

but, by virtue of (3.13), (3.17) will require that

$$\frac{\partial^2 p}{\partial x_1 \partial x_2} = \frac{\partial^2 p}{\partial x_2 \partial x_1} \tag{3.18}$$

In a similar fashion, substitution of (3.14) into the x_3 momentum equation yields the second constraint

$$\frac{\partial^2 p}{\partial x_1 \partial x_3} = \frac{\partial^2 p}{\partial x_3 \partial x_1} \tag{3.19}$$

Finally, (3.13) is integrated in the x_2 direction

$$p = \int \frac{\partial p}{\partial x_2} \, \mathrm{d}x_2 = \int \mathscr{F}_2 \, \mathrm{d}x_2 + \mathcal{G}_2(x_1, x_3, t) \tag{3.20}$$

upon substitution into the x_3 momentum equation, we get

$$\frac{\partial p}{\partial x_3} = \mathscr{F}_3 = \frac{\partial}{\partial x_3} \int \mathscr{F}_2 \, \mathrm{d}x_2 + \frac{\partial \mathcal{G}_2(x_1, x_3, t)}{\partial x_3} \tag{3.21}$$

however, $\mathcal{G}_2$ is a function of x_1, x_3, and t only, one may therefore impose the following constraint

$$\frac{\partial^2 \mathcal{G}_2}{\partial x_2 \partial x_3} = 0 \tag{3.22}$$

in other words, by using (3.21) and (3.13), we get

$$\frac{\partial^2 p}{\partial x_2 \partial x_3} = \frac{\partial^2 p}{\partial x_3 \partial x_2} \tag{3.23}$$

One then concludes that a necessary and sufficient condition for obtaining an anlytic expression for the pressure field via integration of the momentum equations is that the constraints given by (3.18), (3.19), and (3.23) are satisfied. □

Corollary 3.1.1. *The pressure is integrable if its total differential is exact.*

Proof. In general orthogonal coordinates, the total differential of the pressure may be written as

$$dp = \frac{\partial p}{\partial x_1}\,\mathrm{d}x_1 + \frac{\partial p}{\partial x_2}\,\mathrm{d}x_2 + \frac{\partial p}{\partial x_3}\,\mathrm{d}x_3 = F\,\mathrm{d}x_1 + G\,\mathrm{d}x_2 + H\,\mathrm{d}x_3 \tag{3.24}$$

Note that the time derivative of the pressure was not included in (3.24) because it is not specified and is therefore irrelevant in the subsequent steps of this proof. Equation (3.24) is exact if

$$\frac{\partial H}{\partial x_2} = \frac{\partial G}{\partial x_3}; \quad \frac{\partial F}{\partial x_3} = \frac{\partial H}{\partial x_1}; \quad \frac{\partial G}{\partial x_1} = \frac{\partial F}{\partial x_2} \tag{3.25}$$

(see Price 1857, pp. 349). In terms of the pressure,

$$\frac{\partial p}{\partial x_1 \partial x_2} = \frac{\partial p}{\partial x_2 \partial x_1}; \quad \frac{\partial p}{\partial x_2 \partial x_3} = \frac{\partial p}{\partial x_3 \partial x_2}; \quad \frac{\partial p}{\partial x_1 \partial x_3} = \frac{\partial p}{\partial x_3 \partial x_1} \tag{3.26}$$

which reproduces Theorem 3.1. □

Corollary 3.1.2. *The pressure is integrable iff the velocity field satisfies the vorticity equation.*

Proof. The conditions given by (3.12) are equivalent to the vector identity

$$\nabla \times \nabla p = \mathbf{0} \tag{3.27}$$

This condition is true iff the pressure is at least of class C^2. While a velocity field may satisfy mass conservation, it may not be able to generate a pressure field that is twice differentiable and continuous. To ensure that the velocity field will generate a pressure that satisfies (3.27), one may take the curl of (3.11) and enforce (3.27), to obtain

$$\rho \frac{\partial \boldsymbol{\Omega}}{\partial t} - \rho \nabla \times \mathbf{u} \times \boldsymbol{\Omega} - \mu \nabla^2 \boldsymbol{\Omega} = \mathbf{0} \tag{3.28}$$

which is nothing else but the vorticity transport equation. Therefore, one concludes that if the velocity field satisfies (3.28) then (3.27) is successfully enforced. □

Corollary 3.1.3. *In perturbation methods, each order of the pressure must satisfy the integrability constraints applied to that order.*

Proof. In a regular perturbation treatment, the pressure may be expanded as

$$p = \sum_{n=0}^{\infty} \varepsilon^n p_n \tag{3.29}$$

where $|\varepsilon| << 1$. Being linear, substitution into (3.12) warrants that every order of the pressure p_n satisfies the constraints (3.27). □

3.4 Implications and examples

The ideas presented in the previous section all concur to the fact that the vorticity transport equation plays a significant role in determining the characteristics of a flow field. Even if a velocity field satisfies mass conservation, it will not guarantee the integrability of an analytic pressure field unless the vorticity transport equation is also satisfied. In other words, the vorticity transport equation guarantees the symmetry of the second derivatives for the pressure and therefore its continuity on the domain of interest.

To illustrate the process of using the integrability constraints, we select a few well known cases and attempt to solve for the pressure. In certain scenarios, the integrability constraints are substantially simplified and therefore constitute a concise benchmark check for the validity of a given solution.

3.4.1 Potential flows

For potential flows, it is straightforward to show that the condition of irrotationality is a special case of the integrability constraints. When $\boldsymbol{\Omega} = \mathbf{0}$, the vorticity transport

equation (3.28) is identically validated and the conditions of integrability given in (3.27) are always satisfied. Although irrotationality is a valid solution in this case, it is not the only solution. This result illustrates the fact that all potential flow solutions will guarantee the integrability of the momentum equations to extract the pressure.

3.4.2 Inviscid rotational flows

When the flow is inviscid, the vorticity transport equation reduces to

$$\frac{\partial \mathbf{\Omega}}{\partial t} - \nabla \times \mathbf{u} \times \mathbf{\Omega} = \mathbf{0} \tag{3.30}$$

Since $\mathbf{\Omega} = \mathbf{0}$ is a trivial solution in this case, one has to seek alternative solutions. Numerous problems that fall under this category of flows have been successfully treated, the most prominent of which are in the area of propulsion. In fact, these refer to the Taylor and Taylor–Culick flows that were described at length in Chapter 2. For the Taylor flow in a porous channel (planar case), the streamfunction is given by

$$\psi = x \sin(\tfrac{1}{2}\pi y) \tag{3.31}$$

while the velocity field is

$$\mathbf{u} = \tfrac{1}{2}\pi x \cos(\tfrac{1}{2}\pi y)\mathbf{i} - \sin(\tfrac{1}{2}\pi y)\mathbf{j} \tag{3.32}$$

where x and y stand for the axial and transverse coordinates respectively. In this case, the integrability constraint takes the following form

$$u\frac{\partial^2 u}{\partial x \partial y} + v\frac{\partial^2 u}{\partial y^2} = 0 \tag{3.33}$$

with u and v representing the axial and transverse velocities, respectively. It may be easily verified that the solution given by (3.32) satisfies (3.33) identically. At the

outset, the pressure is integrated as

$$p(x,y) = p_0 - \frac{1}{8}[\pi^2 x^2 + 2 - 2\cos(\pi y)] \tag{3.34}$$

where $p_0 = p(0,0)$ is the center pressure at the channel headwall. Similarly, Culick's solution for the flow in a porous cylinder is described by the streamfunction

$$\psi = z\sin(\tfrac{1}{2}\pi r^2) \tag{3.35}$$

while the velocity field, using the Stokes streamfunction, is

$$\mathbf{u} = -r^{-1}\sin(\tfrac{1}{2}\pi r^2)\mathbf{e}_r + \pi z\cos(\tfrac{1}{2}\pi r^2)\mathbf{e}_z \tag{3.36}$$

where r and z are the radial and axial coordinates respectively. For this case, the integrability constraint simplifies to

$$u\frac{\partial^2 w}{\partial r^2} + w\frac{\partial^2 w}{\partial r \partial z} - \frac{u}{r}\frac{\partial w}{\partial r} = 0 \tag{3.37}$$

where u and w stand for the radial and axial velocities, respectively. It may be easily shown that the velocity field given by (3.36) satisfies (3.37) identically. The pressure may be easily extracted as

$$p(r,z) = p_0 - \tfrac{1}{2}\pi^2 z^2 - \tfrac{1}{2}r^{-2}\sin^2(\tfrac{1}{2}\pi r^2) \tag{3.38}$$

An interesting case of Taylor–Culick's problem arises when one attempts to account for arbitrary injection at the headwall of the domain as it gives rise to a velocity field that violates the pressure integrability constraint although it satisfies mass conservation. These solutions were discussed in Chapter 2 and may be found in previous articles by Majdalani and Saad (2007) and Saad and Majdalani (2009b). The reason for this delicate behavior of the flow field is that the solutions are approximate

and that, in essence, they represent a solution to an approximate form of the vorticity transport equation. To illustrate this behavior, we pick the solution corresponding to a parabolic injection profile at the headwall for the planar channel case (Majdalani and Saad 2007). This is given by

$$u(0,y) = 1 - y^2 \tag{3.39}$$

while the corresponding velocity field is given by*

$$\mathbf{u} = \left[\tfrac{1}{2}\pi x \cos(\tfrac{1}{2}\pi y) + f(y)\right] \mathbf{e}_x - \sin(\tfrac{1}{2}\pi y)\mathbf{e}_y; \tag{3.40}$$

where

$$f(y) \equiv \frac{32}{\pi^3} \sum_{n=0}^{\infty} \frac{(-1)^n}{(2n+1)^3} \cos\left[(n+\tfrac{1}{2})\pi y\right] \tag{3.41}$$

It is easy to show that (3.40) does not satisfy (3.33). To further illustrate the reason for this, we attempt to integrate the momentum equations. Starting with the y direction

$$p(x,y) = \int \frac{\partial p}{\partial y}\, \mathrm{d}y = -\int v \frac{\partial v}{\partial y}\, \mathrm{d}x + \mathcal{G}(x) = -\tfrac{1}{4}\cos(\pi y) + \mathcal{G}(x) \tag{3.42}$$

By substituting (3.42) into the x-momentum equation, one must satisfy

$$\frac{\partial p}{\partial x} = \frac{\partial \mathcal{G}(x)}{\partial x} = -u\frac{\partial u}{\partial x} - v\frac{\partial u}{\partial y} \tag{3.43}$$

According to (3.42), $\mathcal{G}(x)$ is a function of x only and therefore, (3.43) must be a function of x as well. However, a closer look at its right-hand-side (RHS) reveals that it is a function of x and y since

$$u\frac{\partial u}{\partial x} + v\frac{\partial u}{\partial y} = \tfrac{1}{4}\pi^2 x + \tfrac{1}{2}\pi\cos(\tfrac{1}{2}\pi y) f(y) - \sin(\tfrac{1}{2}\pi y) f'(y) \tag{3.44}$$

*As outlined in the nomenclature, for the channel configuration, u, v, and w stand for the axial, transverse, and spanwise velocities, respectively.

Therefore, although the velocity field (3.40) is divergence free, it does not allow direct analytical integration of the pressure. This may be attributed to the fact that this solution is approximate. Interestingly enough, the constraints given by (3.12) are not restrictive on the domain of applicability in that the pressure may be uniquely determined in any subdomain on which (3.12) apply. In fact, if one restricts the domain of interest to the centerline, $y = 0$, then (3.43) is a function of x only and the pressure can be determined via

$$p(x, 0) = p_0 - \frac{1}{8}\pi x(\pi x + 4) \tag{3.45}$$

where $p_0 = p(0, 0)$ is the centerline pressure at the headwall.

3.4.3 Series solutions

For series solutions, such as those given in Chapter 2, the velocity constraints may not be satisfied in general since most series solutions stem from a linearization process. The alternative is to write the pressure as a summation of particular solutions

$$p = \sum p_n \tag{3.46}$$

where p_n corresponds to a particular, generally exact solution. An example of this was given in §2.5.

3.5 Summary

In this chapter, we derive a set of constraints that, if satisfied, represent a necessary and sufficient condition for obtaining an analytic expression for the pressure by direct integration of the momentum equations. Given a velocity field that satisfies the continuity equation, it must also satisfy these constraints in order for a plausible fluid motion to exist. The continuity equation is only a necessary condition for the

establishment of a flow field (Euler 1752). While the momentum equations describe the force balance that is needed to sustain fluid motion, the exactness of the total differential of the pressure must be met in order for them to be integrated. Therefore, the equality of the cross derivatives of the momentum equations is a necessary and sufficient condition for sustaining a given fluid motion.

Chapter 4

Variational Solutions

In Chapter 2, we presented a mean flow model for solid and hybrid rocket motors that is able to entertain an arbitrary injection profile at the headwall. The solutions were presented in series form and depended on two sequences, α_n and β_n, the sidewall and headwall injection sequences. The choice of α_n was found to be arbitrary provided that the constraint given by (2.26) is observed. In this chapter, we apply the Lagrangian optimization technique to the total volumetric kinetic energy of the Taylor–Culick flow to identify a general representation for α_n. Subsequently, two families of solutions are determined with increasing or decreasing kinetic energies of which the Taylor–Culick model is recovered as a special case. These exhibit velocity profiles with energy dependent curvatures that are reminiscent of turbulent or compressible motions. In practice, steeper or smoother profiles have been observed in either experimental or numerical tests, particularly in the presence of intense levels of acoustic energy (Apte and Yang 2000, 2001, 2002). Interestingly, it is found that both types cover a wide spectrum of admissible motions ranging from purely irrotational to highly rotational fields. Finally, a second law analysis allows us to explain the physicality of these new solutions and to pinpoint the Taylor–Culick solution as an equilibrium state to which all profiles will tend to converge.

4.1 Energy driven solutions

The sidewall injection sequence was discussed in Chapter 2 and is defined through the following constraint

$$\sum_{n=0}^{\infty}(-1)^n\alpha_n = 1 \tag{4.1}$$

Clearly, innumerable possibilities exist that can be made to satisfy (4.1) depending on the behavior of α_n.

4.1.1 Kinetic energy optimization

One of the choices for α_n may be arrived at by optimizing the total volumetric kinetic energy in the chamber. The guiding principle is based on the fact that a flow may follow the path of least or most energy expenditure. To test this behavior, we evaluate the local kinetic energy at (r, θ, z), for each eigensolution, using

$$E_n(r,\theta,z) = \tfrac{1}{2}\mathbf{u}_n^2 = \tfrac{1}{2}(u_n^2 + v_n^2 + w_n^2) \tag{4.2}$$

where each mode is an exact solution given by

$$\begin{cases} u_n = -r^{-1}\alpha_n \sin\chi_n; \quad v_n = 0; \\ w_n = \pi\alpha_n z(2n+1)\cos\chi_n; \end{cases} \qquad \chi_n = (n+\tfrac{1}{2})\pi r^2 \tag{4.3}$$

We now define the cumulative local kinetic energy as the sum of contributions from individual eignsolutions. This can be written as

$$E(r,\theta,z) = \sum_{n=0}^{\infty} E_n(r,\theta,z) = \tfrac{1}{2}\sum_{n=0}^{\infty}\left[\alpha_n^2 r^{-2}\sin^2\chi_n + \pi^2\alpha_n^2 z^2(2n+1)^2\cos^2\chi_n\right] \tag{4.4}$$

Subsequently, the total kinetic energy in the chamber volume $\mathcal{V}$ may be calculated by integrating the local kinetic energy over the length and chamber cross-section,

$$\begin{aligned} E_{\mathcal{V}} &= \iiint_{\mathcal{V}} E(r,\theta,z) r \,\mathrm{d}r \,\mathrm{d}\theta \,\mathrm{d}z \\ &= \pi \sum_{n=0}^{\infty} \int_0^L \int_0^1 \alpha_n^2 \left[\frac{\sin^2 \chi_n}{r^2} + \pi^2 z^2 (2n+1)^2 \cos^2 \chi_n \right] r \,\mathrm{d}r \,\mathrm{d}z \end{aligned} \tag{4.5}$$

Straightforward evaluation and simplification yield

$$E_{\mathcal{V}} = \tfrac{1}{12}\pi^3 L^3 \sum_{n=0}^{\infty} (\alpha_n^2 a_n + \alpha_n^2 \pi^{-2} L^{-2} d_n); \quad \begin{cases} a_n = (2n+1)^2 \\ d_n = 3\mathrm{Cin}[(2n+1)\pi] \end{cases} \tag{4.6}$$

Here, $\mathrm{Cin}(x) \equiv \int_0^x (1-\cos t) t^{-1} \,\mathrm{d}t$ is the Entire cosine Integral. At this point, one may seek the extremum of (4.6) subject to the fundamental constraint

$$\sum_{n=0}^{\infty} (-1)^n \alpha_n = 1 \tag{4.7}$$

Equation (4.7) enables us to introduce the constrained energy function

$$\mathcal{G}(\alpha_0, \alpha_1, \alpha_2, \ldots, \lambda) = E_{\mathcal{V}} + \lambda \left[\sum_{n=0}^{\infty} (-1)^n \alpha_n - 1 \right] \tag{4.8}$$

where λ is a Lagrangian multiplier. Equation (4.8) can be maximized or minimized by imposing $\nabla \mathcal{G}(\alpha_0, \alpha_1, \alpha_2, \ldots, \lambda) = 0$. In shorthand notation, we put

$$\nabla \mathcal{G}(\alpha_n, \lambda) = 0; \quad n \in \mathbb{N}_0 \tag{4.9}$$

Subsequently, the constrained energy function may be differentiated with respect to each of its variables to obtain

$$\frac{\partial \mathcal{G}}{\partial \alpha_n} = \tfrac{1}{6}\pi^3 L^3 \left(\alpha_n a_n + \frac{\alpha_n d_n}{\pi^2 L^2} \right) + (-1)^n \lambda = 0 \tag{4.10}$$

and

$$\frac{\partial \mathcal{G}}{\partial \lambda} = \sum_{n=0}^{\infty} (-1)^n \alpha_n - 1 = 0 \tag{4.11}$$

Equation (4.10) can be solved for α_n in terms of λ such that

$$\alpha_n = -\frac{6(-1)^n \lambda}{\pi^3 L^3 (a_n + \pi^{-2} L^{-2} d_n)} \tag{4.12}$$

Then, through substitution into (4.11), one retrieves

$$\lambda = -\frac{\pi^3 L^3}{6 \sum_{n=0}^{\infty} (a_n + \pi^{-2} L^{-2} d_n)^{-1}} \tag{4.13}$$

Finally, when λ is inserted into (4.12), a general solution for α_n emerges, specifically

$$\alpha_n = \frac{(-1)^n}{(a_n + \pi^{-2} L^{-2} d_n) N}; \quad N = \sum_{i=0}^{\infty} \frac{1}{a_i + \pi^{-2} L^{-2} d_i} \tag{4.14}$$

Clearly, (4.14) satisfies the fundamental constraint via

$$\sum_{n=0}^{\infty} (-1)^n \alpha_n = \frac{1}{N} \sum_{n=0}^{\infty} \frac{1}{(a_n + \pi^{-2} L^{-2} d_n)} = \frac{N}{N} = 1 \tag{4.15}$$

Some values of α_n are posted in Table 4.1 for various values of L. With this expression at hand, the total energy given by (4.6) is fully determined.

Table 4.1: Convergence of the sidewall injection sequence α_n for $L = 1, 5, 10$, and 100.

n	$L = 1$	$L = 5$	$L = 10$	$L = 100$
0	0.7524	0.8095	0.8115	0.8121
1	-0.1146	-0.0914	-0.0905	-0.0902
2	0.0434	0.0329	0.0326	0.0324
3	-0.0225	-0.0168	-0.0166	-0.0165
4	0.0137	0.0101	0.0100	0.0100
5	-0.0092	-0.0068	-0.0067	-0.0067

4.1.2 Critical length

A close inspection of (4.6) reveals that it can be written in a more convenient form, such as an energy density based on the chamber length. This can be accomplished by setting

$$\mathscr{E} = \frac{E_{\mathcal{V}}}{L^3} \tag{4.16}$$

Then, by plotting $\mathscr{E}$ versus L in Figure 4.1, we are able to observe the energy density variation as the chamber length is increased at fixed radius. It is interesting to note that, opposite to what one would expect, the energy density approaches a constant asymptotic value of $\mathscr{E}_\infty = 2\pi/3$. Granted this behavior, a critical aspect ratio L_{cr} can be defined beyond which the energy density will vary by less than one percent from its asymptotic value $\mathscr{E}_\infty$, i.e.

$$\mathscr{E}_{\text{cr}} - \mathscr{E}_\infty \leq 0.01\, \mathscr{E}_\infty \tag{4.17}$$

Subsequently, for a chamber of length $L \geq L_{\text{cr}}$, one may evaluate the limiting behavior of (4.14) by taking $L \to \infty$. For SRMs with inert headwalls, the critical length is found to be 6.7. However, in practice, most SRMs are designed with an aspect ratio that exceeds 20; thus, the assumption of a large L may be safely employed.

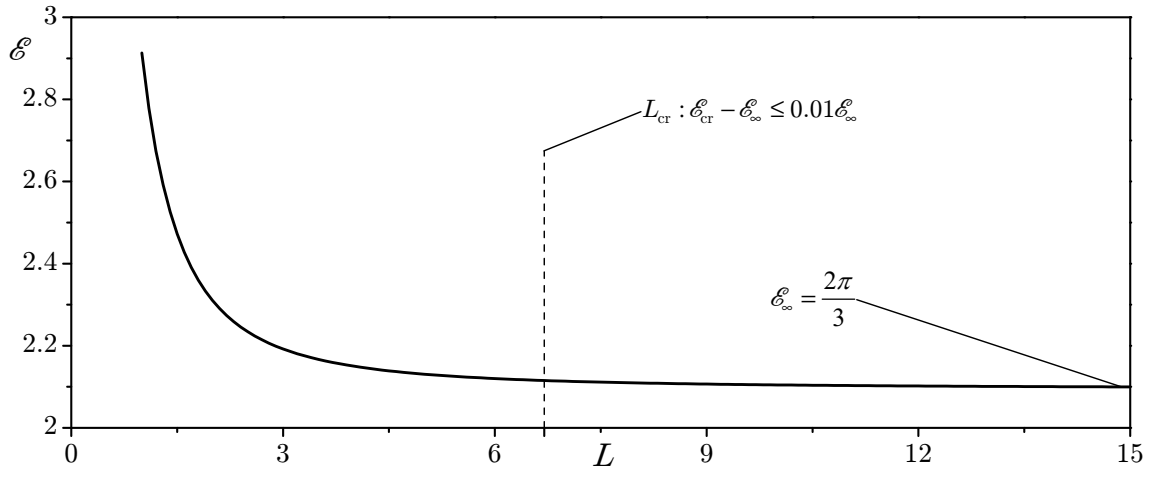

Figure 4.1: Kinetic energy density variation with the chamber length.

The resulting form of α_n is now at hand

$$\lim_{L\to\infty} \alpha_n = (-1)^n \left(a_n \sum_{i=0}^{\infty} \frac{1}{a_i} \right)^{-1} = \frac{8(-1)^n}{\pi^2(2n+1)^2} \tag{4.18}$$

Note that (4.18) identically satisfies the fundamental constraint expressed through (4.7) since

$$\sum_{n=0}^{\infty} (-1)^n \alpha_n = \frac{8}{\pi^2} \sum_{n=0}^{\infty} \frac{1}{(2n+1)^2} = 1 \tag{4.19}$$

Its convergence properties are illustrated in Table 4.2.

4.1.3 Least kinetic energy solution

While the use of Lagrangian multipliers enabled us to identify the problem's extremum, straightforward substitution of (4.14) into (4.6) allows one to compare the energy content of the present approximation to that of Taylor–Culick's. We find that the extremum solution that was exposed corresponds to the solution with least kinetic energy. For an inert headwall, the minimum energy solution collapses into

$$\psi(r,z) = \frac{8}{\pi^2} z \sum_{n=0}^{\infty} \frac{(-1)^n}{(2n+1)^2} \sin \chi_n \mapsto r^2 z \tag{4.20}$$

The right–oriented arrow '$\mapsto$' in (4.20) is used to indicate that the reduced expression is valid inside the domain, $0 \leq r < 1$. Note that, in evaluating (4.20), the large

Table 4.2: Convergence of the sidewall injection sequence α_n when $L \to \infty$.

m	α_m	$\sum_{n=0}^{m}(-1)^n\alpha_n$
0	0.8105	0.8105
1	-0.0900	0.9006
2	0.0324	0.9330
3	-0.0165	0.9495
4	0.0100	0.9596
5	-0.0066	0.9663

L approximation has been used. The corresponding streamfunction, velocity, and vorticity associated with least kinetic energy solutions are posted in Table 4.3. The streamlines are shown in Figure 4.2a using solid lines to denote the traditional Taylor–Culick's, the minimum energy solution is shown using broken lines.

4.2 Generalization

4.2.1 Type I solutions with increasing energy levels

So far, we have identified the form of α_n that produces the solution with the minimum kinetic energy. In the quest for solutions that assimilate varying energy levels, a general formulation for the sidewall injection sequence is at hand. For mathematical simplicity, we restrict our analysis to long chambers (i.e. $L \geq L_{\text{cr}}$) and use (4.18) as our starting point. One can then rewrite α_n in a parametric form as

$$\alpha_n = \frac{8(-1)^n}{\pi^2(2n+1)^2} \sim \frac{(-1)^n A_2}{(2n+1)^2} \tag{4.21}$$

The constant $A_2 = 8/\pi^2$ can be determined by making (4.21) congruent with the sidewall injection constraint (4.7). We also note that the subscript of A_2 is tightly connected to the exponent that stands out in the denominator. Following rote, one may propose the generic Type I form

$$\alpha_n^-(q) = \frac{(-1)^n A_q}{(2n+1)^q}; \quad q \geq 2 \tag{4.22}$$

where the exponent q is conveniently dubbed the *kinetic energy power index* due to its intricate connection with the kinetic energy density as will be shown shortly. The constant A_q can be used to make (4.22) consistent with the boundary condition (4.7). This operation yields

$$\sum_{n=0}^{\infty} (-1)^n \frac{(-1)^n A_q}{(2n+1)^q} = 1 \tag{4.23}$$

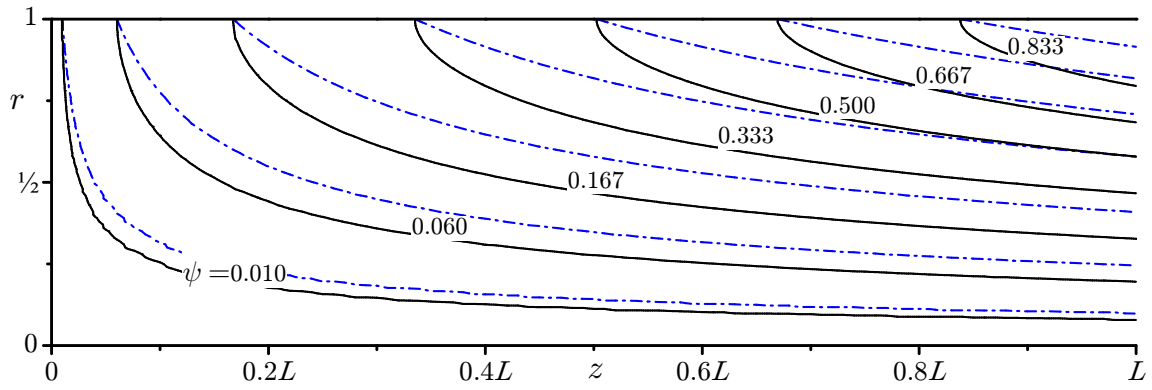

(a) Overall streamline pattern

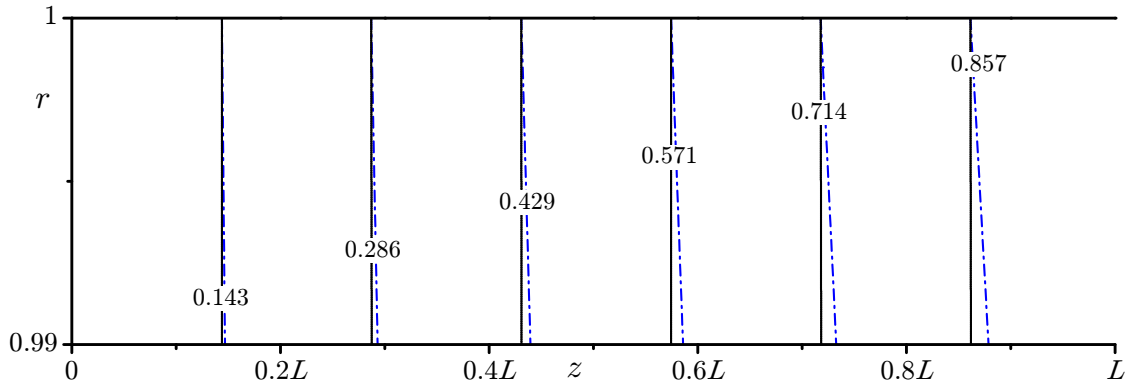

(b) Showing no-slip boundary condition

Figure 4.2: Streamlines corresponding to the minimum kinetic energy solution (4.20) for an inert headwall.

Table 4.3: Summary of least kinetic energy solutions.

$w(r,0)$	$\psi^-(r,z)$	$w^-(r,z)$
0	$\psi^-_{\text{ref}} \equiv \dfrac{8}{\pi^2} z \displaystyle\sum_{n=0}^{\infty} \dfrac{(-1)^n}{(2n+1)^2} \sin\chi_n \mapsto r^2 z$	$w^-_{\text{ref}} \equiv \dfrac{8}{\pi} z \displaystyle\sum_{n=0}^{\infty} \dfrac{(-1)^n}{(2n+1)} \cos\chi_n \mapsto 2z$
W_{c}	$\psi^-_{\text{ref}} + \dfrac{4W_{\text{c}}}{\pi^2} \displaystyle\sum_{n=0}^{\infty} \dfrac{(-1)^n}{(2n+1)^2} \sin\chi_n$	$w^-_{\text{ref}} + \dfrac{4W_{\text{c}}}{\pi} \displaystyle\sum_{n=0}^{\infty} \dfrac{(-1)^n}{(2n+1)} \cos\chi_n$
$W_{\text{c}} \cos(\frac{1}{2}\pi r^2)$	$\psi^-_{\text{ref}} + \dfrac{W_{\text{c}}}{\pi} \sin(\frac{1}{2}\pi r^2)$	$w^-_{\text{ref}} + W_{\text{c}} \cos(\frac{1}{2}\pi r^2)$
$W_{\text{c}}(1-r^2)$	$\psi^-_{\text{ref}} + \dfrac{8W_{\text{c}}}{\pi^3} \displaystyle\sum_{n=0}^{\infty} \dfrac{\sin\chi_n}{(2n+1)^3}$	$w^-_{\text{ref}} + \dfrac{8W_{\text{c}}}{\pi^2} \displaystyle\sum_{n=0}^{\infty} \dfrac{\cos\chi_n}{(2n+1)^2}$

or

$$A_q = \frac{1}{\sum_{n=0}^{\infty}(2n+1)^{-q}} = \frac{1}{\zeta(q)(1-2^{-q})}; \quad \zeta(q) = \sum_{k=1}^{\infty} k^{-q} \tag{4.24}$$

where $\zeta(s)$ is Riemann's zeta function. Evidently, the case corresponding to $q = 2$ reproduces the state of least kinetic energy. Also note that the $q \geq 2$ condition is needed to ensure series convergence down to the vorticity as will be shown in §4.2.5. Backward substitution enables us to collect the final form of α_n, namely,

$$\alpha_n^-(q) = \frac{(-1)^n(2n+1)^{-q}}{\sum_{k=0}^{\infty}(2k+1)^{-q}} = \frac{(-1)^n(2n+1)^{-q}}{\zeta(q)(1-2^{-q})}; \quad q \geq 2 \quad \text{(Type I)} \tag{4.25}$$

To understand the effect of the energy power index q on the kinetic energy density, we use (4.25) and (4.6) to plot $\mathscr{E}$ versus q at two aspect ratios. This plot corresponds to the lower branch of Figure 4.3 for both $L = 10$ and $L = 20$. Interestingly, as $q \to \infty$, Taylor–Culick's classic solution is recovered. In fact, using (4.25), it can be

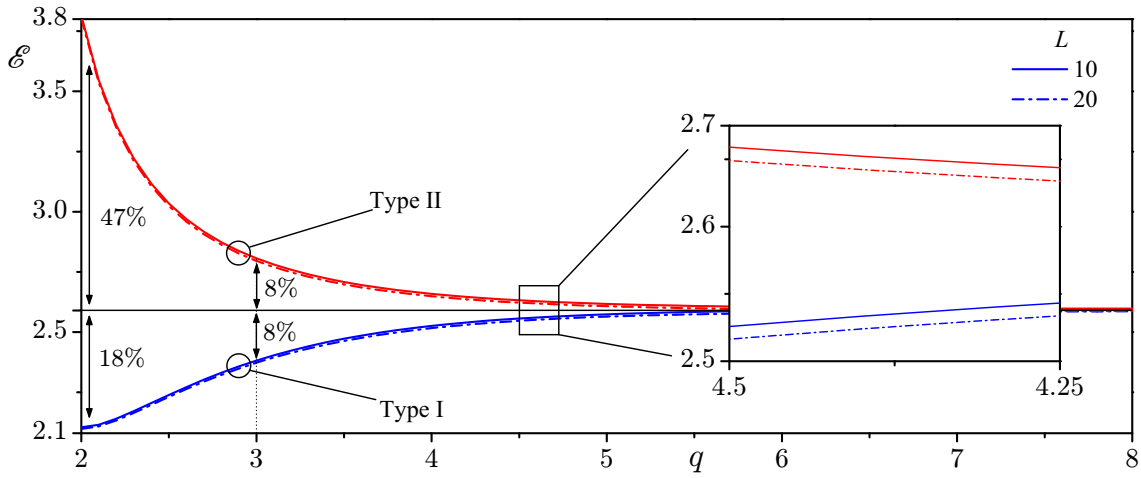

Figure 4.3: Variation of the kinetic energy density with the energy power index for Type I (lower branch) and Type II (upper branch) solutions. These are shown at two aspect ratios, $L = 10$ (—) and $L = 20$ (– · –).

rigorously demonstrated that

$$\lim_{q\to\infty} \alpha_n^-(q) = \begin{cases} 1; & n = 0 \\ 0; & \text{otherwise} \end{cases} \tag{4.26}$$

This result reproduces Taylor–Culick's classic model. All of the Type I solutions derived from (4.25) possess kinetic energies that are lower than Taylor–Culick's; this explains the negative sign in the superscript of α_n^-. They can be bracketed between (4.20) and $\psi(r,z) = z\sin(\frac{1}{2}\pi r^2)$. In practice, profiles with $q \geq 5$ will be practically indistinguishable from Taylor–Culick's as their energies will then differ by less than one percent. The distinct solutions correspond to $q = 2$, 3, and 4 with energies that are 81.1, 91.7, and 97.3 percent of Taylor–Culick's, respectively.

4.2.2 Type II solutions with decreasing energy levels

One may argue that, if one is able to find solutions that possess less kinetic energies than Taylor–Culick's, then there should exist, at least mathematically, a complementary family of solutions with energies that exceed Taylor–Culick's. To test this hypothesis, we begin by introducing

$$\alpha_n^+(q) = \frac{B_q}{(2n+1)^q}; \quad q \geq 2 \tag{4.27}$$

The key difference here stands in the exclusion of the $(-1)^n$ multiplier that appears in (4.22). Substitution into (4.7) requires that

$$\sum_{n=0}^{\infty} \frac{(-1)^n B_q}{(2n+1)^q} = 1 \tag{4.28}$$

or

$$B_q = \frac{1}{\sum_{n=0}^{\infty}(-1)^n(2n+1)^{-q}} = \frac{4^q}{\zeta(q,\frac{1}{4}) - \zeta(q,\frac{3}{4})}; \tag{4.29}$$

where $\zeta(q,a)$ is the generalized Riemann zeta function given here as

$$\zeta(q,a) = \sum_{k=0}^{\infty}(k+a)^{-q} \quad \forall\, a \in \mathbb{R} \tag{4.30}$$

Equation (4.27) yields the general structure for the Type II complementary family of solutions

$$\alpha_n^+(q) = \frac{(2n+1)^{-q}}{\sum_{k=0}^{\infty}(-1)^k(2k+1)^{-q}} = \frac{4^q(2n+1)^{-q}}{\zeta(q,\frac{1}{4}) - \zeta(q,\frac{3}{4})}; \quad q \geq 2 \quad \text{(Type II)} \tag{4.31}$$

The form given by (4.31) will yield solutions that entertain higher kinetic energies than Taylor–Culick's, hence the superscript in α_n^+. The energy variation that accompanies the Type II solutions is shown in the upper branch of Figure 4.3. Similar to the Type I family, Taylor–Culick's model is recovered here asymptotically by taking the limit of α_n^+ as $q \to \infty$. Most of the Type II solutions exhibit energies that fall within one percent of Taylor–Culick's. The most interesting are those corresponding to $q = 2$, 3, and 4 with energies that are 47.0, 8.08, and 2.4 percent larger than Taylor–Culick's. When the energy level is fixed at $q = 2$, a simplification follows for the Type II

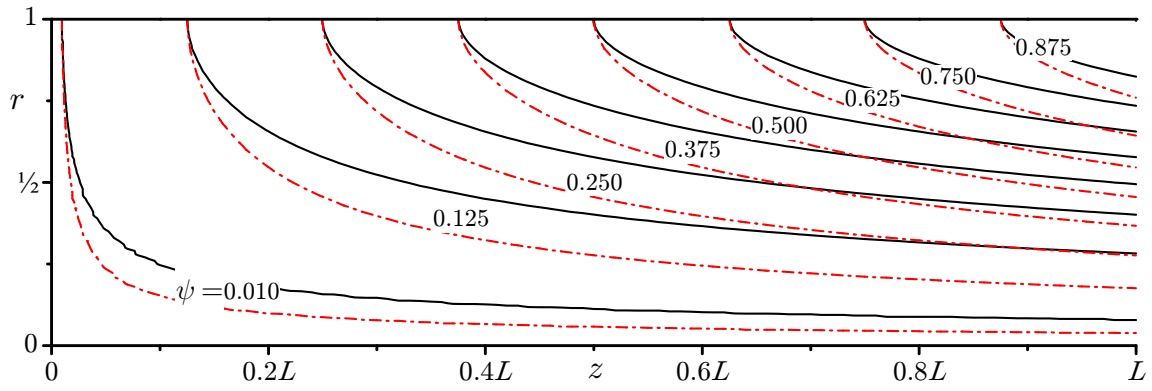

Figure 4.4: Comparison of the Taylor–Culick streamlines (—) and the Type II energy-maximized solution ($q = 2$) with stretched streamline curvature ($- \cdot -$). Results are shown for an inert headwall.

Table 4.4: Summary of solutions with most kinetic energy for various headwall injection patterns. Here, $\chi_n \equiv \frac{1}{2}(2n+1)\pi r^2$.

$w(r,0)$	$\psi^+(r,z)$	$w^+(r,z)$
0	$\psi^+_{\text{ref}} \equiv \dfrac{z}{\mathscr{C}}\displaystyle\sum_{n=0}^{\infty}\dfrac{\sin\chi_n}{(2n+1)^2}$	$w^+_{\text{ref}} \equiv \dfrac{\pi}{\mathscr{C}}z\displaystyle\sum_{n=0}^{\infty}\dfrac{\cos\chi_n}{(2n+1)}$
W_{c}	$\psi^+_{\text{ref}} + \dfrac{4W_{\text{c}}}{\pi^2}\displaystyle\sum_{n=0}^{\infty}\dfrac{(-1)^n}{(2n+1)^2}\sin\chi_n$	$w^+_{\text{ref}} + \dfrac{4W_{\text{c}}}{\pi}\displaystyle\sum_{n=0}^{\infty}\dfrac{(-1)^n}{(2n+1)}\cos\chi_n$
$W_{\text{c}}\cos(\frac{1}{2}\pi r^2)$	$\psi^+_{\text{ref}} + \dfrac{W_{\text{c}}}{\pi}\sin(\frac{1}{2}\pi r^2)$	$w^+_{\text{ref}} + W_{\text{c}}\cos(\frac{1}{2}\pi r^2)$
$W_{\text{c}}(1-r^2)$	$\psi^+_{\text{ref}} + \dfrac{8W_{\text{c}}}{\pi^3}\displaystyle\sum_{n=0}^{\infty}\dfrac{\sin\chi_n}{(2n+1)^3}$	$w^+_{\text{ref}} + \dfrac{8W_{\text{c}}}{\pi^2}\displaystyle\sum_{n=0}^{\infty}\dfrac{\cos\chi_n}{(2n+1)^2}$

representation. Catalan's constant emerges in (4.31), namely, in the form

$$\mathscr{C} = \sum_{k=0}^{\infty}(-1)^k(2k+1)^{-2} \simeq 0.915966 \tag{4.32}$$

The Type II solution that carries the most energy at $q = 2$ is plotted in Figure 4.4 and listed in Table 4.4.

Now that we have derived two families of solutions with kinetic energies that either surpass or lag that of Taylor–Culick's, the latter may be perceived as a saddle point for both solutions. In fact, in §4.6, we will demonstrate that the Taylor–Culick model corresponds to a local equilibrium solution to which all other profiles will quickly converge.

4.2.3 Behavior of the velocity and vorticity fields

The ramifications of the energy power index q on the solution are illustrated in Figure 4.5 where both velocity components are drawn along with the streamline turn angle θ.

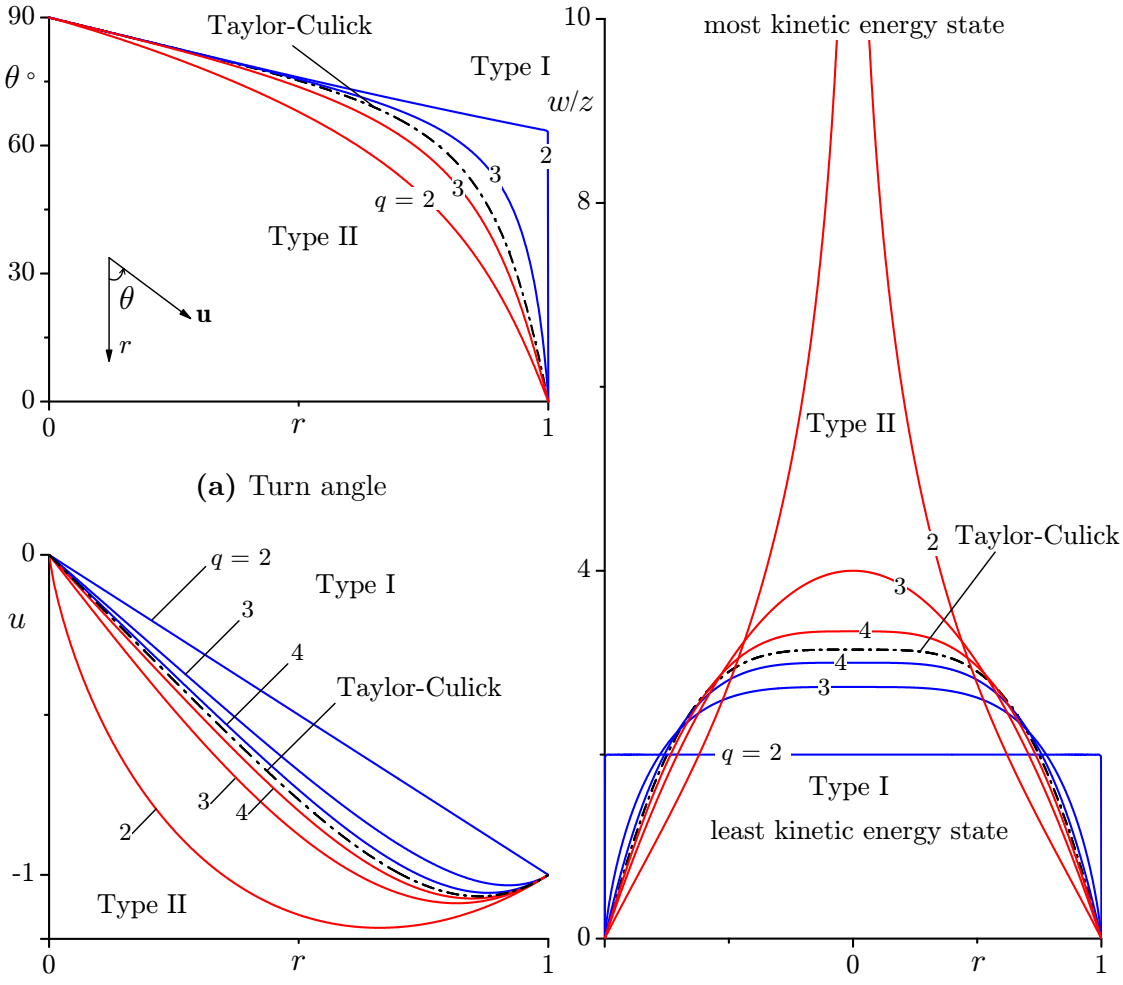

Figure 4.5: Comparison between analytical (lines) and numerical simulations (circles) for the vorticity magnitude using (a, b) cosine and (c, d) Poiseuille injection. Curves are shown for $z/L = 0.1$, 0.3, 0.5, 0.7, and 0.9.

Turn angle

The turn angle represents the slope of the local velocity measured from the radial injection direction. It may be expressed via

$$\theta(r) = \frac{180}{\pi} \tan^{-1}\left(-\frac{1}{z}\frac{w}{u}\right) \tag{4.33}$$

This angle is shown Figure 4.5a where it is clear that, irrespective of q, the flow is purely radial at the sidewall where $\theta(1) = 0$. This reaffirms that our model conforms to the no-slip boundary condition at the sidewall. Furthermore, the no cross flow boundary condition at $r = 0$ is clearly evident for all cases and is reflected in $\theta(0) = 90$. The Type I solutions are accompanied by the sharpest turns that become successively smoother as q is increased. This may be explained by the relative magnitudes of the radial and axial velocities. Specifically, for the Type I, $q = 2$ case, the axial velocity remains practically constant throughout any cross section of the chamber, while the radial velocity magnitude increases radially. As we cross into the Type II region, the flow starts turning in the vicinity of the sidewall and progresses smoothly as the centerline is approached. This can be corroborated by the impressive increase in the axial velocity magnitude thus forcing the flow to turn further away from the centerline.

Radial velocity

The radial velocity is shown in Figure 4.5b for both families of solutions and representative energy power indices. Starting with the Type I region, the radial velocity is seen to increase in magnitude with successive increases in q. Interestingly, for the case with least kinetic energy, the radial velocity diminishes linearly from 0 to -1 as we move from the sidewall towards the centerline region. Conversely, the Type II solutions exhibit smoother curvatures with successive decreases in magnitude as q is increased. Also, the solution accompanied by the most kinetic energy is seen to overshoot the sidewall injection speed by 16.5% at $r \approx 0.66$, a value that is twice as

large as that of Taylor–Culick's. Note that the Taylor–Culick radial velocity exhibits a 7% overshoot at $r = 0.861$. Of note also is the radial location of the overshoot that varies between $0.66 < r < 1$ as one moves from the Type II, $q = 2$ to the Type I, $q = 2$ solution.

Axial velocity

In Figure 4.5c, it is clear that the Type I axial velocities are initially blunt, with the flattest curve being the one corresponding to $q = 2$. As q is increased, all curves evolve into a sinusoid that approaches the Taylor–Culick model for $q = 5$ and above. Furthermore, as we cross into the Type II region, the centerline velocity continues to increase with the energy content. Due to mass conservation, $Q = 2\pi \int_0^1 wr \, \mathrm{d}r = 2\pi z$, and so the centerline speed at each power index is compelled to vary with its corresponding shape to preserve Q. The lowest centerline speed will thus accompany the spatially uniform distribution whereas the highest speed will emerge in the narrowest and most elongated profile connected with the state of most kinetic energy. Interestingly, although this profile slowly diverges at the centerline, it observes mass conservation. This may be explained by the fact that $\lim_{r \to 0} rw^+(r, z) = 0$.

Table 4.5: Vorticity for least or most kinetic energy solutions.

$w(r, 0)$	$\Omega^-(r, z)$	$\Omega^+(r, z)$
0	0	$\Omega^+_{\mathrm{ref}} \equiv \dfrac{\pi^2}{2\mathscr{C}} rz \csc(\frac{1}{2}\pi r^2)$
W_{c}	0	Ω^+_{ref}
$W_{\mathrm{c}} \cos(\frac{1}{2}\pi r^2)$	$\pi W_{\mathrm{c}} r \sin(\frac{1}{2}\pi r^2)$	$\Omega^+_{\mathrm{ref}} + \pi W_{\mathrm{c}} r \sin(\frac{1}{2}\pi r^2)$
$W_{\mathrm{c}}(1 - r^2)$	$2W_{\mathrm{c}} r$	$\Omega^+_{\mathrm{ref}} + 2W_{\mathrm{c}} r$

Vorticity

Having fully determined the velocity field, its vorticity companion may be determined from

$$\Omega = \Omega_\theta = \pi^2 r \sum_{n=0}^{\infty} (2n+1)^2 \alpha_n z \sin \chi_n \tag{4.34}$$

This expression is evaluated for the least and most kinetic energy forms ($q = 2$) and provided in Table 4.5.

Irrotational motion

For the least kinetic energy solution (Type I, $q = 2$), the linear variation that accompanies the radial velocity as well as the uniformity of the axial velocity point out in the direction of an irrotational motion. In fact, the vorticity in this case is zero and the corresponding velocity field collapses into

$$\mathbf{u} = -r\mathbf{e}_r + 2z\mathbf{e}_z \tag{4.35}$$

inside the domain. This is the classic velocity potential for the Taylor–Culick problem and has been traditionally used in modeling the internal flow in SRMs (McClure et al. 1963). In Chapter 5, this result will be further corroborated with a variant of Kelvin's minimum energy theorem, thus enforcing the validity of the present model.

4.2.4 Pressure evaluation

One can approximate the pressure over the entire solution domain by using (2.75)

$$p(r, z) = \sum_{n=0}^{\infty} p_n(r, z) \tag{4.36}$$

By substituting u_n and w_n from (4.3) into (2.4b), one can integrate for the pressure eigenmodes to recover

$$p_n = p_0 - \tfrac{1}{2}(2n+1)^2\pi^2 z^2 \alpha_n^2 - \tfrac{1}{2}\frac{\alpha_n^2}{r^2}\sin^2\chi_n \tag{4.37}$$

The total pressure is then obtained by summing over all eigensolutions

$$p(r,z) = p_0 - \tfrac{1}{2}\pi^2 z^2 \sum_{n=0}^{\infty}(2n+1)^2\alpha_n^2 - \tfrac{1}{2}\sum_{n=0}^{\infty}\frac{\alpha_n^2}{r^2}\sin^2\chi_n \tag{4.38}$$

where $p_0 = p(0,0)$. Using (4.38), the centerline pressure drop is found to be

$$\Delta p = p(0,z) - p_0 = -\tfrac{1}{2}\pi^2 z^2 \sum_{n=0}^{\infty}(2n+1)^2\alpha_n^2 \tag{4.39}$$

Equation (4.39) is plotted in Figure 4.6 for $q = 2$, 3, and ∞ for both types of solutions. It is clear that the largest pressure drop corresponds to the Type II energy state with

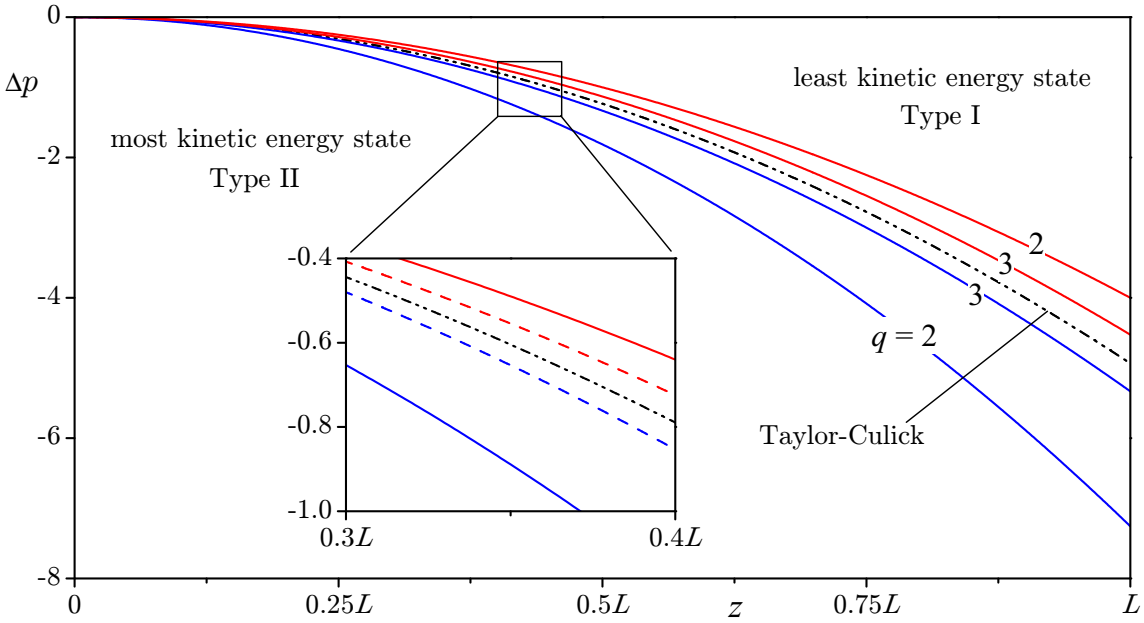

Figure 4.6: Centerline pressure drop for Type I and Type II energy states.

the most kinetic energy while the smallest drop accompanies the Type I solution with the least kinetic energy, i.e. the irrotational motion.

4.2.5 Asymptotic limits of the kinetic energy density

When the large L approximation is employed, with $q = 2$, the Type II kinetic energy density $\mathscr{E}^+$ approaches a constant value of $\mathscr{E}^+_\infty(2) = \pi^5/(96\mathscr{C}^2) \approx 3.79944$. Note that the asymptotic value for Taylor–Culick's (i.e. when both L and q approach infinity), $\mathscr{E}^\infty_\infty \equiv \pi^3/12 \approx 2.5838$, is recovered as $q \to \infty$. In general, when $L \to \infty$, the limit of the kinetic energy density can be written as

$$\mathscr{E}_\infty = \tfrac{1}{12}\pi^3 \sum_{n=0}^{\infty} (2n+1)^2 \alpha_n^2 = \mathscr{E}^\infty_\infty \sum_{n=0}^{\infty} (2n+1)^2 \alpha_n^2 \tag{4.40}$$

For the Type I solutions, substitution of (4.40) yields a closed-form expression,

$$\mathscr{E}^-_\infty(q) = \mathscr{E}^\infty_\infty \left[\sum_{k=0}^{\infty} \frac{1}{(2k+1)^q}\right]^{-2} \sum_{n=0}^{\infty} (2n+1)^{2-2q} = \mathscr{E}^\infty_\infty \frac{4^q - 4}{(2^q-1)^2} \frac{\zeta(2q-2)}{\zeta(q)^2} \tag{4.41}$$

In like manner, for the Type II solutions, (4.40) leads to

$$\mathscr{E}^+_\infty(q) = \mathscr{E}^\infty_\infty \left[\sum_{k=0}^{\infty} \frac{(-1)^k}{(2k+1)^q}\right]^{-2} \sum_{n=0}^{\infty} (2n+1)^{2-2q} = \mathscr{E}^\infty_\infty \frac{4^q(4^q-4)\zeta(2q-2)}{[\zeta(q,\frac{1}{4}) - \zeta(q,\frac{3}{4})]^2} \tag{4.42}$$

Specific values of these limits can be found in Table 4.6. Both types approach $\mathscr{E}^\infty_\infty$ either from below or above. One may consult Figure 4.7 to infer the asymptotic kinetic energy density associated with different values of q. Note that the Taylor–Culick limit of 2.5838 is practically reached by both Type I and Type II solutions with differences of less than 0.287 and 0.265 percent at $q = 6$. The maximum range occurs at $q = 2$ while the total allowable excursion in energy that the mean flow can undergo may be estimated at $[\mathscr{E}^+_\infty(2) - \mathscr{E}^-_\infty(2)]\,/\mathscr{E}^\infty_\infty = 0.66$. From an academic standpoint, the Type I family of solutions bridges the gap between an essentially potential flow at

$q = 2$ and a fully rotational field at $q \to \infty$, thus yielding intermediate formulations with energies that vary across the range $[0.81 - 1]\mathscr{E}_\infty^\infty$.

4.3 Convergence properties

Using the absolute convergence and ratio tests, the series representations can be individually shown to be unconditionally convergent for $q \geq 2$. The most subtle solutions to examine correspond to the Type II inert headwall case with maximum kinetic energy. The corresponding velocity and vorticity forms require special attention. For the sake of illustration, we consider the Type II streamfunction, specifically

$$\psi(r,z) = z \sum_{n=0}^{\infty} \frac{B_q}{(2n+1)^q} \sin \chi_n; \quad \chi_n \equiv \tfrac{1}{2}(2n+1)\pi r^2 \tag{4.43}$$

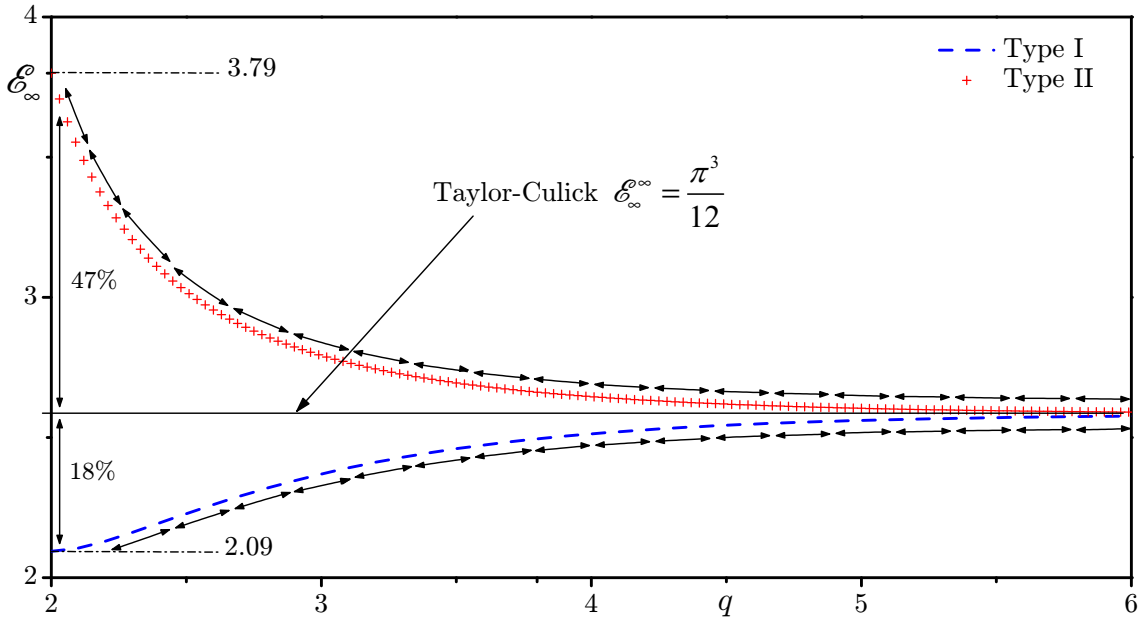

Figure 4.7: Asymptotic behavior of the kinetic energy density for both Type I (- - -) and Type II (+ + +) solutions.

The absolute convergence test may be applied to show that

$$\sum_{n=0}^{\infty}\left|\frac{1}{(2n+1)^q}\sin\chi_n\right| \leq \sum_{n=0}^{\infty}\frac{1}{(2n+1)^q} \tag{4.44}$$

where the right-hand-side converges for $q > 1$. In evaluating quantities that require one or more differentiations (such as the vorticity), we find it useful to substitute, whenever possible, the closed-form analytical representations of the series in question. The equivalent finite expressions enable us to overcome the pitfalls of term-by-term differentiation which, for some infinite series, can lead to spurious results. The Type II axial velocity for the inert headwall configuration presents such an example at $q = 2$. This series can be collapsed into a combination of inverse hyperbolic tangent functions by writing

$$u_z^+ = \sum_{n=0}^{\infty}\frac{B_2}{(2n+1)}\cos\chi_n = \frac{1}{2\mathscr{C}}\left[\tanh^{-1}\left(e^{i\frac{1}{2}\pi r^2}\right) + \tanh^{-1}\left(e^{-i\frac{1}{2}\pi r^2}\right)\right] \tag{4.45}$$

While term-by-term differentiation of the infinite series representation of u_z^+ diverges, the derivative of the closed-form equivalent yields the correct outcome of

$$\Omega^+ = -\frac{\pi}{2\mathscr{C}} r\csc(\tfrac{1}{2}\pi r^2) \tag{4.46}$$

As it may be expected, the corresponding solution is accompanied by finite kinetic energy and mass flowrate despite its singularity at the centerline.

Table 4.6: Sample values of the asymptotic energy density.

q	$\mathscr{E}_\infty^-$	$\mathscr{E}_\infty^+$
2	2.0944	3.7994
4	2.5133	2.6457
6	2.5764	2.5907

4.4 Arbitrary injection

For T-burners, solid rocket motors with reactive fore-ends, and hybrid rocket chambers with injector faceplates, a model that accounts for headwall injection is required. For these problems, our analysis may be repeated assuming an injecting headwall with an axisymmetrically varying profile defined by (2.9). The streamfunction is given by

$$\psi(r,z)=\sum_{n=0}^{\infty}(\alpha_n z+\beta_n)\sin[\tfrac{1}{2}(2n+1)\pi r^2] \tag{4.47}$$

In the resulting expressions, β_n does not vanish. As shown by Majdalani and Saad (2007) and in Chapter 2, orthogonality may be applied to obtain β_n for an axisymmetric headwall injection profile. Application of Lagrangian optimization in conjunction with the large L approximation yield identical results for α_n as those obtained in (4.25) and (4.31). The streamfunction, axial velocity, and vorticity for several injection profiles are catalogued in tables 4.3, 4.4, and 4.5 where the least and most kinetic energy solutions are identified.

4.5 Numerical verification

As a way of validating our solutions, (2.17) is solved numerically using a fourth order Runge–Kutta method. By introducing the transformation $\psi=zF(r)$, (2.17) is reduced to a second order ODE

$$F''(r)-\frac{1}{r}F'(r)+C^2r^2F(r)=0 \tag{4.48}$$

In order to numerically capture the different variational solutions, the boundary conditions of (2.18) have to be carefully selected. Since our solutions are in series

form, we first decompose $F(r)$ into its eigenmode components

$$F(r) = \sum_{n=0}^{\infty} F_n(r) \tag{4.49}$$

then, (4.48) becomes

$$F_n''(r) - \frac{1}{r}F_n'(r) + C_n^2 r^2 F_n(r) = 0; \quad n = 0, 1, \cdots, \infty \tag{4.50}$$

where n corresponds to the eigenmode associated with $C_n = (2n+1)\pi$. Finally, the boundary conditions are at hand. These become

$$\begin{cases} F_n(0) = 0; & F(0) = \sum\limits_{n=0}^{\infty} F_n(0) = 0 \\ F_n(1) = (-1)^n \alpha_n; & F(1) = \sum\limits_{n=0}^{\infty} F_n(1) = \sum\limits_{n=0}^{\infty} (-1)^n \alpha_n = 1 \end{cases} \tag{4.51}$$

Using 120 terms to reconstruct the series expansions, both numerical and analytical solutions for $F(r)$ and $F'(r)$ are displayed in Figures 4.8a and 4.8b, respectively. It is apparent from these figures that, irrespective of the power index, the variational solutions are reliably simulated by the numerical data to the extent that visual differences between full circles (numerical) and solid lines (analytical) are masked.

4.6 Thermodynamic considerations

To help address the question of the physicality of our variational solutions, a second law analysis is required. Given that our formulation is volumetric, we choose a control volume approach and start by noting that, for a frictionless fluid, the entropy s remains invariant along individual streamlines. This can be expressed as

$$s = \sum_{n=0}^{\infty} s_n = \text{const} \quad \text{(along a streamline)} \tag{4.52}$$

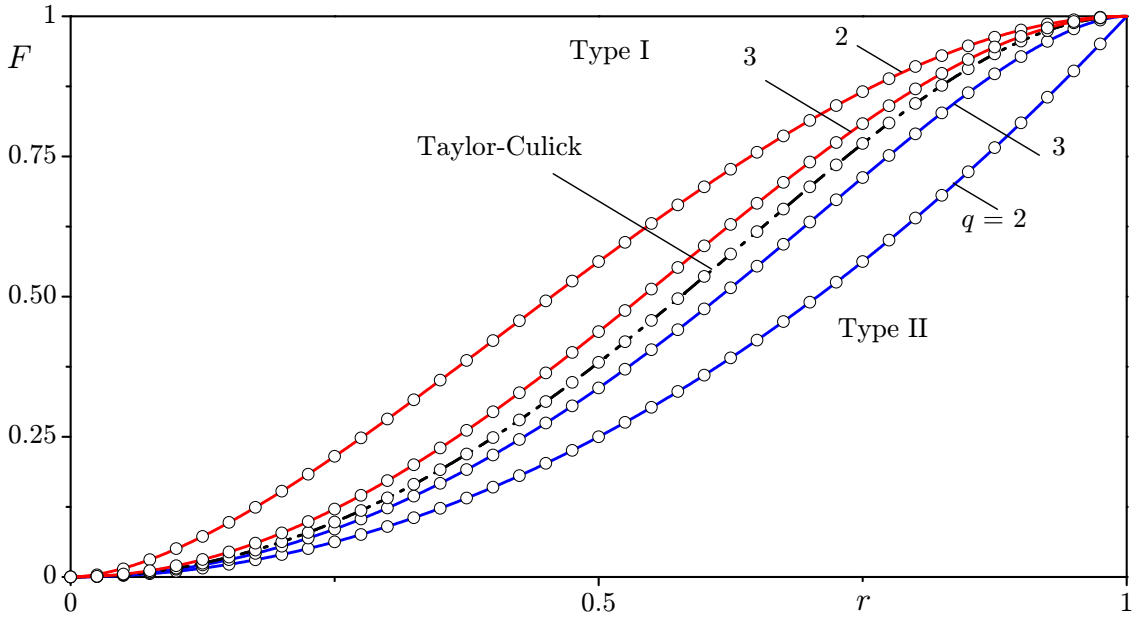

(a) $F(r)$

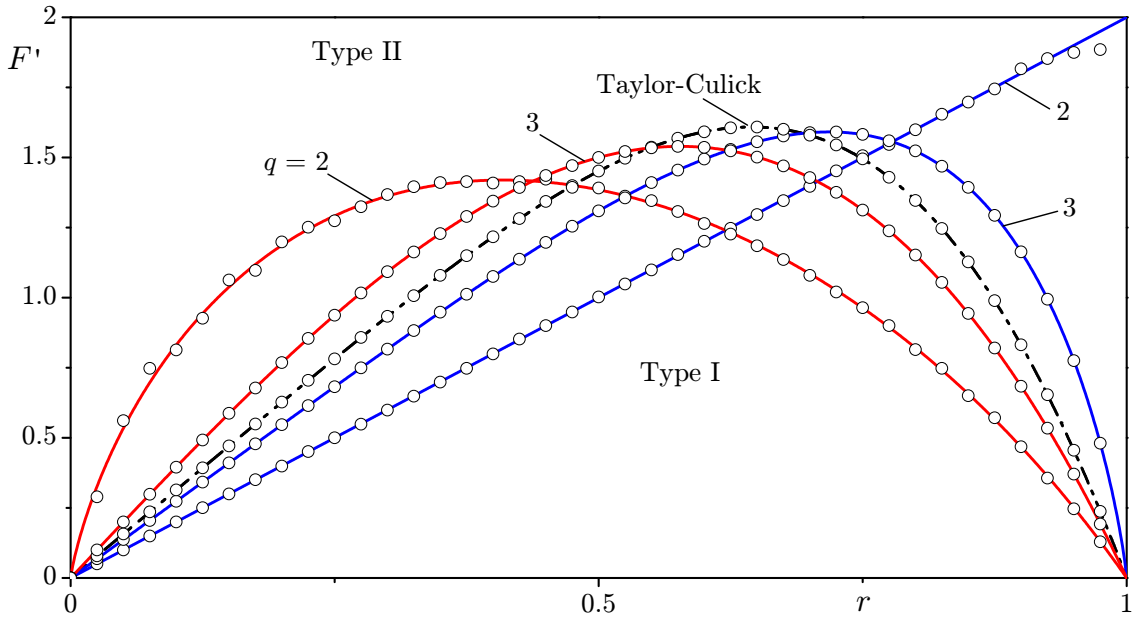

(b) $F'(r)$

Figure 4.8: Comparison between analytical (—) and numerical (∘) solutions for (a) $F(r)$, and (b) $F'(r)$ for Type I (blue) and Type II (red) solutions. Plots are shown for $q = 2, 3$ and ∞. Here, $\psi(r, z) = zF(r)$.

where s is the total local entropy while s_n corresponds to the entropy carried by the individual modes of the series solutions. A viable model for entropy input in our case is to assume that it is proportional to the vorticity. In other words, since $\Omega = C^2 r\psi$ one can choose the entropy to be proportional to the streamfunction. Given that ψ is already at hand, one may express (4.52) in terms of the independent variables r and z. Choosing σ to denote the proportionality constant, we set

$$s(r,z) = \sigma\psi(r,z) = \sigma\sum_{n=0}^{\infty}\psi_n = \sigma\sum_{n=0}^{\infty}\alpha_n z\sin\left[\tfrac{1}{2}(2n+1)\pi r^2\right] \tag{4.53}$$

Although unnecessary for the pursuant analysis, one may determine σ from knowledge of the entropy of the incoming stream. By using the same average entropy S_w at the injecting sidewall as a common basis for all variational solutions (i.e. $S_\mathrm{w} \neq S_\mathrm{w}(q)$), we integrate (4.53) at the porous wall and set

$$S_\mathrm{w} = \frac{2\pi\displaystyle\int_0^L s(1,z)\,\mathrm{d}z}{2\pi L} = \frac{\sigma L}{2}\sum_{n=0}^{\infty}(-1)^n\alpha_n = \frac{\sigma L}{2} \quad \text{or} \quad \sigma = 2\frac{S_\mathrm{w}}{L} \tag{4.54}$$

The proportionality constant is thus determined as function of the average entropy at the wall.

4.6.1 Entropy change for a given energy state

For a given energy state q, we consider the control volume $\mathcal{V}$ bounded by the inner surface of the porous cylinder shown in Figure 4.9. In the absence of heat transfer or mechanical work that is congruent with our steady state model, the change of entropy

as the fluid crosses $\mathcal{V}$ may be determined from the net entropy flux

$$\begin{aligned}\Delta\dot{S} = \dot{S}_{\text{out}} - \dot{S}_{\text{in}} &= \iint_{\partial\mathcal{V}} s\,\mathbf{u}\cdot\mathbf{n}\,\mathrm{d}\mathcal{S} \\ &= 2\pi\int_0^1 s(r,L)w(r,L)r\,\mathrm{d}r + 2\pi\int_0^L s(1,z)u(1,z)\,\mathrm{d}z \\ &= 2\pi\int_0^1 s(r,L)w(r,L)r\,\mathrm{d}r - 2\pi\int_0^L s(1,z)\,\mathrm{d}z = 0; \quad \text{(Type I, II)}\end{aligned} \tag{4.55}$$

This result confirms that the inviscid flow corresponding to a fixed state of energy undergoes a reversible process. Note that, when evaluating (4.55), the product of the sums is employed via

$$\begin{cases} s(r,z)w(r,z) = \displaystyle\sum_{n=0}^{\infty} s_n(r,z)\sum_{n=0}^{\infty} w_n(r,z) \\ s(r,z)u(r,z) = \displaystyle\sum_{n=0}^{\infty} s_n(r,z)\sum_{n=0}^{\infty} u_n(r,z) \end{cases} \tag{4.56}$$

In lieu of coupling the total eigensolutions, one may pair the individual eigenmodes of the entropy and velocity viz.

$$\begin{cases} s(r,z)w(r,z) = \displaystyle\sum_{n=0}^{\infty} s_n(r,z)w_n(r,z) \\ s(r,z)u(r,z) = \displaystyle\sum_{n=0}^{\infty} s_n(r,z)u_n(r,z) \end{cases} \tag{4.57}$$

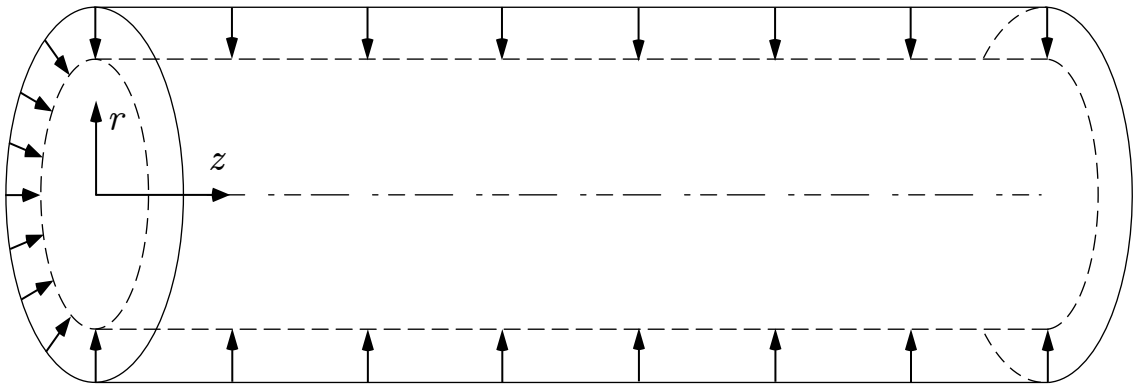

Figure 4.9: Control volume.

Interestingly, evaluating the new difference between incoming and outgoing entropy fluxes leads to

$$\begin{aligned}\Delta\dot{S} = \dot{S}_{\text{out}} - \dot{S}_{\text{in}} =& 2\pi \sum_{n=0}^{\infty} \int_0^1 s_n(r, L) w_n(r, L) r \, \mathrm{d}r \\ &+ 2\pi \sum_{n=0}^{\infty} \int_0^L s_n(1, z) u_n(1, z) \, \mathrm{d}z = 0; \quad \text{(Type I, II)} \end{aligned} \tag{4.58}$$

The entropy flux is thus conserved across the chamber irrespective of whether the eigensolutions remain strongly coupled or not.

4.6.2 Entropy change across energy states

In order to address the nature of the mechanism responsible for the system to opt for one energy state over another, or one type of solutions over another for that matter, we invoke the principle of entropy maximization. This principle states that a system will tend to maximize entropy at equilibrium. Albeit usually applied in a setting with viscous losses, the concept may still be explored in our case. This may be accomplished by considering the different energy solutions as different states of the same system. To that end, we start by selecting the control volume shown in figure (4.9). Next, we evaluate the change in total volumetric entropy as function of the kinetic energy power index q. This can be done by integrating (4.53) over the control volume and writing

$$S(q) = \int_0^{2\pi} \int_0^L \int_0^1 sr \, \mathrm{d}r \, \mathrm{d}z \, \mathrm{d}\theta = \sigma L^2 \sum_{n=0}^{\infty} (2n+1)^{-1} \alpha_n \tag{4.59}$$

The variation of the total entropy with the energy power index is illustrated in Figure 4.10 for both types of solutions. For the Type I family, the least amount of entropy (78.5% of Taylor–Culick's) corresponds to the irrotational profile. Conversely, the most entropy (114.8% of Taylor–Culick's) marks the Type II profile exhibiting the

most kinetic energy. These observations confirm that the entropy in our problem is an increasing function of the kinetic energy.

Type I

Now for the Type I family of solutions, (4.59) reduces to

$$S^{-}(q) = \sigma L^2 \sum_{n=0}^{\infty} (2n+1)^{-1} \alpha_n^{-} = \frac{\zeta\left(1+q, \frac{1}{4}\right) - \zeta\left(1+q, \frac{3}{4}\right)}{2^{q+2}\left(-1+2^{q}\right)\zeta\left(q\right)} \sigma L^2 \tag{4.60}$$

Then, by taking the difference in total entropy between two different energy states, we recover

$$\Delta S^{-} = S^{-}(q_2) - S^{-}(q_1) > 0; \quad q_2 > q_1 \tag{4.61}$$

Accordingly, if one initializes the system with a given energy state q_1, ΔS^{-} will reach its maximum value as $q_2 \to \infty$. The maximum change in entropy will thus occur

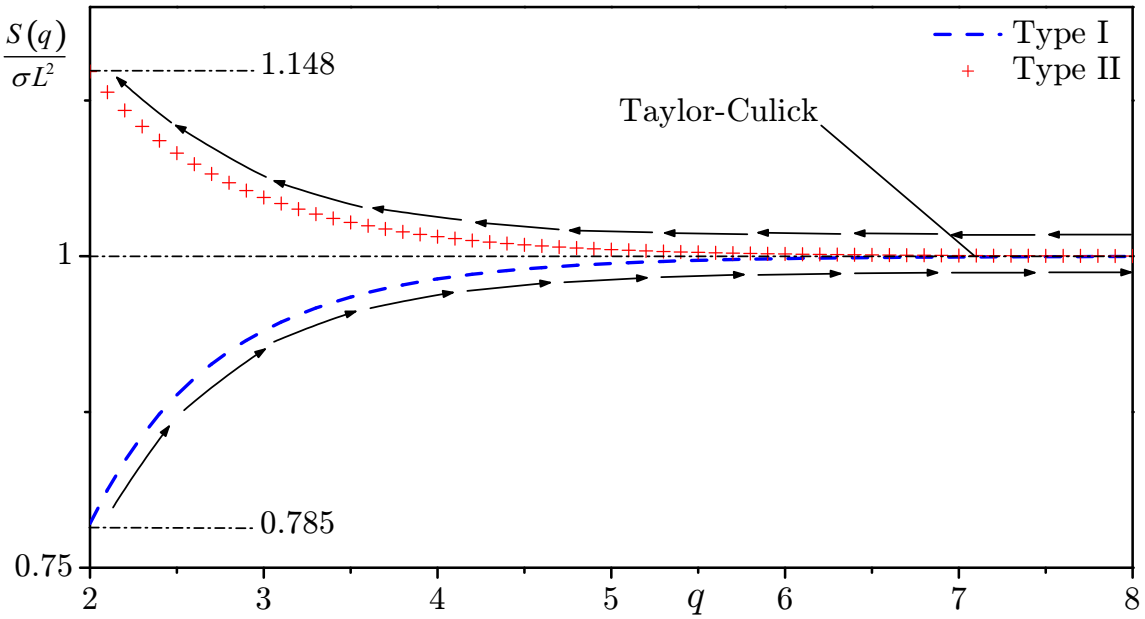

Figure 4.10: Variation of the total entropy with the energy power index q for either Type I (- - -) or Type II (+ + +) solutions. Arrows designate direction of entropy maximization.

between the irrotational and Taylor–Culick profiles for which

$$\Delta S^{-}_{\max} = S^{-}(\infty) - S^{-}(2) \cong 0.215\sigma L^2 = 0.43 S_{\mathrm{w}} L \tag{4.62}$$

Clearly, from an entropy maximization perspective, the Taylor–Culick solution constitutes the equilibrium state among all possible Type I approximations. This conclusion is reassuring since it conforms with the fact that the Taylor–Culick solution is the one obtained by solving the governing equation directly by separation of variables.

Type II

For the Type II family, one may follow similar lines and write

$$S^{+}(q) = \sigma L^2 \sum_{n=0}^{\infty} (2n+1)^{-1} \alpha_n^{+} = \frac{2^{q-1}\left(2^{q+1}-1\right)\zeta\left(q+1\right)}{\zeta\left(q,\frac{1}{4}\right) - \zeta\left(q,\frac{3}{4}\right)} \sigma L^2 \tag{4.63}$$

We also find that the change in entropy between states is

$$\Delta S^{+} = S^{+}(q_1) - S^{+}(q_2) > 0; \quad q_2 > q_1 \tag{4.64}$$

The maximum change in volumetric entropy may be estimated from

$$\Delta S^{+}_{\max} = S^{+}(2) - S^{+}(\infty) \cong 0.148\sigma L^2 = 0.296 S_{\mathrm{w}} L \tag{4.65}$$

This confirms that the $q = 2$ case entails the most entropy among the Type II solutions.

4.6.3 Physicality of the Type II family of solutions

The second law analysis shows that the volumetric entropy of the Type I family grows with successive increases in q but depreciates in the Type II case. Given an

initial profile, the system may hence evolve according to one of two scenarios that are described next.

Type I branching

If the system is initialized on the Type I branch, it will evolve, according to (4.62), to the Taylor–Culick solution so that it maximizes its total entropy. While entropy could be further increased by branching out to the Type II region, we argue that this is not possible for two reasons. Firstly, the character of the two types of solutions is acutely dissimilar owing to the incongruent formulation for α_n^- and α_n^+. Secondly, given that the Taylor–Culick solution maximizes the entropy for the Type I branch, it can be viewed as a local equilibrium state and therefore, there is no necessity for the system to switch branches once it reaches the Taylor–Culick state.

Type II branching

If the system is initialized on the Type II branch, according to (4.65), it will approach the solution with most vorticity (i.e. Type II, $q = 2$). However, we argue that, although this is a mathematically valid outcome, it may not be physically realizable since it would be practically impossible to initialize a system with such a high level of vorticity without introducing external work on the system. The most natural flow evolution corresponds to an irrotational system originally at rest in which vorticity generation is initiated at the sidewall during the injection process. The ensuing motion will subsequently progress until it reaches the stable Taylor–Culick equilibrium state in which it can settle with no further tendency to branch out.

4.7 Summary

In this chapter, we revisit the procedure leading to the Taylor–Culick incompressible model and investigate alternative models for the sidewall injection sequence α_n. By using the Lagrangian multipliers method to optimize the volumetric kinetic energy in

the chamber, a general representation of α_n is uncovered. Subsequently, two families of solutions are identified with increasing or decreasing kinetic energies of which the Taylor–Culick model is recovered as a special case. Interestingly, it is found that both types cover a wide spectrum of admissible motions ranging from purely irrotational to highly rotational fields. Finally, a second law analysis allows us to explain the physicality of these new solutions and to pinpoint the Taylor–Culick solution as an equilibrium state to which all profiles will converge.

Chapter 5

Kelvin's Minimum Energy Theorem for Compressible Flows in Open Regions

In Chapter 4, we derived two families of solutions for the Taylor–Culick problem using a variational procedure. Of the many interesting features of these motions is the fact that the one with least kinetic energy (Type I, $q = 2$) matches the irrotational solution for the Taylor–Culick problem. In principle, it should be possible to confirm this observation using Kelvin's minimum energy theorem. This theorem states that *the irrotational motion of an incompressible fluid in a simply connected region contains less kinetic energy than any other motion with the same normal velocity at its boundary.* However, the Taylor–Culick profile violates Kelvin's constraints in the exit plane at $z = L$, hence, it cannot be applied to the variational solutions unless these restraints are relaxed. In this chapter, we extend Kelvin's theorem to compressible flows in regions with different normal velocities at the boundary. This extension grants Kelvin's theorem a wider range of applications and increases our repertoire of mathematical tools for the treatment of fluid problems.

5.1 Introduction

Kelvin's contributions to fluid dynamics are fundamental to the understanding of fluid motion. His many theorems help to establish the key relations between ideal and real fluids as well as the conservation principles and behavior of vorticity and circulation in general. They continue to receive attention in various fundamental studies including those pertaining to turbulence (Chen et al. 2006; Eyink 2006) and aerodynamic lift (Wu et al. 2006). Of particular interest to this dissertation is Kelvin's minimum energy theorem. First formulated in 1849, this theorem states that *the irrotational motion* $\bar{\mathbf{u}}$ *of an incompressible fluid in a simply connected region contains less kinetic energy than any other motion* $\mathbf{u}$ *with the same normal velocity at its boundary*, $\bar{\mathbf{u}} \cdot \mathbf{n} = \mathbf{u} \cdot \mathbf{n}$ (Thomson 1849). For a fluid extending to infinity, the theorem demands a vanishing normal velocity at the far-field boundary (Lamb 1895; Batchelor 1967).

Evidently, the constraints imposed by the theorem limit its applicability to a very narrow class of problems, namely those that observe the normal velocity requirement given by $\bar{\mathbf{u}} \cdot \mathbf{n} = \mathbf{u} \cdot \mathbf{n}$. In this vein, we define a Kelvin boundary as a surface on which these constraints are observed. Conversely, a boundary on which the constraints are breached is called open. In this chapter, we demonstrate that Kelvin's theorem continues to hold in regions with open boundaries provided that an easy to check criterion is satisfied. Furthermore, we extend the applicability of the theorem to compressible flows with open boundaries.

5.2 Mathematical derivation

Theorem 5.1 (Compressible flow with open boundaries)**.** *The irrotational motion* $\bar{\mathbf{u}}$ *of a steady compressible fluid of density* $\bar{\rho}$ *in a simply connected fluid region* $\mathcal{V}$ *carries less kinetic energy than any other motion* $\mathbf{u}$ *of density* ρ *with or without the same normal velocity at its boundary provided that the following sufficient condition*

is satisfied

$$\iint_{\mathcal{S}_\mathrm{o}} \rho\phi\tilde{\mathbf{u}}\cdot\mathbf{n}\,\mathrm{d}\mathcal{S} + \tfrac{1}{2}\iiint_{\mathcal{V}} \delta_\rho\bar{\mathbf{u}}^2\,\mathrm{d}\mathcal{V} \geq \iiint_{\mathcal{V}} \phi\nabla\cdot\rho\tilde{\mathbf{u}}\,\mathrm{d}\mathcal{V} \tag{5.1}$$

where $\delta_\rho = \rho - \bar{\rho}$ defines the difference between densities corresponding to the rotational and irrotational motions, $\tilde{\mathbf{u}} = \mathbf{u} - \bar{\mathbf{u}}$ defines the vortical component of the flowfield (i.e. $\nabla\times\tilde{\mathbf{u}} = \nabla\times\mathbf{u}$), whereas ϕ, $\mathbf{n}$, and $\mathcal{S}_\mathrm{o}$ denote the velocity potential, normal unit vector, and open surface, respectively.

Proof. With $\bar{\mathbf{u}} = \nabla\phi$ being a single-valued velocity potential of a steady compressible flow in a volume of fluid $\mathcal{V}$, then $\tilde{\mathbf{u}} = \mathbf{u} - \bar{\mathbf{u}}$ refers to the rotational contribution and difference between the velocity of any other motion satisfying continuity and the potential solution $\bar{\mathbf{u}}$ (see Figure 5.1). These fields are compressible and so, by virtue of mass conservation,

$$\nabla\cdot(\bar{\rho}\bar{\mathbf{u}}) = \nabla\cdot(\rho\mathbf{u}) = 0 \tag{5.2}$$

According to Batchelor (1967), if we choose T and $\bar{T}$ to represent the kinetic energies associated with $\mathbf{u}$ and $\bar{\mathbf{u}}$, respectively, then the increment in energy brought about

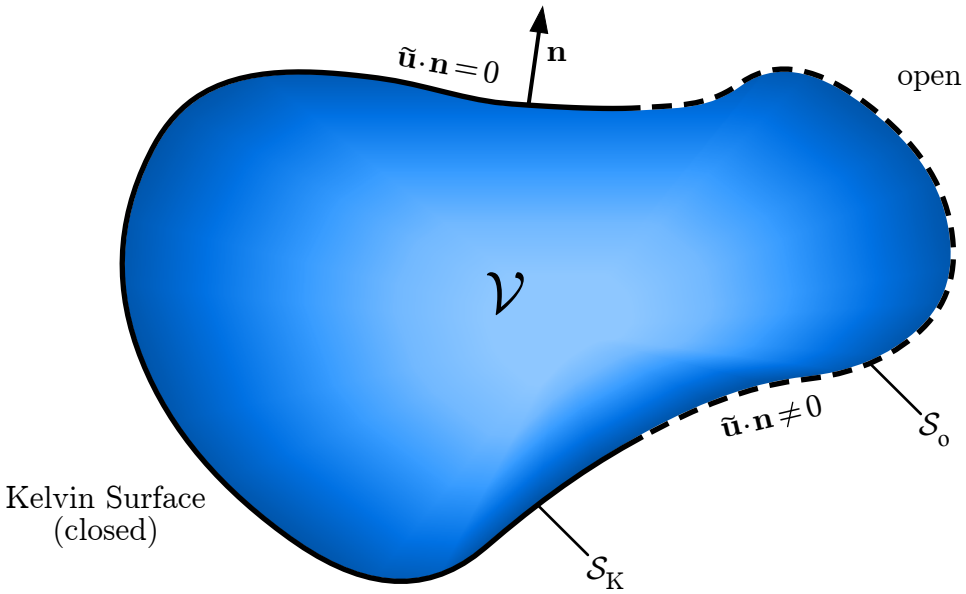

Figure 5.1: Volume of fluid showing both Kelvin and open surfaces with corresponding velocity requirements at the boundaries.

by rotationality can be evaluated from

$$\begin{aligned}\Delta T = T - \bar{T} &= \tfrac{1}{2}\iiint_{\mathcal{V}} \rho \mathbf{u}^2 \,\mathrm{d}\mathcal{V} - \tfrac{1}{2}\iiint_{\mathcal{V}} \bar{\rho}\bar{\mathbf{u}}^2 \,\mathrm{d}\mathcal{V} \\ &= \tfrac{1}{2}\iiint_{\mathcal{V}} \rho\left(\mathbf{u}^2 - \bar{\mathbf{u}}^2\right) \,\mathrm{d}\mathcal{V} + \tfrac{1}{2}\iiint_{\mathcal{V}} \delta_\rho \bar{\mathbf{u}}^2 \,\mathrm{d}\mathcal{V}\end{aligned} \tag{5.3}$$

where

$$\delta_\rho = \rho - \bar{\rho} \tag{5.4}$$

represents the net difference between the densities corresponding to the the rotational and irrotational motions. This pseudo-density function does not correspond to a physical description of some mass per unit volume because it can take on negative values in general. It simply represents a convenient connotation for simplifying algebraic manipulation. Consequently, using $\mathbf{u}^2 - \bar{\mathbf{u}}^2 = (\mathbf{u} - \bar{\mathbf{u}})^2 + 2(\mathbf{u} - \bar{\mathbf{u}}) \cdot \bar{\mathbf{u}} = \tilde{\mathbf{u}}^2 + 2\tilde{\mathbf{u}} \cdot \nabla\phi$, (5.3) becomes

$$\Delta T = \widetilde{T} + T_{\mathcal{S}} + T_{\mathcal{C}}; \quad \begin{cases} \widetilde{T} = \tfrac{1}{2}\iiint_{\mathcal{V}} \rho \tilde{\mathbf{u}}^2 \,\mathrm{d}\mathcal{V} \\ T_{\mathcal{S}} = \iiint_{\mathcal{V}} \rho \tilde{\mathbf{u}} \cdot \nabla\phi \,\mathrm{d}\mathcal{V} \\ T_{\mathcal{C}} = \tfrac{1}{2}\iiint_{\mathcal{V}} \delta_\rho \bar{\mathbf{u}}^2 \,\mathrm{d}\mathcal{V} \end{cases} \tag{5.5}$$

where $\widetilde{T}$ stands for the kinetic energy associated with the vortical contribution and $T_{\mathcal{S}}$ represents the energy associated with the vortical component of motion in the direction of the velocity potential vector. This term reduces to a surface integral, hence the subscript. Finally, $T_{\mathcal{C}}$ represents the energy associated with the irrotational motion weighted by δ_ρ. Evidently, for $\Delta T \geq 0$, it is necessary and sufficient to impose

$$\tfrac{1}{2}\iiint_{\mathcal{V}} \rho \tilde{\mathbf{u}}^2 \,\mathrm{d}\mathcal{V} + \iiint_{\mathcal{V}} \rho \tilde{\mathbf{u}} \cdot \nabla\phi \,\mathrm{d}\mathcal{V} + \tfrac{1}{2}\iiint_{\mathcal{V}} \delta_\rho \bar{\mathbf{u}}^2 \,\mathrm{d}\mathcal{V} \geq 0 \tag{5.6}$$

However, given that $\rho > 0$, then $\widetilde{T} \geq 0$ for any rotational motion. Therefore, for $\Delta T \geq 0$, it is sufficient to show that

$$T_{\mathcal{S}} + T_{\mathcal{C}} = \iiint_{\mathcal{V}} \rho \tilde{\mathbf{u}} \cdot \nabla \phi \, \mathrm{d}\mathcal{V} + \tfrac{1}{2} \iiint_{\mathcal{V}} \delta_{\rho} \bar{\mathbf{u}}^2 \, \mathrm{d}\mathcal{V} \geq 0 \tag{5.7}$$

By using

$$\rho \tilde{\mathbf{u}} \cdot \nabla \phi = \nabla \cdot (\rho \phi \tilde{\mathbf{u}}) - \phi \nabla \cdot (\rho \tilde{\mathbf{u}}) \tag{5.8}$$

in conjunction with the divergence theorem, we have

$$T_{\mathcal{S}} = \iiint_{\mathcal{V}} \rho \tilde{\mathbf{u}} \cdot \nabla \phi \, \mathrm{d}\mathcal{V} = \iint_{\mathcal{S}} \rho \phi \tilde{\mathbf{u}} \cdot \mathbf{n} \, \mathrm{d}\mathcal{S} - \iiint_{\mathcal{V}} \phi \nabla \cdot (\rho \tilde{\mathbf{u}}) \, \mathrm{d}\mathcal{V} \tag{5.9}$$

Pursuant to Kelvin's argument, $\mathbf{u}$ and $\bar{\mathbf{u}}$ must exhibit the same normal velocity along the boundary of $\mathcal{V}$ or else vanish, thus defining a Kelvin surface. Using $\mathcal{S}$ to denote a surface that envelops the fluid, one may seek a more general case by decomposing $\mathcal{S}$ into

$$\mathcal{S} = \mathcal{S}_{\mathrm{K}} + \mathcal{S}_{\mathrm{o}} \tag{5.10}$$

where $\mathcal{S}_{\mathrm{K}}$ and $\mathcal{S}_{\mathrm{o}}$ represent the Kelvin and open surfaces, respectively. Velocity constraints at the boundaries include

$$\begin{cases} \mathcal{S}_{\mathrm{K}}: & \tilde{\mathbf{u}} \cdot \mathbf{n} = (\mathbf{u} - \nabla \phi) \cdot \mathbf{n} = 0 \\ \mathcal{S}_{\mathrm{o}}: & \tilde{\mathbf{u}} \cdot \mathbf{n} \neq \mathbf{u} \cdot \mathbf{n} \neq 0 \end{cases} \tag{5.11}$$

Then, the first term in (5.9) becomes

$$\iint_{\mathcal{S}} \rho \phi \tilde{\mathbf{u}} \cdot \mathbf{n} \, \mathrm{d}\mathcal{S} = \iint_{\mathcal{S}_{\mathrm{K}}} \rho \phi \tilde{\mathbf{u}} \cdot \mathbf{n} \, \mathrm{d}\mathcal{S} + \iint_{\mathcal{S}_{\mathrm{o}}} \rho \phi \tilde{\mathbf{u}} \cdot \mathbf{n} \, \mathrm{d}\mathcal{S} = \iint_{\mathcal{S}_{\mathrm{o}}} \rho \phi \tilde{\mathbf{u}} \cdot \mathbf{n} \, \mathrm{d}\mathcal{S} \tag{5.12}$$

so that (5.7) reduces to

$$\underbrace{\iint_{\mathcal{S}_\mathrm{o}} \rho\phi\tilde{\mathbf{u}}\cdot\mathbf{n}\,\mathrm{d}\mathcal{S}}_{T_\mathrm{o}} + \underbrace{\tfrac{1}{2}\iiint_{\mathcal{V}} \delta_\rho\bar{\mathbf{u}}^2\,\mathrm{d}\mathcal{V}}_{T_\mathcal{C}} \geq \underbrace{\iiint_{\mathcal{V}} \phi\nabla\cdot(\rho\tilde{\mathbf{u}})\,\mathrm{d}\mathcal{V}}_{T_\phi} \tag{5.13}$$

where T_o represents a weighted flux of the vortical motion through the open boundaries and T_ϕ represents the weighted divergence of the vortical component. □

In Kelvin's classic theorem, the fluid is assumed to be homogeneous incompressible, hence, $\delta_\rho = 0$ and $\nabla\cdot\rho\tilde{\mathbf{u}} = 0$. Also, the vortical motion vanishes on all boundaries, thus yielding $\tilde{\mathbf{u}}\cdot\mathbf{n} = 0$ on $\mathcal{S}$. This permits setting $T_\mathcal{S} = T_\mathcal{C} = 0$ in (5.5) and deducing that $\Delta T \geq 0$ with $\widetilde{T} \geq 0$ for any rotational field. It can therefore be seen that taking $\mathcal{S}$ to be a Kelvin surface and the fluid to be homogeneous incompressible ensures that the energy associated with the potential field remains a minimum.

In what follows, we consider special cases of Theorem 5.1 for which the general criteria given by (5.6) and (5.13) are substantially reduced.

Corollary 5.1.1 (Compressible flow with Kelvin boundaries)**.** *The irrotational motion* $\bar{\mathbf{u}}$ *of a steady compressible fluid of density* $\bar{\rho}$ *in a simply connected fluid region* $\mathcal{V}$ *carries less kinetic energy than any other motion* $\mathbf{u}$ *of density* ρ *with the same normal velocity at its boundary* ($\mathbf{u}\cdot\mathbf{n} = \bar{\mathbf{u}}\cdot\mathbf{n}$) *provided that the following sufficient condition is satisfied*

$$\tfrac{1}{2}\iiint_{\mathcal{V}} \delta_\rho\bar{\mathbf{u}}^2\,\mathrm{d}\mathcal{V} \geq \iiint_{\mathcal{V}} \phi\nabla\cdot(\rho\tilde{u})\,\mathrm{d}\mathcal{V} \tag{5.14}$$

Proof of Corollary 5.1.1. Having the same normal velocity at the boundary, then $\tilde{\mathbf{u}}\cdot\mathbf{n} = 0$. Therefore, the condition given by (5.13) reduces to

$$\tfrac{1}{2}\iiint_{\mathcal{V}} \delta_\rho\bar{\mathbf{u}}^2\,\mathrm{d}\mathcal{V} \geq \iiint_{\mathcal{V}} \phi\nabla\cdot(\rho\tilde{u})\,\mathrm{d}\mathcal{V} \tag{5.15}$$

since $T_\mathrm{o} = 0$. □

Corollary 5.1.2 (Homogeneous incompressible flow with open boundaries)**.** *The irrotational motion* $\bar{\mathbf{u}}$ *of a steady homogeneous incompressible fluid of density* ρ *in a simply connected fluid region* $\mathcal{V}$ *carries less kinetic energy than any other motion* $\mathbf{u}$ *with or without the same normal velocity at its boundary* $(\mathbf{u}\cdot\mathbf{n} \neq \bar{\mathbf{u}}\cdot\mathbf{n})$ *provided that the following sufficient condition is satisfied*

$$\iint_{\mathcal{S}_\circ} \phi\tilde{\mathbf{u}}\cdot\mathbf{n}\,\mathrm{d}\mathcal{S} \geq 0 \tag{5.16}$$

Proof of Corollary 5.1.2. For homogeneous incompressible fluids, the density is constant $(\bar{\rho} = \rho)$ and $\delta_\rho = 0$. In this case,

$$\nabla\cdot(\rho\tilde{\mathbf{u}}) = \rho\nabla\cdot\tilde{\mathbf{u}} = \rho(\nabla\cdot\mathbf{u} - \nabla\cdot\bar{\mathbf{u}}) = 0 \tag{5.17}$$

Then, by virtue of (5.13), the sufficient condition becomes

$$\iint_{\mathcal{S}_\circ} \phi\tilde{\mathbf{u}}\cdot\mathbf{n}\,\mathrm{d}\mathcal{S} \geq 0 \tag{5.18}$$

□

5.3 Discussion

In what follows, we discuss some of the implications brought about by the preceding derivations.

Multi-Valued potentials

For a multi-valued potential such as that corresponding to the flow in multiply connected regions, the theorem no longer holds unless one selects the particular solution that bears the least kinetic energy among all potential solutions. Alternatively, if one defines a velocity potential as the difference between two possible potential solutions

having the same cyclic constant ($\phi = \phi_0 - \phi_1$), then the theorem will be true owing to the resulting potential becoming unique (Batchelor 1967).

Mass equiflux condition

When the flow is incompressible, an immediate consequence of the boundary decomposition in (5.11) is that the mass flowrates of the potential and rotational motions are equal at the open boundary. This can be shown by first recalling that the vortical component of motion is divergence free, or

$$\rho \iint_{\mathcal{S}} \tilde{\mathbf{u}} \cdot \mathbf{n} \, \mathrm{d}\mathcal{S} = 0 \tag{5.19}$$

But, given that $\tilde{\mathbf{u}} \cdot \mathbf{n} = 0$ on $\mathcal{S}_\mathrm{K}$, we have

$$\rho \iint_{\mathcal{S}} \tilde{\mathbf{u}} \cdot \mathbf{n} \, \mathrm{d}\mathcal{S} = \rho \iint_{\mathcal{S}_\mathrm{o}} \tilde{\mathbf{u}} \cdot \mathbf{n} \, \mathrm{d}\mathcal{S} = 0 \tag{5.20}$$

Finally, we recover the mass equiflux condition at an open boundary

$$\iint_{\mathcal{S}_\mathrm{o}} \mathbf{u} \cdot \mathbf{n} \, \mathrm{d}\mathcal{S} = \iint_{\mathcal{S}_\mathrm{o}} \bar{\mathbf{u}} \cdot \mathbf{n} \, \mathrm{d}\mathcal{S} \tag{5.21}$$

This condition holds for incompressible motions and is congruent with the search for motions with comparable kinetic energies that share "similar" conditions at their boundaries. Equation (5.21) can also be used to achieve closure in underdetermined potential motions. This corresponds to potential flow problems that lack a sufficient number of boundary conditions to secure a unique velocity potential.

Arbitrary constants

In general, velocity potentials are defined up to an arbitrary constant. One can show that the addition of a constant A has no effect on Theorem 5.1. To that end, we

replace ϕ by $(\phi + A)$ in (5.13) and write

$$\iint_{\mathcal{S}_\circ} \rho\phi\tilde{\mathbf{u}} \cdot \mathbf{n}\,\mathrm{d}\mathcal{S} + \tfrac{1}{2}\iiint_{\mathcal{V}} \delta_\rho \bar{\mathbf{u}}^2\,\mathrm{d}\mathcal{V} + \iint_{\mathcal{S}_\circ} \rho A\tilde{\mathbf{u}} \cdot \mathbf{n}\,\mathrm{d}\mathcal{S} \geq \iiint_{\mathcal{V}} \phi\nabla \cdot \rho\tilde{\mathbf{u}}\,\mathrm{d}\mathcal{V} + \iiint_{\mathcal{V}} A\nabla \cdot \rho\tilde{\mathbf{u}}\,\mathrm{d}\mathcal{V} \quad (5.22)$$

but, using the divergence theorem, we have

$$\iiint_{\mathcal{V}} A\nabla \cdot \rho\tilde{\mathbf{u}}\,\mathrm{d}\mathcal{V} = \iint_{\mathcal{S}_\circ} A\rho\tilde{\mathbf{u}} \cdot \mathbf{n}\,\mathrm{d}\mathcal{S} \quad (5.23)$$

where, upon substitution into (5.22), we recover the original form

$$\iint_{\mathcal{S}_o} \rho\phi\tilde{\mathbf{u}} \cdot \mathbf{n}\,\mathrm{d}\mathcal{S} + \tfrac{1}{2}\iiint_{\mathcal{V}} \delta_\rho \bar{\mathbf{u}}^2\,\mathrm{d}\mathcal{V} \geq \iiint_{\mathcal{V}} \phi\nabla \cdot \rho\tilde{\mathbf{u}}\,\mathrm{d}\mathcal{V} \quad (5.24)$$

This result equally applies to corollaries 5.1.1 and 5.1.2.

5.4 Applications

Of the variety of fluid dynamics applications that exhibit open boundaries, we select a few that correspond to classic problems described by Poiseuille (White 2005), Taylor (Taylor 1956), and Culick (Culick 1966). We start by revisiting the variational solutions from Chapter 4 and confirm that the least kinetic energy solution indeed corresponds to the irrotational motion. Then, we apply the present extension to the Poiseuille flow in ducts of arbitrary cross section, Taylor's flow in a porous channel, and the complex-lamellar bidirectional vortex motion in a confined cylinder.

5.4.1 Variations solutions for the Taylor–Culick Flow

We start by recalling the families of solutions obtained in Chapter 4. Since both types of solutions observe identical boundary conditions, then they must share the same unique velocity potential. In this case, the potential function may be obtained from

solving the Laplacian of ϕ over the domain defined by $0 \leq r \leq 1$ and $0 \leq z \leq L$. The boundary conditions translate into

$$\frac{\partial \phi(0,z)}{\partial r} = 0 \tag{5.25a}$$

$$\frac{\partial \phi(r,0)}{\partial z} = 0 \tag{5.25b}$$

$$\frac{\partial \phi(1,z)}{\partial r} = -1 \tag{5.25c}$$

Note that the no-slip condition has been excluded from (5.25) since the flow is irrotational. The resulting potential, shared by all solutions, is

$$\phi(r,z) = -\tfrac{1}{2}r^2 + z^2 \tag{5.26}$$

It may also prove to be easier to solve for the streamfunction. In this case, one uses the vorticity equation by noting that $\mathbf{\Omega} = \mathbf{0}$, or

$$\frac{\partial^2 \psi}{\partial z^2} + \frac{\partial^2 \psi}{\partial r^2} - \frac{1}{r}\frac{\partial \psi}{\partial r} = 0 \tag{5.27}$$

Then, separation of variables can be called upon to solve (5.27). At the outset, one recovers

$$\psi = r^2 z \tag{5.28}$$

The irrotational velocity field is

$$\bar{\mathbf{u}} = -r\mathbf{e}_r + 2z\mathbf{e}_z \tag{5.29}$$

The velocity field of the variational solutions is given by

$$\mathbf{u} = -r^{-1}\sum \alpha_n \sin\chi_n \mathbf{e}_r + \pi z \sum (2n+1)\alpha_n \cos\chi_n \mathbf{e}_z \tag{5.30}$$

where $\chi_n = \frac{1}{2}(2n+1)\pi r^2$. Finally, the vortical component of motion, for both Type I and Type II solutions, can be expressed via

$$\tilde{\mathbf{u}} = \mathbf{u} - \bar{\mathbf{u}} = \left(-r^{-1}\sum \alpha_n \sin\chi_n + r\right)\mathbf{e}_r + \left[\pi \sum \alpha_n z(2n+1)\cos\chi_n - 2z\right]\mathbf{e}_z \quad (5.31)$$

When evaluated over the boundary, (5.31) vanishes everywhere except in the exit plane at $z = L$, which constitutes an open boundary. Then, to test the condition given by (5.16), we are only required to integrate over the exit plane. This operation yields

$$\begin{aligned} T_o &= \iint_{\mathcal{S}_o} \phi\tilde{\mathbf{u}}\cdot\mathbf{n}\,\mathrm{d}\mathcal{S} = \iint_{\mathcal{S}_o} (\phi\, w)|_{z=L}\,\mathrm{d}\mathcal{S} \\ &= 2\pi L\int_0^1 \left(L^2 - \tfrac{1}{2}r^2\right)\left[\pi\sum \alpha_n(2n+1)^{-1}\cos\chi_n - 2\right] r\,\mathrm{d}r \end{aligned} \quad (5.32)$$

Upon integration, we recover

$$T_o = 2L\sum \alpha_n(2n+1)^{-1} - \tfrac{1}{2}\pi L \quad (5.33)$$

By replacing α_n with either α_n^- or α_n^+ given by (4.25) and (4.31), we can immediately see that $T_o \geq 0$ as a consequence of

$$2L\sum \alpha_n(2n+1)^{-1} \geq \tfrac{1}{2}\pi; \quad \forall\, q \geq 2 \quad \text{(Type I and II)} \quad (5.34)$$

This ensures that $\bar{T} \leq T$. The case of $T_o = 0$ corresponds to the irrotational Type I solution with $q = 2$ since $\bar{T} = T$. This confirms that the solution bearing the least kinetic energy is indeed the potential flow solution.

5.4.2 Poiseuille flow in ducts of arbitrary cross sections

For this class of problems, the velocity potential corresponds to that of a uniform planar flow such that the velocity remains parallel to the channel walls. With the

potential and rotational velocities being axially independent, and having a single inlet and outlet as open boundaries, it can be easily seen that

$$T_{\mathrm{o}} = \iint_{\mathcal{S}_{\mathrm{o}}} \phi\tilde{\mathbf{u}} \cdot \mathbf{n}\, \mathrm{d}\mathcal{S} = \iint_{\mathcal{S}_{\mathrm{inlet}}} \phi\tilde{\mathbf{u}} \cdot \mathbf{n}\, \mathrm{d}\mathcal{S} - \iint_{\mathcal{S}_{\mathrm{outlet}}} \phi\tilde{\mathbf{u}} \cdot \mathbf{n}\, \mathrm{d}\mathcal{S} = 0 \tag{5.35}$$

Specific velocity profiles may be obtained from Batchelor (1967) or White (2005). It is clear that the lower limit in (5.16) is always met.

5.4.3 Taylor flow in a porous channel

For the Taylor flow in a porous channel (Saad and Majdalani 2007, 2009b), the potential corresponds to a power law conformal map with an exponent of 2. This may be written as

$$\phi + \mathrm{i}\,\psi = \tfrac{1}{2}z^2; \quad z = x + \mathrm{i}\,y \tag{5.36}$$

Subsequently, the corresponding velocity potential, streamfunction, and velocity field are expressed as

$$\phi = \tfrac{1}{2}(x^2 - y^2); \quad \psi = xy; \quad \bar{\mathbf{u}} = x\,\mathbf{e}_x - y\,\mathbf{e}_y \tag{5.37}$$

This irrotational solution may also be obtained by solving $\nabla^2\psi = 0$ with a suitable set of boundary conditions, namely,

$$\begin{cases} u(0,y) = \dfrac{\partial\psi(0,y)}{\partial y} = 0; & \text{impermeable headwall} \quad \text{(a)} \\ v(x,1) = -\dfrac{\partial\psi(x,1)}{\partial x} = -1; & \text{constant sidewall injection} \quad \text{(b)} \\ v(x,0) = -\dfrac{\partial\phi(1,z)}{\partial r} = 0; & \text{no flow across the symmetry plane} \quad \text{(c)} \end{cases} \tag{5.38}$$

Taylor's solution for this problem is given by

$$\psi = z\sin(\tfrac{1}{2}\pi y); \quad \mathbf{u} = \tfrac{1}{2}\pi x\cos\left(\tfrac{1}{2}\pi y\right)\mathbf{e}_x - \sin\left(\tfrac{1}{2}\pi y\right)\mathbf{e}_y \tag{5.39}$$

The vortical part may be extracted from

$$\tilde{\mathbf{u}} = \mathbf{u} - \bar{\mathbf{u}} = \left[\tfrac{1}{2}\pi x \cos\left(\tfrac{1}{2}\pi y\right) - x\right] \mathbf{e}_x + \left[y - \sin\left(\tfrac{1}{2}\pi y\right)\right] \mathbf{e}_y \equiv \tilde{u}\mathbf{e}_x + \tilde{v}\mathbf{e}_y \tag{5.40}$$

In this problem, the exit plane constitutes the only open boundary at $z = L$. Application of (5.16) yields

$$\begin{aligned} T_o &= \iint_{\mathcal{S}_o} \phi\tilde{\mathbf{u}} \cdot \mathbf{n}\, \mathrm{d}\mathcal{S} = \iint_{\mathcal{S}_o} (\phi\, \tilde{u})|_{x=L}\, \mathrm{d}\mathcal{S} \\ &= \int_0^1 \tfrac{1}{2}\left(L^2 - y^2\right)\left[\tfrac{1}{2}\pi L \cos\left(\tfrac{1}{2}\pi y\right) - L\right] \mathrm{d}y = \left(4\pi^{-2} - \tfrac{1}{3}\right) L > 0 \end{aligned} \tag{5.41}$$

Thus, Kelvin's extended theorem shows that the irrotational motion of the Taylor problem carries the least kinetic energy. It is worthy to note here that Saad and Majdalani (2008a) applied a variational procedure to the Taylor flow and obtained an independent verification that the irrotational solution indeed carries the least kinetic energy. This reassuring conclusion helps confirm the validity of Kelvin's theorem extension to regions with open boundaries.

5.4.4 Bidirectional vortex in a confined cylinder

The confined bidirectional vortex is illustrated schematically in Figure 5.2. It pertains to the bipolar swirling motion of an incompressible fluid in a cylindrical chamber of height L and unit radius. This problem has been extensively investigated by Majdalani and co-workers (Majdalani 2009; Majdalani and Chiaverini 2009; Maicke and Majdalani 2009; Saad and Majdalani 2008b; Majdalani and Rienstra 2007; Vyas and Majdalani 2006). A characteristic of the bidirectional vortex is the presence of a rotating fluid interface known as the mantle. This so-called spinning wheel separates the outer and inner vortex regions at a radius of $r = \beta$ (Majdalani and Chiaverini 2009; Majdalani 2009). In this vein, the mantle position β denotes the locus of points along which the axial flow vanishes before switching spatial polarity. The velocity

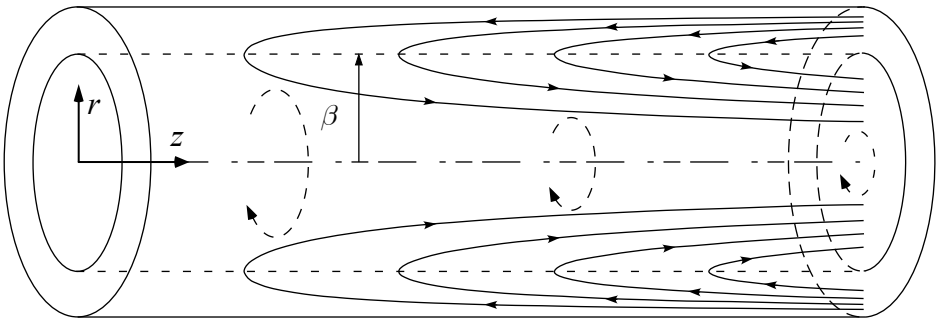

Figure 5.2: Schematic of the bidirectional vortex motion in a confined cylindrical chamber of unit radius and length L.

potential for the bidirectional vortex can be determined by first splitting the domain into two regions. An inner cylinder bounded by the mantle ($0 \leq r < \beta$) and an outer annulus extending from the mantle to the sidewall ($\beta < r \leq 1$). Corresponding boundary conditions consist of

$$0 \leq r < \beta : \begin{cases} \bar{w}(r,0) = 0 \\ \bar{u}(0,z) = 0 \end{cases} \quad ; \quad \beta < r \leq 1 : \begin{cases} \bar{w}(r,0) = 0 \\ \bar{u}(1,z) = 0 \end{cases} \quad ; \quad \bar{v}(1,z) = 1 \tag{5.42}$$

Then, by using $\phi = f(r) + g(\theta) + h(z)$ in $\nabla^2 \phi = 0$, one arrives at

$$\phi = \begin{cases} -\frac{1}{2} a_0 r^2 + \theta + a_0 z^2; & 0 \leq r < \beta \\ -b_0(\frac{1}{2} r^2 - \ln r) + \theta + b_0 z^2; & \beta < r \leq 1 \end{cases} \tag{5.43}$$

and so

$$\bar{\mathbf{u}} = \begin{cases} -a_0 r \mathbf{e}_r + r^{-1} \mathbf{e}_\theta + 2 a_0 z \mathbf{e}_z; & 0 \leq r < \beta \\ -b_0 (r - r^{-1}) \mathbf{e}_r + r^{-1} \mathbf{e}_\theta + 2 b_0 z \mathbf{e}_z; & \beta < r \leq 1 \end{cases} \tag{5.44}$$

The constants a_0 and b_0 are related by matching the inner and outer radial velocities at the mantle via

$$b_0 = \frac{\beta^2 a_0}{\beta^2 - 1} \tag{5.45}$$

While the mantle location is prescribed by the rotational motion, a_0 must be evaluated, by virtue of (5.21), from mass conservation at the open bounday:

$$\int_0^\beta \bar{w}(r, L) r \, \mathrm{d}r = \int_0^\beta w(r, L) r \, \mathrm{d}r \tag{5.46}$$

In some rotational models of bidirectional vortex motions, the radial velocity is axially invariant to the extent of permitting the use of an equivalent approach for determining a_0. This can be accomplished by setting $\bar{u}(\beta) = u(\beta)$ or $a_0 = -\beta^{-1} u(\beta)$.

Vyas and Majdalani (2006) introduced an inviscid rotational model for the bidirectional vortex of the complex lamellar type for which $\mathbf{u} \cdot (\nabla \times \mathbf{u}) = 0$. Their model is summarized by

$$\mathbf{u} = -r^{-1} \sin(\pi r^2) \mathbf{e}_r + r^{-1} \mathbf{e}_\theta + 2\pi z \cos(\pi r^2) \mathbf{e}_z \tag{5.47}$$

where, for simplicity, we have set $\kappa = 1$ in their original solution. The mantle, in this case, is located at $\beta = 1/\sqrt{2} \simeq 0.707$. The vortical component of (5.47) can be written as

$$\tilde{\mathbf{u}} = \begin{cases} \left[2r - r^{-1} \sin(\pi r^2)\right] \mathbf{e}_r + \left[2\pi z \cos(\pi r^2) - 4z\right] \mathbf{e}_z; & 0 \le r < \sqrt{2}/2 \\ -\left[r^{-1} \sin(\pi r^2) + (2r - 2r^{-1})\right] \mathbf{e}_r + \left[2\pi z \cos(\pi r^2) + 4z\right] \mathbf{e}_z; & \sqrt{2}/2 < r \le 1 \end{cases} \tag{5.48}$$

where $a_0 = b_0 = 2$ for this particular model. By evaluating (5.16) along the open boundary at $z = L$, we recover

$$\begin{aligned} T_\mathrm{o} &= \iint_{\mathcal{S}_\mathrm{o}} \phi \, \tilde{\mathbf{u}} \cdot \mathbf{n} \, \mathrm{d}\mathcal{S} = \iint_{\mathcal{S}_\mathrm{o}} (\phi \, \tilde{w})|_{z=L} \, \mathrm{d}\mathcal{S} \\ &= \int_0^{2\pi} \int_0^{\sqrt{2}/2} \left(2L^2 + \theta - r^2\right) \left[2\pi L \cos(\pi r^2) - 4L\right] r \, \mathrm{d}r \, \mathrm{d}\theta \\ &+ \int_0^{2\pi} \int_{\sqrt{2}/2}^1 \left(r^2 - 2\ln r + \theta - 2L^2\right) \left[2\pi L \cos(\pi r^2) + 4L\right] r \, \mathrm{d}r \, \mathrm{d}\theta \end{aligned} \tag{5.49}$$

and so

$$T_{\text{o}} = 2\left[1 - \ln 4 + \text{Si}(\pi) - \text{Si}\left(\tfrac{1}{2}\pi\right)\right]\pi L \simeq 0.596L > 0 \tag{5.50}$$

where $\text{Si}(\theta) = \int_0^\theta t^{-1}\sin t\,\mathrm{d}t$ is the sine integral function. This result verifies that the irrotational motion carries the least kinetic energy for the bidirectional vortex. In fact, Saad and Majdalani (2008b) obtained an independent confirmation of this fact by using the Lagrangian optimization technique. Not only does this result enable us to benchmark the present extension of Kelvin's theorem, but it also presents an avenue for displaying the delicate harmony between Kelvin's minimum energy theorem and the Lagrangian minimization principle.

5.5 Summary

In this chapter, we present an extension of Kelvin's minimum energy theorem to compressible flows in regions with open boundaries. After deriving a general form of the theorem, two corollaries are discussed for which the global criteria are substantially simplified. It is found that Kelvin's theorem remains generally valid provided a simple criterion is in check for each of the cases considered. This is followed by a discussion about the specific situations where these criteria are always met. The criterion corresponding to the case of homogeneous incompressible flow is then tested on the variational solutions discussed in Chapter 4 to confirm that the least kinetic energy solution (Type I, $q = 2$) indeed corresponds to the irrotational motion. Finally, three classic fluid dynamics problems that exhibit open boundaries are considered; namely, Poiseuille flow in ducts of arbitrary cross sections, Taylor's flow in a porous channel, and the complex-lamellar bidirectional motion in a confined cylinder. The results confirm that the irrotational motion carries the least kinetic energy thus enabling us to apply the extended form of the theorem to a wider class of problems with varying degrees of topological complexities as well as arbitrary velocity specifications at the boundaries.

Chapter 6

Regressing Walls

In this chapter, we derive the governing equations for the viscous flow in a porous cylinder with regressing walls. By using physical arguments and a similarity transform in space and time, the Navier-Stokes equations are reduced to a single ODE that can be solved analytically using a variety of classic and novel techniques. This chapter illustrates the derivation of the governing equations for this classic problem. It also contains the details of the numerical method that is used to solve these equations. Chapters 7 and 8 will deal with the details of the analytical solution for this problem by using regular perturbation and Adomian's decomposition method (ADM), respectively.

6.1 Introduction

The preceding chapters dealt with approximating the mean flow in a porous cylinder using an inviscid rotational formulation. These were used to model the average flow inside solid and hybrid rocket motors. In practice, as the fuel grain burns, the internal radius of the motor increases and thus affects the mean and transient properties of the flowfield. Although the time scales in this case are very small compared to the total burn time, it would be quite a feat, no to say impossible, to resolve all the scales.

However, by making a suitable similarity transform, the problem with wall regression can be simplified to the extent of obtaining a practical solution.

In this chapter, we derive the governing equations for the viscous flow in a porous cylinder with regressing walls. By using physical arguments and a similarity transform in space and time, the Navier-Stokes equations are reduced to a single ODE that can be solved analytically using regular perturbation and the Adomian Decomposition Method (ADM). Here, we only present the derivation of the governing equations as well as the numerical strategy to solve this problem. Chapters 7 and 8 will be devoted to the analytical solution of this problem using regular perturbation and Adomian's decomposition method (ADM), respectively.

6.2 Mathematical model

As usual, the cylindrical propellant grain of a solid rocket motor is modeled as a long tube with one end closed at the headwall, while the other remains open. The cylindrical wall is assumed to be permeable so as to simulate the propellant burning and normal gas injection. Furthermore, the wetted area of the pipe is allowed to radially expand at a speed equal to $\dot{a}$. For this to happen, the mathematical model requires that the headwall area stretches accordingly to accommodate the expansion of the cylinder. This is shown in Figure 6.1 where an axisymmetric coordinate system has been chosen. By assuming an incompressible mean flow, the vorticity transport equation is written as

$$\frac{\partial \mathbf{\Omega}^*}{\partial t} - \nabla^* \times \mathbf{u}^* \times \mathbf{\Omega}^* = \nu \nabla^* \times \nabla^{*2} \mathbf{u}^* \tag{6.1}$$

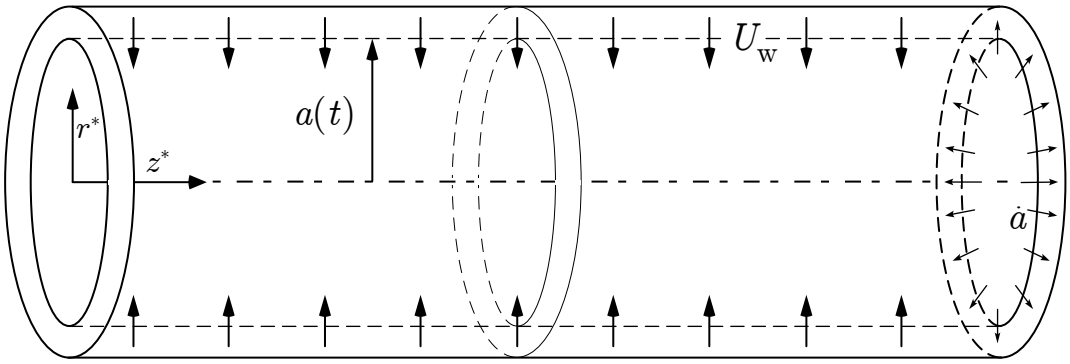

Figure 6.1: Schematic of a cylindrical chamber used to illustrate sidewall injection and wall regression as well as the control volume used to evaluate the average axial velocity.

6.2.1 Boundary conditions

These can be organized as follows

$$r^* = a(t) : \begin{cases} w^* = 0; & \text{no slip} \\ u^* = -U; & \text{sidewall injection} \end{cases} \tag{6.2}$$

$$r^* = 0 : \begin{cases} u^* = 0; & \text{no flow across the centerline} \\ ; \dfrac{\partial w^*}{\partial r^*} = 0; & \text{axial velocity symmetry} \end{cases} \tag{6.3}$$

$$z^* = 0 : \quad w^* = 0 \quad \text{inert headwall} \tag{6.4}$$

Here, U is the absolute fluid injection velocity at the wall. This is defined as the fluid velocity seen by an observer in a reference frame located outside the tube. In this vein, if U_w is used to denote the fluid velocity with respect to the wall, then we have the following relation

$$U = U_w - \dot{a} \tag{6.5}$$

so that if the walls are stationary the absolute and relative velocities are equal. If the wall is moving radially inwards, then $\dot{a} < 0$ and the fluid is seen to be injected at

a larger speed than U_{w}. Conversly, if the the wall is moving radially outwards, then $\dot{a} > 0$ and the fluid injection velocity is seen to be smaller than U_{w}.

6.2.2 Similarity in space

By inspection, one expects the axial velocity to vary linearly in z^*. To demonstrate this, we consider the control volume delineated by the dashed lines in Figure 6.1. Then, by applying a mass balance on the inlet and outlet surfaces, we have

$$\frac{\partial}{\partial t}\int_{\mathcal{V}} \rho \,\mathrm{d}\mathcal{V} + \iint_{\mathcal{S}} \rho \mathbf{u}^* \cdot \mathbf{n} \,\mathrm{d}\mathcal{S} = 0 \tag{6.6}$$

or

$$\frac{\partial \mathcal{V}}{\partial t} + \iint_{\mathcal{S}_{\mathrm{exit}}} \mathbf{u}^* \cdot \mathbf{n} \,\mathrm{d}\mathcal{S} + \iint_{\mathcal{S}_{\mathrm{sidewall}}} \mathbf{u}^* \cdot \mathbf{n} \,\mathrm{d}\mathcal{S} = 0 \tag{6.7}$$

this yields

$$\frac{\partial \mathcal{V}}{\partial t} + \iint_{\mathcal{S}_{\mathrm{exit}}} \mathbf{u}^* \cdot \mathbf{n} \,\mathrm{d}\mathcal{S} - 2\pi U a z^* = 0 \tag{6.8}$$

The second integral in (6.8) is related to the average axial velocity W_{m} inside the volume via

$$W_{\mathrm{m}} = \frac{1}{\pi a^2} \iint_{\mathcal{S}_{\mathrm{exit}}} \mathbf{u}^* \cdot \mathbf{n} \,\mathrm{d}\mathcal{S} \tag{6.9}$$

Then, substitution in (6.8) gives

$$\frac{\partial \mathcal{V}}{\partial t} + \pi a^2 W_{\mathrm{m}} - 2\pi U a z^* = 0 \tag{6.10}$$

Using $\mathcal{V} = \pi a^2 z^*$, (6.10) reduces to

$$2\pi a \dot{a} z^* + \pi a^2 W_{\mathrm{m}} - 2\pi U a z^* = 0 \tag{6.11}$$

which, upon simplification, yields

$$W_{\mathrm{m}} = 2U\frac{z^*}{a} \tag{6.12}$$

but, since the average velocity is defined as

$$W_{\mathrm{m}}(z^*,t) = \frac{1}{\pi a^2}\int_0^a w^*(r^*,z^*,t) r^*\,\mathrm{d}r^* = 2U\frac{z^*}{a} \tag{6.13}$$

then, the only admissible form of the axial velocity is

$$w^*(r^*,z^*,t) = z^* f(r^*,t) \tag{6.14}$$

6.2.3 Vorticity transport

We introduce the stokes streamfunction via

$$u^* = -\frac{1}{r^*}\frac{\partial \psi^*}{\partial z^*}; \quad w^* = \frac{1}{r^*}\frac{\partial \psi^*}{\partial r^*} \tag{6.15}$$

Based on (6.14), the streamfunction may be written as

$$\psi^* = \nu z^* F(r,t); \quad r = \frac{r^*}{a} \tag{6.16}$$

Note that $F(r,t)$ is dimensionless. The radial and axial velocities can now be expressed in terms of F. This operation yields

$$u^* = -\frac{\nu}{ar}F; \quad w^* = \frac{\nu z^*}{a^2 r}\frac{\partial F}{\partial r} \tag{6.17}$$

Since u^* is independent of the axial coordinate, then the vorticity has a single nonzero component given by

$$\Omega^* = \Omega^*_\theta = \frac{\partial u^*}{\partial z^*} - \frac{\partial w^*}{\partial r^*} = -\frac{\partial w^*}{\partial r^*} \tag{6.18}$$

Upon substitution of (6.18) into (6.1), one recovers

$$\frac{\partial}{\partial r^*}\left(\frac{\partial w^*}{\partial t}\right) + \frac{\partial}{\partial r^*}\left(u\frac{\partial w^*}{\partial r^*}\right) + \frac{\partial}{\partial r^*}\left(w^*\frac{\partial w^*}{\partial z^*}\right) - \nu\frac{\partial}{\partial r^*}\left[\frac{1}{r^*}\frac{\partial}{\partial r^*}\left(r^*\frac{\partial w^*}{\partial r^*}\right)\right] = 0 \tag{6.19}$$

where we have used the fact that

$$\frac{\partial}{\partial z^*}\left(w\frac{\partial w}{\partial r^*}\right) = \frac{\partial}{\partial r^*}\left(w\frac{\partial w}{\partial z^*}\right) \tag{6.20}$$

We now evaluate every term in (6.19) paying careful attention to partial differentiation

$$\frac{\partial w^*}{\partial t} = \frac{\nu z^*}{a^2}\left(\frac{F_r}{r}\right)_t - \frac{2\nu z^*}{a^3}\frac{F_r}{r}\dot{a} \tag{6.21a}$$

$$\frac{\partial w^*}{\partial r^*} = \frac{\nu z^*}{a^3}\left(\frac{F_r}{r}\right)_r \tag{6.21b}$$

$$\frac{w^*}{z^*} = \frac{\nu}{a^2}\frac{F_r}{r} \tag{6.21c}$$

$$u^*\frac{w^*}{\partial r^*} = -\frac{\nu^2 z^*}{a^4}\frac{F}{r}\left(\frac{F_r}{r}\right)_r \tag{6.21d}$$

$$w^*\frac{\partial w^*}{\partial z^*} = \frac{\nu^2 z^*}{a^4}\left(\frac{F_r}{r}\right)^2 \tag{6.21e}$$

$$\frac{1}{r^*}\frac{\partial}{\partial r^*}\left(r^*\frac{\partial w^*}{\partial r^*}\right) = \frac{\nu z^*}{a^4 r}\frac{\partial}{\partial r}\left[r\left(\frac{F_r}{r}\right)_r\right] \tag{6.21f}$$

Evaluation of the time derivative in (6.21a) is carried out as follows

$$\left(\frac{F_r}{r}\right)_t = \frac{\mathrm{d}r^{-1}}{\mathrm{d}t}F_r + \frac{1}{r}\frac{\mathrm{d}F_r}{\mathrm{d}t} \tag{6.22}$$

or

$$\begin{cases} \dfrac{\mathrm{d}r}{\mathrm{d}t} = \dfrac{\mathrm{d}(r^*/a(t))}{\mathrm{d}t} = -r^*\dfrac{\dot{a}}{a^2} = -\dfrac{\dot{a}}{a}r \\ \dfrac{\mathrm{d}}{\mathrm{d}t}\left(\dfrac{1}{r}\right) = \dfrac{\partial}{\partial r}\left(\dfrac{1}{r}\right)\dfrac{\mathrm{d}r}{\mathrm{d}t} + \underbrace{\dfrac{\partial}{\partial t}\left(\dfrac{1}{r}\right)}_{0} = \dfrac{\dot{a}}{ar} \\ \dfrac{\mathrm{d}F_r}{\mathrm{d}t} = \dfrac{\partial F_r}{\partial r}\dfrac{\mathrm{d}r}{\mathrm{d}t} + \dfrac{\partial F_r}{\partial t} = -\dfrac{\dot{a}}{a}rF_{rr} + F_{rt} \end{cases} \tag{6.23}$$

Upon substitution and collection of terms, we recover

$$\left\{-\frac{a^2}{\nu}\frac{F_{rt}}{r}+\frac{a\dot{a}}{\nu}r\left(\frac{F_r}{r}\right)_r+2\frac{a\dot{a}}{\nu}\frac{F_r}{r}+\frac{F}{r}\left(\frac{F_r}{r}\right)_r - \left(\frac{F_r}{r}\right)^2+\frac{1}{r}\left(\frac{F_r}{r}\right)_r\left(\frac{F_r}{r}\right)_{rr}\right\}_r=0 \tag{6.24}$$

If we let

$$\alpha(t)=\frac{a\dot{a}}{\nu} \tag{6.25}$$

then (6.24) becomes

$$\left\{\left(\frac{F_r}{r}\right)_{rr}+\left[\frac{1}{r}+\frac{F}{r}+\alpha r\right]\left(\frac{F_r}{r}\right)_r-\left(\frac{F_r}{r}-2\alpha\right)\frac{F_r}{r}-\frac{a^2}{\nu}\frac{F_{rt}}{r}\right\}_r=0 \tag{6.26}$$

or, by integrating with respect to r,

$$\left(\frac{F_r}{r}\right)_{rr}+\left[\frac{1}{r}+\frac{F}{r}+\alpha r\right]\left(\frac{F_r}{r}\right)_r-\left(\frac{F_r}{r}-2\alpha\right)\frac{F_r}{r}-\frac{a^2}{\nu}\frac{F_{rt}}{r}=K \tag{6.27}$$

This formidable ODE embodies the physics of the viscous flow in a porous pipe with regressing walls. It was first derived by Uchida and Aoki (1977) in the context of pipe flow with expanding or contracting walls. The only difference that the current derivation bears is in the boundary conditions. Goto and Uchida (1990) and Dauenhauer and Majdalani (1999) later extended Uchida's problem to allow injection of fluid at the wall (see also Dauenhauer and Majdalani 2003). They did this for both cylindrical and planar configurations. Majdalani and coworkers (Majdalani et al. 2002; Majdalani and Zhou 2003; Majdalani et al. 2009) subsequently derived asymptotic solutions for this problem for a wide range of Reynolds numbers.

6.2.4 Similarity in time

Equation (6.27) is obviously intractable using any of the standard analytical techniques. By utilizing a practical hypothesis however, Uchida and Aoki (1977)

and Goto and Uchida (1990) were able to reduce (6.27) to a third order nonlinear ODE. This may be accomplished by setting

$$\alpha(t) = \text{constant}; \quad F(r,t) \mapsto F[r, \alpha(t)] \tag{6.28}$$

this immediately implies that

$$F_{rt} = \frac{\partial F_r}{\partial \alpha}\frac{\mathrm{d}\alpha}{\mathrm{d}t} = 0 \tag{6.29}$$

One can then compute the required wall regression speed for which α becomes a constant. According to this model

$$\alpha = \frac{a\dot{a}}{\nu} = \frac{a_0\dot{a}_0}{\nu} \tag{6.30}$$

where a_0 and $\dot{a}_0$ correspond to the initial radius and regression speed, respectively. Upon integration, we get

$$a(t) = a_0\sqrt{1 + 2\frac{\nu\alpha}{a_0^2}t} \tag{6.31}$$

Note that Uchida's model does not dispatch of time dependence, it merely states that the regression speed is specified in such a way that $\alpha(t)$ remains a constant.

Before substituting the time similarity conditions into (6.27), we find it useful to introduce the following normalizations

$$F \mapsto \frac{F}{\mathrm{Re}}; \quad \eta \equiv \tfrac{1}{2}r^2 \tag{6.32}$$

where Re is the sidewall injection Reynolds number based on the absolute velocity of the fluid

$$\mathrm{Re} \equiv \frac{Ua}{\nu} = \frac{U_{\mathrm{w}}a}{\nu} - \alpha \tag{6.33}$$

In this setting, the Reynolds number is a function of time. To make further headway, we must assume that Re = constant, or

$$\frac{U_{\mathrm{w}}a}{\nu} = \text{constant} = \frac{U_{\mathrm{w}0}a_0}{\nu} \tag{6.34}$$

Then, one can extract the proper form for U_{w}

$$U_{\mathrm{w}} = \frac{U_{\mathrm{w}0}a_0}{a} = U_{\mathrm{w}0}\left(1 + 2\frac{\nu\alpha}{a_0^2}t\right)^{-\frac{1}{2}} \tag{6.35}$$

Finally, Backward substitution of (6.32) into (6.27) yields

$$\eta F''' + F'' + \tfrac{1}{2}\mathrm{Re}(FF'' - F'^2) + \alpha(\eta F'' + F') = K(\mathrm{Re}) \tag{6.36}$$

where primes denote differentiation with respect to η. To eliminate the constant $K(\mathrm{Re})$, one differentiates (6.36) with respect to η

$$\eta F'''' + \alpha(\eta F''' + 2F'') + \tfrac{1}{2}\mathrm{Re}(FF''' - F'F'') + 2F''' = 0 \tag{6.37}$$

Finally, the boundary conditions may be assimilated into the following set

$$\frac{dF(\frac{1}{2})}{d\eta} = 0 \tag{6.38a}$$

$$F(\tfrac{1}{2}) = 1 \tag{6.38b}$$

$$F(0) = 0 \tag{6.38c}$$

$$\lim_{\eta\to 0}\sqrt{2\eta}\frac{d^2F}{d\eta^2} = 0 \tag{6.38d}$$

Note that the constant $K(\mathrm{Re})$ may be specified by evaluating (6.36) at any location inside the domain such as the centerline $r = 0$. Based on the boundary conditions,

this gives

$$K(\mathrm{Re}) = F''(0) + \tfrac{1}{2}\mathrm{Re}F'^2(0) + \alpha F'(0) \tag{6.39}$$

Either of the differential equations given by (6.36) and (6.37) may be used to solve for the mean flow function $F(\eta)$. The choice depends on the type of solution sought. For example, we will use (6.36) for the numerical solution because it requires less memory storage and a minimum number of Runge–Kutta integrations. On the other hand, (6.37) is used to determine both the regular perturbation and ADM solutions because of the implicit nonlinearity that the constant $K(\mathrm{Re})$ embodies.

6.3 Numerical method

Being nonlinear ODEs, (6.36) and (6.37) may be solved directly through a Runge–Kutta integration routine. However, a close inspection of the boundary conditions as well as the governing equations reveals the following difficulties. Firstly, the explicit presence of η in either equation requires a careful treatment by virtue of the singularity at the origin. This matter may be settled through a Taylor series expansion near the centerline. Secondly, the boundary conditions given by (6.38) clearly indicate that we are dealing with a boundary value problem that requires a double infinity of integrations (see Terrill and Thomas 1969). While this problem may be overcome via a shooting method based on a Newton-Raphson root finding algorithm such as the one proposed by Dauenhauer and Majdalani (2003), the fourth boundary condition (6.38d) will complicate this procedure. The reason is that, as long as $F''(0)$ is finite, (6.38d) is always satisfied. Indeed, one expects $F''(0)$ to be finite as it corresponds to the vorticity at the centerline. The conclusion is that (6.38d) is practically useless for a numerical treatment.

These difficulties may be overcome if one uses a transformation similar to the one proposed by Terrill and Thomas (1969), but that incorporates the effect of α. By allowing both the Reynolds number Re and α to be determined a posteriori, i.e. at

the end of the integration, the shooting method will no longer be required and the numerical solution may be arrived at via a single Runge–Kutta integration. We start by introducing the following

$$F = \lambda G(\xi); \quad \xi = b\,\eta \tag{6.40}$$

where both λ and b are scaling factors that will be determined once the integration is complete. Upon substitution into (6.36) , we recover the following third order ODE in $G(\xi)$

$$\xi G''' + G'' + \tfrac{1}{2}\lambda \mathrm{Re}(GG'' - G'^2) + \frac{\alpha}{b}(\xi G'' + G') = \frac{K}{\lambda b^2} = K_1 \tag{6.41}$$

where the primes denote differentiation with respect to ξ. If we further set

$$\lambda = \frac{2}{\mathrm{Re}} \quad \text{and} \quad \beta = \frac{\alpha}{b} \tag{6.42}$$

equation (6.41) reduces to the following convenient form

$$\xi G''' + G'' + GG'' - G'^2 + \beta(\xi G'' + G') = K_1 \tag{6.43}$$

Finally, by applying this procedure to the boundary conditions (6.38), they transform to

$$\frac{dG(\frac{1}{2}b)}{d\xi} = 0 \tag{6.44a}$$

$$G(\tfrac{1}{2}b) = \frac{1}{\lambda} = \frac{\mathrm{Re}}{2} \tag{6.44b}$$

$$G(0) = 0 \tag{6.44c}$$

$$\lim_{\xi \to 0} \sqrt{\xi} \frac{d^2 G}{d\xi^2} = 0 \tag{6.44d}$$

By initializing the solution with arbitrary values for $G'(0)$, $G''(0)$, and β, the integration is carried out until $G'(\frac{1}{2}b) = 0$ from which one can extract the value of b.

Then, one can obtain the value of the Reynolds number from (6.44b) or $\mathrm{Re} = 2G(\frac{1}{2}b)$. Finally, the value of α is computed from knowledge of b and β. The constant K_1 is also evaluated from the initial guesses as follows

$$K_1 = G''(0) - G'(0)^2 + \beta G'(0) \tag{6.45}$$

Finally, near centerline ($\xi \to 0$), a Taylor series expansion of the governing equation is required. Let

$$G(\xi) = \sum \gamma_i \xi^i \tag{6.46}$$

Given this form, we have

$$\gamma_0 = G(0) = 0; \quad \gamma_1 = G'(0); \quad \gamma_2 = \tfrac{1}{2}G''(0) \tag{6.47}$$

Note that these coefficients are known since the values of the first and second derivatives at the centerline are used to seed the numerical solution. Then, by substituting (6.46) into the governing equation (6.36), coefficients of the same order are equated to recover the following recurrence formula

$$\begin{aligned}(n+2)(n+1)^2\gamma_{n+2} = &\sum_{j=0}^{n}(j+1)(n-j+1)\gamma_{j+1}\gamma_{n-j+1} - \sum_{j=0}^{n}(j+1)(j+2)\gamma_{j+2}\gamma_{n-j} \\ &- \beta(n+1)^2\gamma_{n+1}; \quad n \geq 1\end{aligned} \tag{6.48}$$

Algorithm 6.4.1 lists the necessary steps for our numerical implementation. Results of the numerical simulation will be presented in subsequent chapters where they will be compared to the analytical solutions.

6.4 Summary

In this chapter, we derive the equations governing the motion of an incompressible viscous fluid in a porous pipe with regressing walls. By assuming that the axial

velocity varies linearly in the axial direction, an assumption based on Berman's original work (Berman 1953), we are able to reduce the Navier-Stokes equations to a partial differential equation in r and t. Then, by confining the walls to move in a specified manner, time similarity will further reduce the governing equation to a single nonlinear ODE. This equation is presented in two flavors; a third order equation with an undetermined constant and a fourth order equation. Finally, a strategy for the numerical solution of this problem is discussed based on a scaling transformation of both the dependent and independent variables. The subsequent chapters will focus on the solution of this problem using a two analytical tools. Because the physical behavior of this problem has been explored by many scholars, the focus hereafter will be on the analytical solutions rather than the behavior of the flowfield.

Algorithm 6.4.1: RK4INTEGRATE()

allocate memory for arrays

process user input: $G(0)$, $G'(0)$, $G''(0)$, β, $n_{\max}$, n_{Taylor}, $\xi_{\max}$

calculate K_1

calculate Taylor series coefficients γ_i

for $i \leftarrow 0$ **to** n_{Taylor}

  do calculate $G(\xi)$ near the centerline

for $i \leftarrow n_{\text{Taylor}}$ **to** $n_{\max}$

  do integrate governing equation

for $i \leftarrow 0$ **to** $n_{\max}$

  do find $n_p \setminus G'(n_p) = 0$

calculate ξ_p that corresponds to n_p

$\xi_{\max} \leftarrow \xi_p + \epsilon$

for $i \leftarrow n_{\text{Taylor}}$ **to** $n_{\max}$

  do integrate governing equation using

for $i \leftarrow 0$ **to** $n_{\max}$

  do find $n_p \setminus G'(n_p) = 0$

calculate ξ_p that corresponds to n_p

$b \leftarrow 2\xi_p$

$\alpha \leftarrow b\beta$

$\text{Re} \leftarrow 2G(n_p)$

Here, $\xi_{\max}$ is the interval size (starting from zero), $n_{\max}$ is the number of points that divides the interval, and n_{Taylor} is the number of points for which the Taylor series expansion is to be applied. Note that n_p corresponds to the point where $G'(n_p) = 0$ and ϵ is arbitrary small number. All subscripts with p correspond to that point.

Chapter 7

Asymptotic Treatment via Perturbation

In this chapter, we use a regular perturbation expansion to solve the differential equation that was derived in Chapter 6. We focus on the cases of large injection Reynolds number with arbitrary wall permeability α as well as small injection or suction with weak permeability.

7.1 Introduction

In the previous chapter, we reduced the Navier-Stokes equations for the viscous flow in a porous cylinder with regressing walls to a nonlinear ODE by using a similarity transformation in time and space. To recapitulate, the ODE is given by

$$\eta F'''' + \alpha(\eta F''' + 2F'') + \tfrac{1}{2}\mathrm{Re}(FF''' - F'F'') + 2F''' = 0 \tag{7.1}$$

with the following set of boundary conditions

$$\frac{dF(\frac{1}{2})}{d\eta} = 0 \tag{7.2a}$$

$$F(\tfrac{1}{2}) = 1 \tag{7.2b}$$

$$F(0) = 0 \tag{7.2c}$$

$$\lim_{\eta\to 0} \sqrt{2\eta}\frac{d^2F}{d\eta^2} = 0 \tag{7.2d}$$

In this chapter, we solve (7.1) by using a regular perturbation expansion. We consider the cases of large injection (Re $>>$ 1) and small injection/suction with weak permeability ($|\mathrm{Re}| = O(1)$, $|\alpha| = O(1)$).

7.2 Large injection

In this case, the Reynolds number is a large positive number and a regular perturbation in the inverse of the Reynolds number is appropriate. We follow Majdalani et al. (2002) and write

$$F = F_0 + \varepsilon F_1 + O(\varepsilon^2); \quad \varepsilon \equiv \frac{1}{\mathrm{Re}} \tag{7.3}$$

upon substitution into (7.1), we recover the ODEs governing the leading and first order solutions. These are

$$O(0): \quad F_0F_0''' - F_0'F_0'' = 0 \tag{7.4a}$$

$$O(1): \quad F_0F_1''' + F_1F_0''' - F_0'F_1'' - F_1'F_0'' + 2\eta F_0'''' + (2\alpha\eta + 4)F_0''' + 4\alpha F_0'' = 0 \tag{7.4b}$$

Note that we will limit our analysis to obtaining the leading and first order solutions partly due to the excellent agreement of the present solution with the numerical simulations.

7.2.1 Leading order solution

At leading order, we have

$$F_0 F_0''' - F_0' F_0'' = 0 \tag{7.5}$$

This can be solved by inspection to obtain

$$F_0 = \sin(\pi\eta) = \sin\vartheta; \quad \vartheta = \pi\eta \tag{7.6}$$

Equation (7.6) identically recovers Taylor–Culick's model (Culick 1966).

7.2.2 First order solution

By substituting (7.6) into (7.4b), we obtain the ODE governing the first order term

$$\begin{aligned}\sin\vartheta F_1''' - \cos\vartheta F_1 - \cos\vartheta F_1'' + \sin\vartheta F_1' = \\ -2\vartheta\sin\vartheta + (2\pi^{-1}\alpha\vartheta + 4)\cos\vartheta + 4\pi^{-1}\alpha\sin\vartheta\end{aligned} \tag{7.7}$$

The solution of (7.7) requires the identification of a homogeneous solution. This can be obtained by solving

$$\sin\vartheta F_{1h}''' - \cos\vartheta F_{1h} - \cos\vartheta F_{1h}'' + \sin\vartheta F_{1h}' = 0 \tag{7.8}$$

for which a particular solution is found to be

$$F_{1h} = C\cos\vartheta \tag{7.9}$$

To determine a more general homogeneous solution, we allow the constant in (7.9) to be a function of ϑ by setting

$$F_{1h} = C(\vartheta)\cos\vartheta \tag{7.10}$$

Upon substitution of (7.10) into (7.8), one obtains the differential equation governing $C(\vartheta)$

$$C''' \sin\vartheta \cos\vartheta - 2C'' \sin^2\vartheta - C'' = 0 \tag{7.11}$$

The solution of (7.11) may be obtained through division by $C'' \sin\vartheta \cos\vartheta$ and then by immediate integration. This operation gives

$$C(\vartheta) = \tfrac{1}{2} K_0 \tan\vartheta + K_1 \vartheta + K_2 \tag{7.12}$$

Finally, the general homogeneous solution of (7.8) is at hand

$$F_{1h} = C(\vartheta)\cos\vartheta = K_0 \sin\vartheta + K_1 \vartheta \cos\vartheta + K_2 \cos\vartheta \tag{7.13}$$

To obtain the total solution of (7.7), we use variation of parameters and write

$$F_1 = K_0(\vartheta)\sin\vartheta + K_1(\vartheta)\vartheta\cos\vartheta + K_2(\vartheta)\cos\vartheta \tag{7.14}$$

then, upon differentiation, we obtain

$$F_1' = K_0\cos\vartheta + K_1(\cos\vartheta - \vartheta\sin\vartheta) - K_2\sin\vartheta \tag{7.15a}$$

$$F_1'' = -K_0\sin\vartheta + K_1(-2\sin\vartheta - \vartheta\cos\vartheta) - K_2\cos\vartheta \tag{7.15b}$$

$$F_1''' = -2K_1'\sin\vartheta - K_0\cos\vartheta + K_1(-2\cos\vartheta - \cos\vartheta + \vartheta\sin\vartheta) + K_2\sin\vartheta \tag{7.15c}$$

along with the auxiliary conditions

$$K_0'\sin\vartheta + K_1'\vartheta\cos\vartheta + K_2'\cos\vartheta = 0 \tag{7.16a}$$

$$K_0'\cos\vartheta + K_1'(\cos\vartheta - \vartheta\sin\vartheta) - K_2'\sin\vartheta = 0 \tag{7.16b}$$

By using (7.15) in the governing equation (7.7), we recover

$$-2K_1'\sin^2\vartheta = (2\pi^{-1}\alpha\vartheta + 4)\cos\vartheta + 4\pi^{-1}\alpha\sin\vartheta - 2\vartheta\sin\vartheta \tag{7.17}$$

It is convenient to divide the above equation by $\sin\vartheta$ so that

$$-2K_1'\sin\vartheta = (2\pi^{-1}\alpha\vartheta + 4)\cot\vartheta + 4\pi^{-1}\alpha - 2\vartheta \tag{7.18}$$

Then, one solves (7.16) in conjunction with (7.18) simultaneously for K_0', K_1', and K_2'. The resulting system is conveniently written in matrix form

$$\begin{bmatrix} \sin\vartheta & \vartheta\cos\vartheta & \cos\vartheta \\ \cos\vartheta & \cos\vartheta - \vartheta\sin\vartheta & -\sin\vartheta \\ 0 & -2\sin\vartheta & 0 \end{bmatrix} \begin{bmatrix} K_0' \\ K_1' \\ K_2' \end{bmatrix} = \begin{bmatrix} 0 \\ 0 \\ (\frac{2}{\pi}\alpha\vartheta + 4)\cot\vartheta + \frac{4}{\pi}\alpha - 2\vartheta \end{bmatrix} \tag{7.19}$$

Upon inversion, one recovers the differential equations for K_0', K_1', and K_2'

$$K_0' = -\vartheta\cos\vartheta\cot\vartheta + \frac{2}{\pi}\alpha\cos\vartheta\cot\vartheta + 2\cos\vartheta\cot^2\vartheta + \frac{\alpha}{\pi}\vartheta\cos\vartheta\cot^2\vartheta \tag{7.20}$$

$$K_1' = \vartheta\csc\vartheta - \frac{2}{\pi}\alpha\csc\vartheta - 2\cot\vartheta\csc\vartheta - \frac{\alpha}{\pi}\vartheta\cot\vartheta\csc\vartheta \tag{7.21}$$

$$\begin{aligned} K_2' = -\frac{2}{\pi}\alpha\cos\vartheta + \frac{2}{\pi}\alpha\vartheta\csc\vartheta + \vartheta\cos\vartheta - \vartheta^2\csc\vartheta - 2\cot\vartheta\cos\vartheta \\ +2\vartheta\cot\vartheta\csc\vartheta - \frac{\alpha}{\pi}\vartheta\cos\vartheta\cot\vartheta + \frac{\alpha}{\pi}\vartheta^2\cot\vartheta\csc\vartheta \end{aligned} \tag{7.22}$$

By integrating the previous set of equations we obtain the following expressions

$$\begin{aligned} K_0 = \frac{\alpha}{\pi}\left(\cos\vartheta + 3\ln\tan\tfrac{1}{2}\vartheta - \vartheta\sin\vartheta - \vartheta\csc\vartheta\right) - \vartheta\cos\vartheta - \sin\vartheta \\ - 2\csc\vartheta - S(\vartheta) + C_0 \end{aligned} \tag{7.23}$$

$$K_1 = \frac{\alpha}{\pi}\left(\vartheta\csc\vartheta - 3\ln\tan\tfrac{1}{2}\vartheta\right) + 2\csc\vartheta + S(\vartheta) + C_1 \tag{7.24}$$

$$K_2 = \frac{\alpha}{\pi}\left[3S(\vartheta) - \sin\vartheta - \vartheta^2\csc\vartheta - \vartheta\cos\vartheta\right] - \cos\vartheta + \vartheta\sin\vartheta - 2\vartheta\csc\vartheta - J(\vartheta) + C_2 \tag{7.25}$$

where

$$S(\vartheta) = \int_0^{\vartheta} \phi \csc\phi d\phi; \quad J(\vartheta) = \int_0^{\vartheta} \phi^2 \csc\phi d\phi \tag{7.26}$$

and C_0, C_1, and C_2 are constants that can be determined by invoking the boundary conditions (7.2). The first order solution (7.14) is now at hand

$$\begin{aligned} F_1 =& \frac{\alpha}{\pi}\left[3\ln\tan\tfrac{1}{2}\vartheta(\sin\vartheta - \vartheta\cos\vartheta) - 2\vartheta\right] + \frac{3}{\pi}\alpha\cos\vartheta S(\vartheta) - 3 - J(\vartheta)\cos\vartheta \\ &+ (\vartheta\cos\vartheta - \sin\vartheta)S(\vartheta) + C_0\sin\vartheta + C_1\vartheta\cos\vartheta + C_2\cos\vartheta \end{aligned} \tag{7.27}$$

Application of the boundary conditions requires that

$$F_1(\tfrac{1}{2}\pi) = 0; \quad \text{or} \quad C_0 = 3 + \alpha + S(\tfrac{1}{2}\pi) \tag{7.28}$$

in conjunction with

$$\lim_{\vartheta\to 0} F_1(\vartheta) = 0; \quad \text{or} \quad C_2 = 3 \tag{7.29}$$

and finally

$$\frac{\mathrm{d}F_1}{\mathrm{d}\eta}\left(\frac{1}{2}\right) = \pi\frac{\mathrm{d}F_1}{\mathrm{d}\vartheta}\left(\tfrac{1}{2}\pi\right) = 0 \tag{7.30}$$

from which we extract

$$C_1 = -1 - \frac{6}{\pi} + \frac{2}{\pi^2}\alpha + \frac{2}{\pi}J(\tfrac{1}{2}\pi) - S(\tfrac{1}{2}\pi)\left(\frac{6}{\pi^2}\alpha + 1\right) \tag{7.31}$$

7.2.3 Verification

The total solution is now at hand and is given by

$$\begin{aligned} F =& F_0 + \varepsilon F_1 + \mathcal{O}(\varepsilon^2) = \sin\vartheta + \varepsilon\left\{\frac{\alpha}{\pi}\left[3\ln\tan\tfrac{1}{2}\vartheta(\sin\vartheta - \vartheta\cos\vartheta) - 2\vartheta\right]\right. \\ &+ \frac{3}{\pi}\alpha\cos\vartheta S(\vartheta) - 3 - J(\vartheta)\cos\vartheta + (\vartheta\cos\vartheta - \sin\vartheta)S(\vartheta) \\ &\left. + C_0\sin\vartheta + C_1\vartheta\cos\vartheta + C_2\cos\vartheta\right\} \end{aligned} \tag{7.32}$$

This result is identical to the one obtained by Majdalani et al. (2002) (see Majdalani et al. 2009, for correct form). Equation (7.32) is compared to results from the Runge–Kutta integration for Reynolds numbers of 100, 500, and 1000 held at different values of the wall permeability, namely $\alpha = 10$, 20, -10, and -20. Starting with the mean flow function F, corresponding graphs are shown in Figures 7.1–7.2. The first noticeable feature is the accuracy of the solution for large Re regardless of the wall permeability. In fact, even for the relatively small value of $\mathrm{Re} = 100$, the curves are indistinguishable unless one uses magnification on certain areas of the graphs. The other noteworthy feature is the effect of decreasing the wall permeability number. Specifically, the curves become increasingly identical if one scans the graphs starting with the largest value of α in Figure 7.1b through Figure 7.2b.

The second set of comparisons is shown in Figures 7.3–7.4 for F'. The derivative of the mean flow function is directly connected to the axial velocity and hence the importance of arriving at a reliable analytical representation for $F'(\eta)$. By looking at the comparison in this case, similar trends are observed as those corresponding to F. The most prominent feature in these graphs is the effect of α on the centerline velocity. As the wall permeability is decreased so does the centerline velocity. Altogether, the curves are practically inseparable, a satisfactory observation given that our solution is of first order accuracy.

7.3 Small injection/suction with weak permeability

In this case, both the Reynolds number and the permeability are small. This necessitates rewriting (7.1) as

$$2\eta F'''' + \alpha(2\eta F''' + 4F'') + \mathrm{Re}(FF''' - F'F'') + 4F''' = 0 \tag{7.33}$$

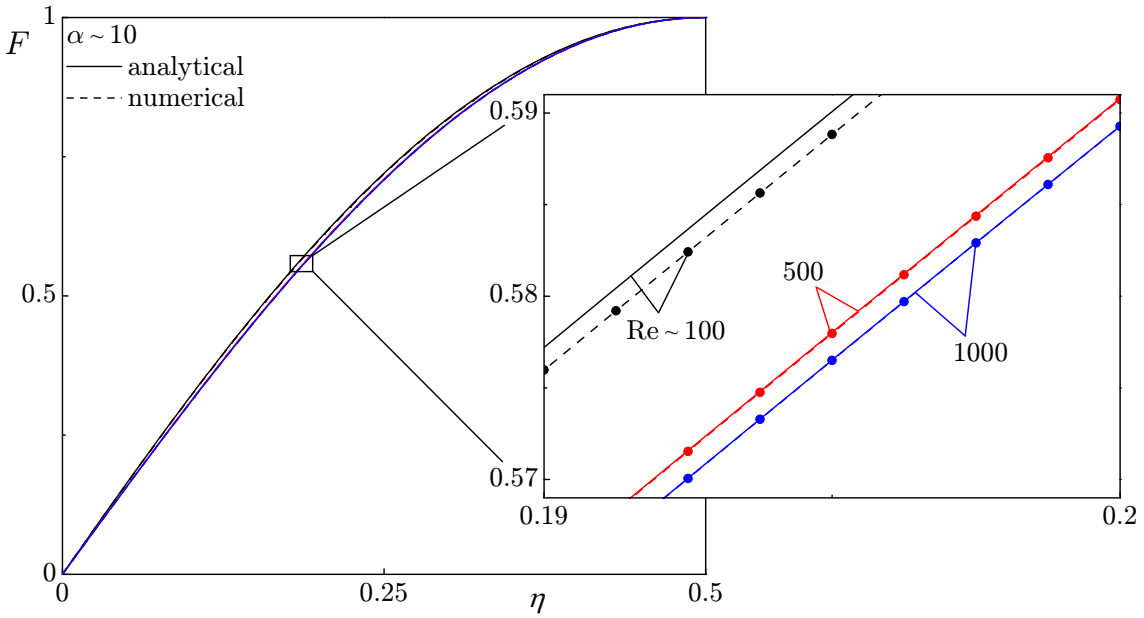

(a) $\alpha \sim 10$

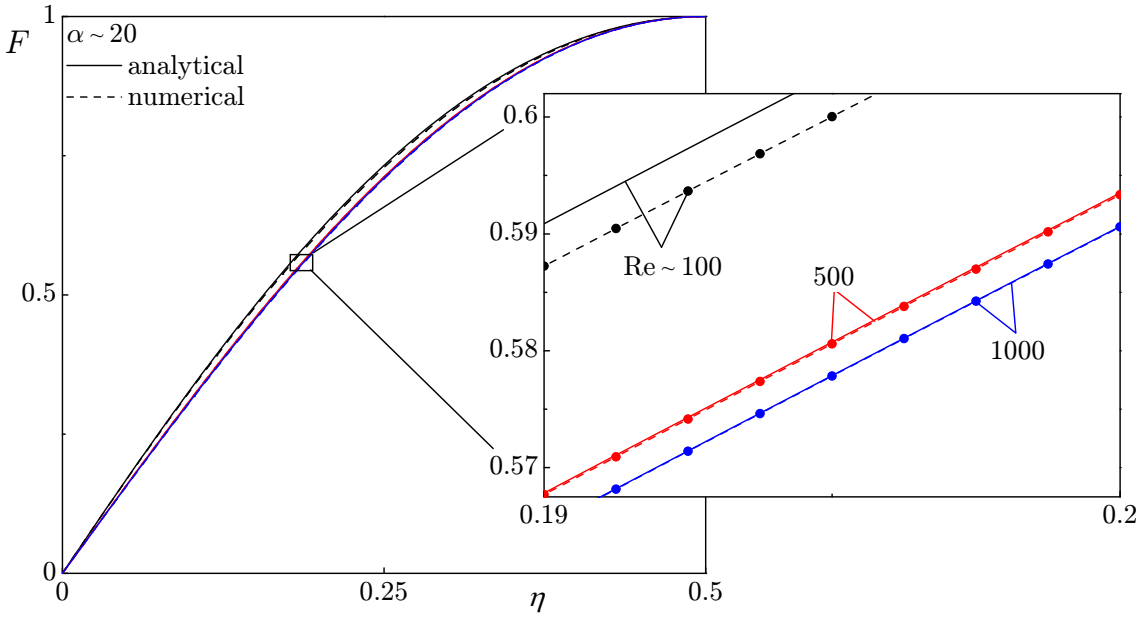

(b) $\alpha \sim 20$

Figure 7.1: Comparison between analytical (—) and numerical solutions (○) for the mean flow function F using (a) $\alpha \sim 10$, and (b) $\alpha \sim 20$. Curves are shown for Re $\sim$ 100, 500, and 1000.

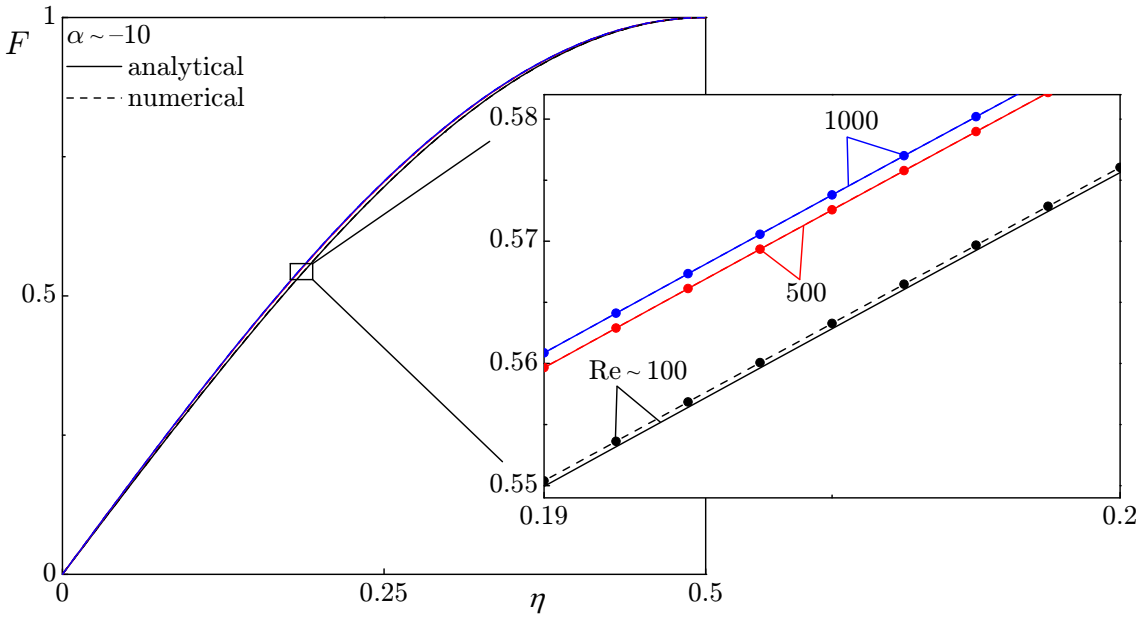

(a) $\alpha \sim -10$

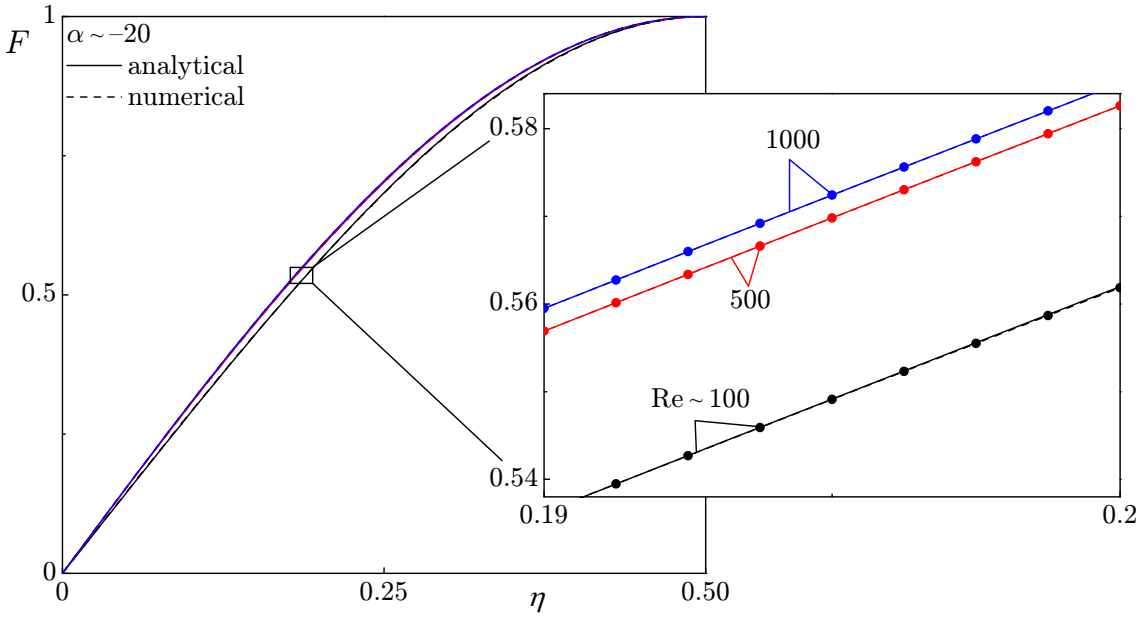

(b) $\alpha \sim -20$

Figure 7.2: Comparison between analytical (—) and numerical solutions (∘) for the mean flow function F using (a) $\alpha \sim -10$, and (b) $\alpha \sim -20$. Curves are shown for Re $\sim$ 100, 500, and 1000.

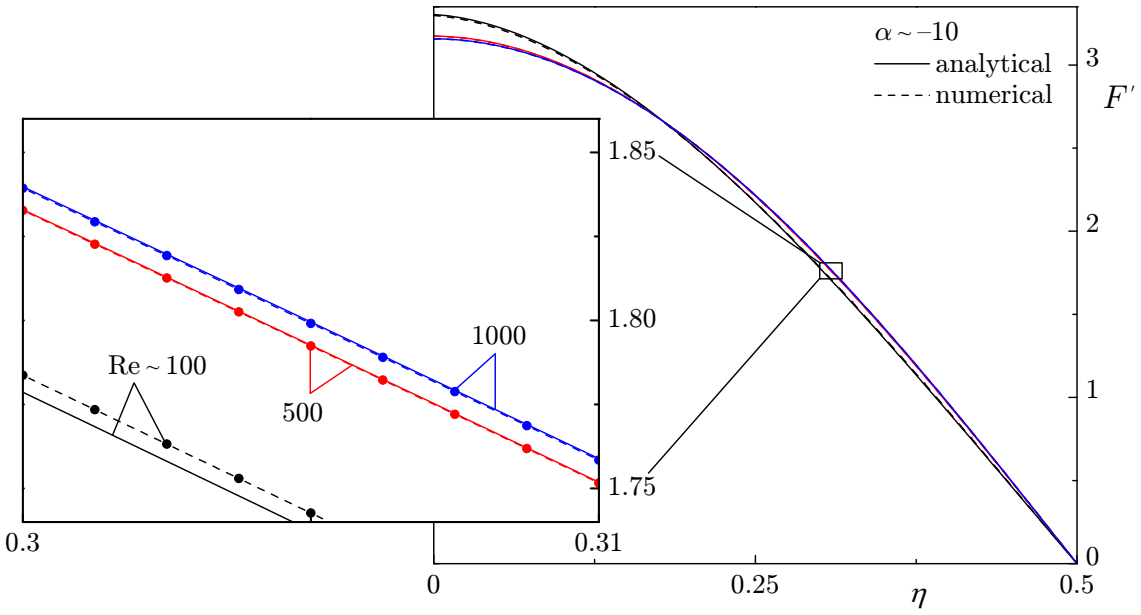

(a) $\alpha \sim 10$

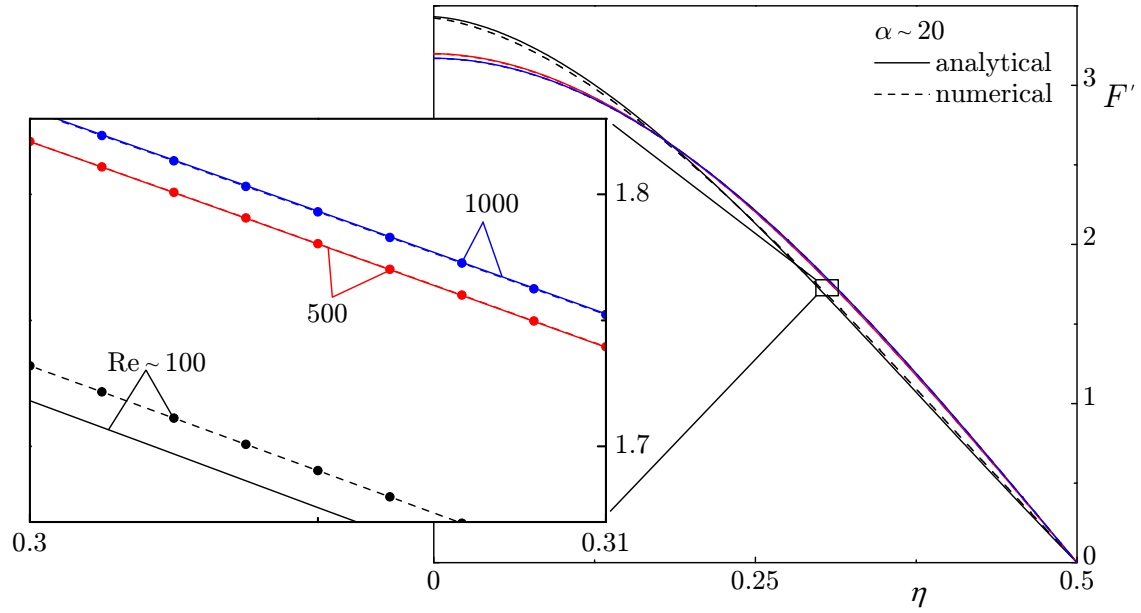

(b) $\alpha \sim 10$

Figure 7.3: Comparison between analytical (—) and numerical solutions (∘) for F' using (a) $\alpha \sim 10$, and (b) $\alpha \sim 20$. Curves are shown for Re $\sim$ 100, 500, and 1000.

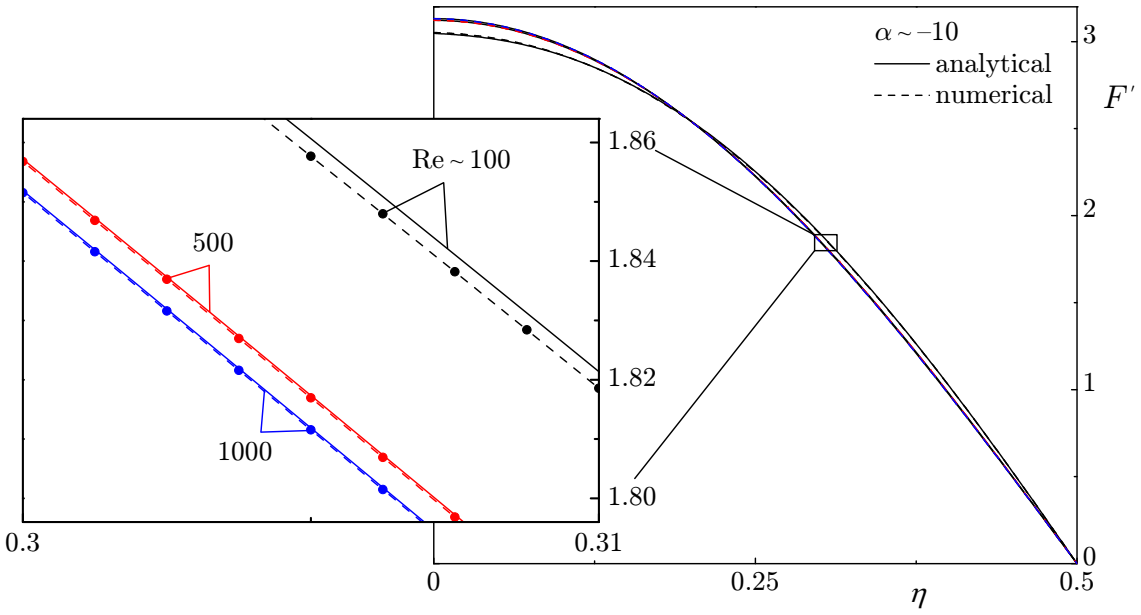

(a) $\alpha \sim -10$

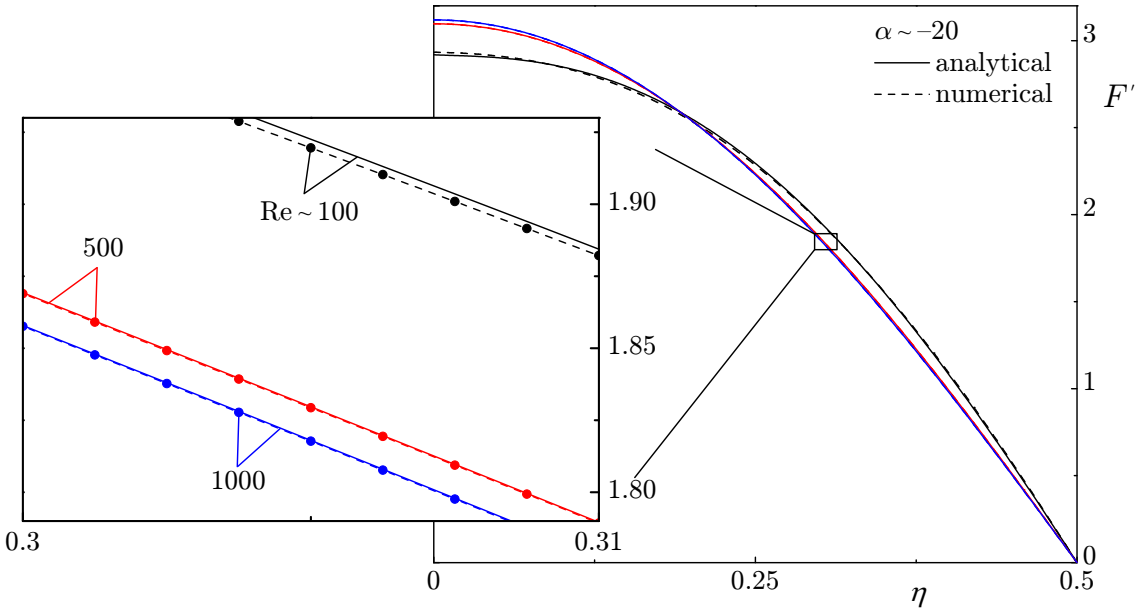

(b) $\alpha \sim -20$

Figure 7.4: Comparison between analytical (—) and numerical solutions (∘) for F' using (a) $\alpha \sim -10$, and (b) $\alpha \sim -20$. Curves are shown for Re $\sim$ 100, 500, and 1000.

To solve (7.33) using a perturbation expansion, one needs to expand in both small parameters, i.e. Re and α. In other words,

$$F = F_0 + \mathrm{Re} F_1 + O(\mathrm{Re}^2) \tag{7.34}$$

$$F_0 = F_{00} + \alpha F_{01} + O(\alpha^2) \tag{7.35}$$

$$F_1 = F_{10} + \alpha F_{11} + O(\alpha^2) \tag{7.36}$$

7.3.1 Leading order solution

At leading order in Re (i.e. $\mathrm{Re} = 0$), we have

$$2\eta F_0'''' + \alpha(2\eta F_0''' + 4F_0'') + 4F_0''' = 0 \tag{7.37}$$

but

$$F_0 = F_{00} + \alpha F_{01} + O(\alpha^2) \tag{7.38}$$

then, the leading and first order equations in α are

$$O(0): \quad \eta F_{00}'''' + 2F_{00}''' = 0 \tag{7.39a}$$

$$O(\alpha): \quad \eta F_{01}'''' + 2F_{01}''' = -\eta F_{00}''' - 2F_{00}'' \tag{7.39b}$$

The solution of (7.39a) along with the boundary conditions (7.2) is

$$F_{00} = -4\eta^2 + 4\eta \tag{7.40}$$

with F_{00} known, (7.39b) becomes

$$\eta F_{01}'''' + 2F_{01}''' = 16 \tag{7.41}$$

Since the boundary conditions are picked up by F_{00}, then, for all other orders, the boundary conditions are null, i.e.

$$\begin{cases} F'_{0i}(\frac{1}{2}) = 0; \quad F_{0i}(\frac{1}{2}) = 0 \\ F_{0i}(0) = 0; \quad \lim_{\eta\to 0} \sqrt{2\eta} F''_{0i}(\eta) = 0 \end{cases}; \quad i = 1, 2, 3 \cdots \tag{7.42}$$

Then, the solution of (7.41) is

$$F_{01} = \tfrac{1}{3}(4\eta^3 - 4\eta^2 + \eta) \tag{7.43}$$

Finally, the leading order solution becomes

$$F_0 = F_{00} + \alpha F_{01} = -4\eta^2 + 4\eta + \tfrac{1}{3}\alpha\left(4\eta^3 - 4\eta^2 + \eta\right) \tag{7.44}$$

7.3.2 First order solution

At first order in Re we have

$$2\eta F_1'''' + \alpha(2\eta F_1''' + 4F_1'') + 4F_1''' = F_0' F_0'' - F_0 F_0''' \tag{7.45}$$

then, the leading and first order equations in α are

$$O(0): \quad \eta F_{10}'''' + 2F_{10}''' = 32\eta - 16 \tag{7.46a}$$

$$O(\alpha): \quad \eta F_{11}'''' + 2F_{11}''' = -\eta F_{10}''' - 2F_{10}'' + \tfrac{4}{9}(-72\eta^2 + 48\eta - 15) \tag{7.46b}$$

The solutions are

$$F_{10} = \tfrac{1}{9}(4\eta^4 - 12\eta^3 + 9\eta^2 - 2\eta) \tag{7.47}$$

and

$$F_{11} = \tfrac{1}{9}\left(-2\eta^5 + \tfrac{17}{3}\eta^4 - 8\eta^3 + \tfrac{19}{4}\eta^2 - \tfrac{23}{24}\eta\right) \tag{7.48}$$

The first order solution is therefore

$$F_1 = \tfrac{1}{9}(4\eta^4 - 4\eta^3 + \eta^2 - 2\eta) + \tfrac{1}{9}\alpha\left(-2\eta^5 + \tfrac{17}{3}\eta^4 - 8\eta^3 + \tfrac{19}{4}\eta^2 - \tfrac{23}{24}\eta\right) \tag{7.49}$$

7.3.3 Verification

The total solution is

$$\begin{aligned} F = &- 4\eta(\eta - 1) + \tfrac{1}{3}\alpha\,\eta\left(4\eta^2 - 4\eta + 1\right) + \tfrac{1}{9}\mathrm{Re}\,\eta(4\eta^3 - 12\eta^2 + 9\eta - 2) \\ &+ \tfrac{1}{9}\mathrm{Re}\,\alpha\,\eta\left(-2\eta^4 + \tfrac{17}{3}\eta^3 - 8\eta^2 + \tfrac{19}{4}\eta - \tfrac{23}{24}\right) \end{aligned} \tag{7.50}$$

Comparisons with numerical solutions are presented in Figures 7.5–7.6 for $\mathrm{Re} = 1$ and $\mathrm{Re} = -1$ held at representative values of $\alpha = -1$, -0.5, 0.5, and 1. In general, the curves corresponding to both analytical and numerical results are seen to exhibit very good agreement. It is also evident that the agreement depreciates with decreasing values of the Reynolds number as well as increasing values of the wall permeability. Larger values of the Reynolds number will not be appropriate for comparison because of the nature of the perturbation expansion that was based on small values of Re.

7.4 Summary

In this chapter, we present an asymptotic solution for the viscous flow in a porous pipe with regressing walls. The method is based on a regular perturbation expansion for two specific cases, namely, large injection ($\mathrm{Re} \to \infty$) and small injection or suction with weak permeability. The results are then compared with numerical simulations held at representative values of the Reynolds number and wall permeability. We find that in the majority of cases the asymptotic expansions and the numerical solutions are in very good agreement to the extent of indistinguishable visual differences in some cases.

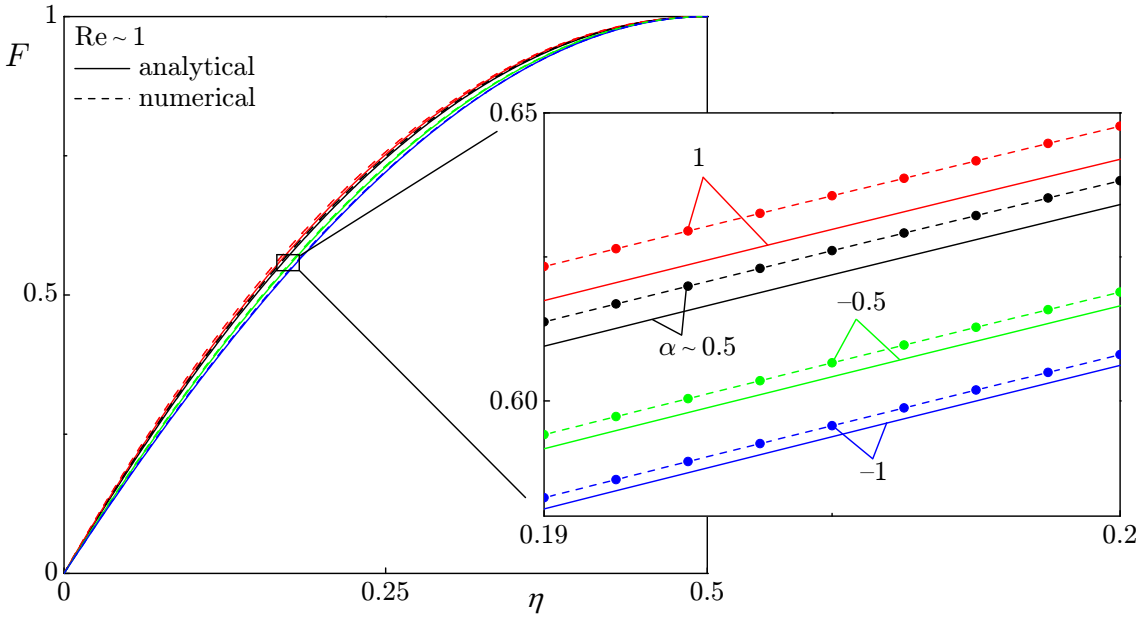

(a) Re ~ 1

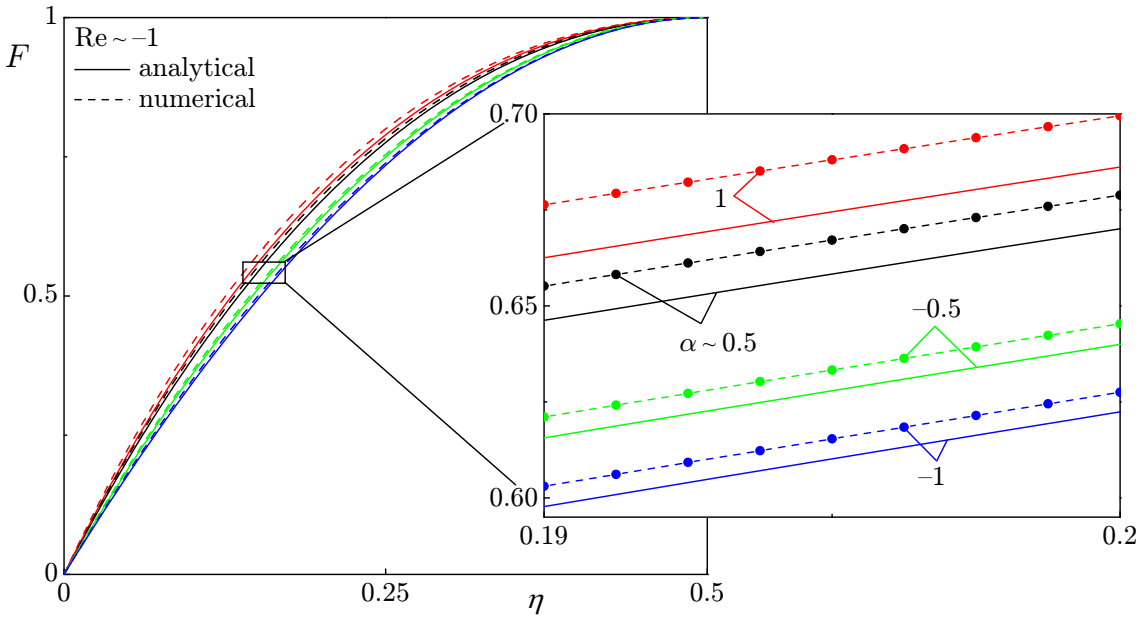

(b) Re ~ -1

Figure 7.5: Comparison between analytical (—) and numerical solutions (∘) for F using (a) Re ~ 1, and (b) Re ~ -1. Curves are shown for $\alpha \sim 0.5$, 1, -0.5, and -1.

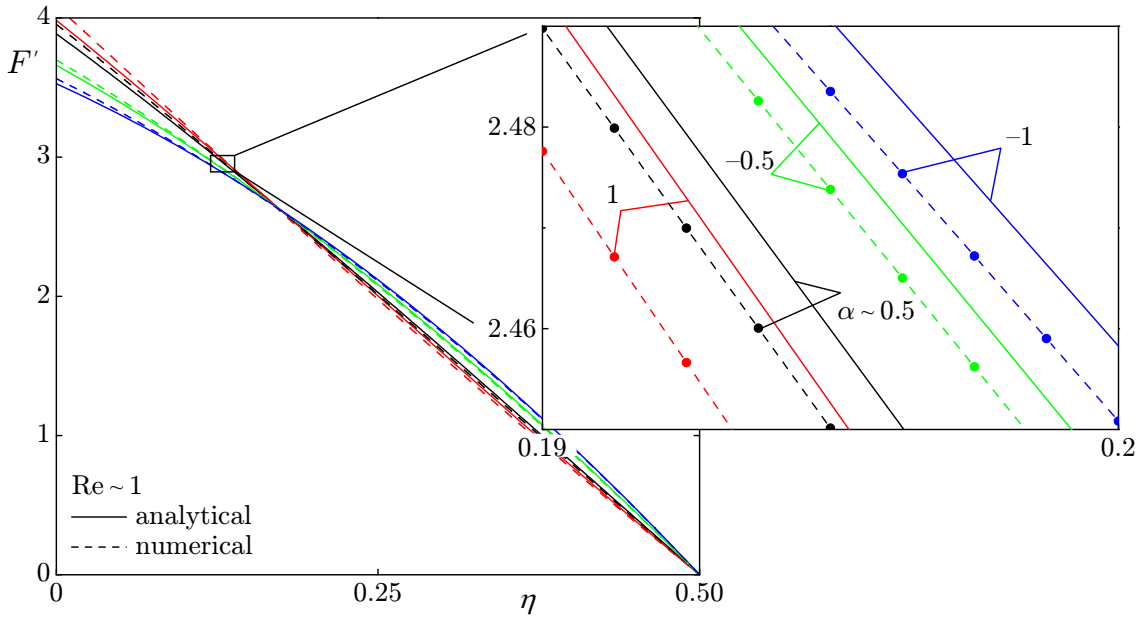

(a) Re ∼ 1

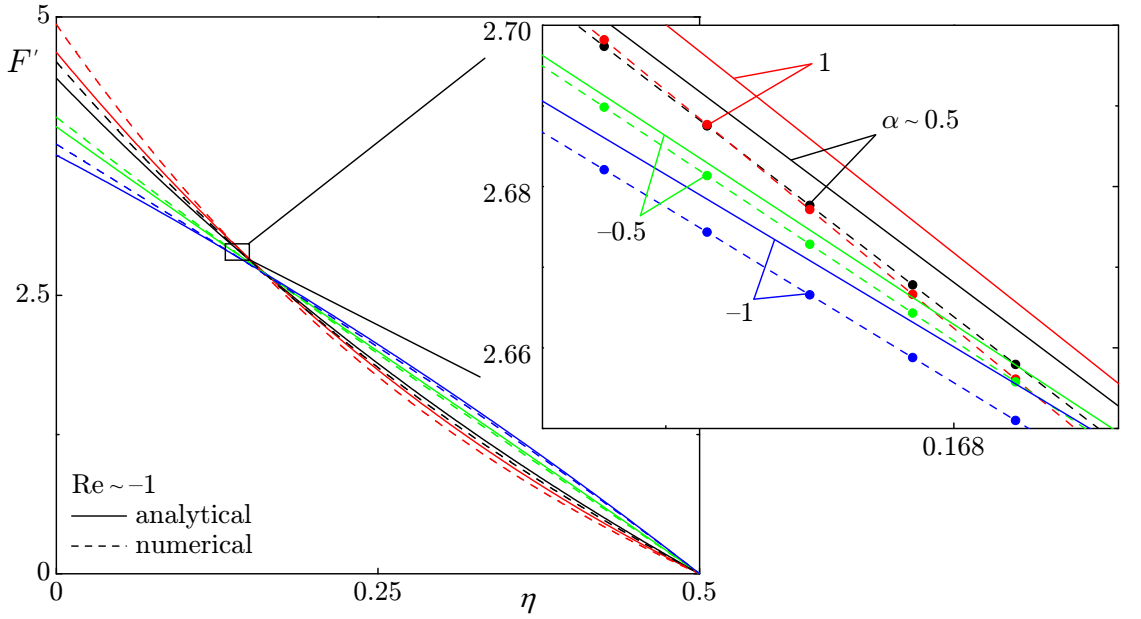

(b) Re ∼ −1

Figure 7.6: Comparison between analytical (—) and numerical solutions (∘) for F' using (a) Re ∼ 1, and (b) Re ∼ −1. Curves are shown for $\alpha \sim 0.5$, 1, −0.5, and −1.

Chapter 8

Adomian Decomposition Method

The Adomian Decomposition Method is a powerful technique for the solution of nonlinear equations. It is based on the idea of splitting a differential equation into a sum of linear and nonlinear operators and then expanding the nonlinear operator as a Taylor series around an initial solution. In this chapter we apply this method to the problem of the viscous flow in a porous cylinder with regressing walls. In the process we review the decomposition method and present it in a systematic manner that is easy to implement.

8.1 Introduction

First proposed by Adomian (1984), the decomposition method seeks to address the problem of handling nonlinearities arising in the modeling of physical systems (see also Adomian 1988). According to Adomian (1994), our analysis of real systems is severely hindered by our limitation to solve simple equations. In rare cases, nonlinear transformations convert the governing differential equations into linear equivalents where superposition and other known methods can be used to obtain an exact solution. However, the majority of practical situations offer no viable route for simplification or analytical modeling. The purpose of the decomposition method is to provide an avenue for handling the nonlinearities in differential equations by way

of a specific linearization that later came to be known as the Adomian polynomials (Rach 1984; Adomian and Rach 1992, 1996; Adomian 1997).

8.2 Overview of the decomposition method

In this overview, we will only restrict our attention to non-stochastic differential equations. These may be chaotic, only the boundary conditions and coefficients are deterministic. Then, a general form for such a differential equation is written in terms of an operator $\mathscr{F}$ as

$$\mathscr{F}y = g(t) \tag{8.1}$$

where y is the dependent variable, t is the independent variable, and $g(t)$ is a source term or forcing function. For example, one may consider Ueda's oscillator to illustrate the implementation of the decomposition method. This harmonic system is given by

$$y'' + ky' + y^3 = b\cos t \tag{8.2}$$

Using the nomenclature presented above, we have

$$\mathscr{F}y = y'' + ky' + y^3; \quad g(t) = b\cos t \tag{8.3}$$

8.2.1 Operator splitting

In the majority of cases, $\mathscr{F}$ is a combination of linear and nonlinear terms. If we choose $\mathscr{L}$ and $\mathscr{N}$ to denote the linear and nonlinear terms, respectively, we can then split $\mathscr{F}$ as follows

$$\mathscr{F}y = \mathscr{L}y + \mathscr{N}y = g(t) \tag{8.4}$$

For example, given Ueda's oscillator (8.2), we have

$$\mathscr{L}y = y'' + ky'; \quad \mathscr{N}y = y^3 \tag{8.5}$$

By examining (8.4), we write

$$\mathcal{L}y = g(t) - \mathcal{N}y \tag{8.6}$$

Then, the solution of the previous equation is generally written as

$$\mathcal{L}^{-1}\mathcal{L}y = \mathcal{L}^{-1}g - \mathcal{L}^{-1}\mathcal{N}y \tag{8.7}$$

Here, we make two observations. First, the nonlinear terms in (8.7) represent a fundamental difficulty in inverting it. Handling $\mathcal{N}y$ will be the subject of the remainder of this discussion. For now, if we assume that $\mathcal{N}y$ can be inverted somehow, the second observation is related to the choice of an easy to implement $\mathcal{L}^{-1}$. In other words, the selection of $\mathcal{L}$ is at the heart of the success of the decomposition method. One straightforward procedure consists of choosing the highest ordered derivative in $\mathscr{F}$ as the linear operator. The left over linear terms can be either cast into a remainder linera operator $\mathscr{R}$. This can be written as

$$\mathcal{L}y \to \mathscr{L}y + \mathscr{R}y \tag{8.8}$$

so that

$$\mathscr{L}y = g(t) - \mathscr{R}y - \mathcal{N}y \tag{8.9}$$

For instance, for Ueda's oscillator, we now have

$$\mathscr{L}y = y''; \quad \mathscr{R}y = ky'; \quad \mathcal{N}y = y^3 \tag{8.10}$$

In this case, the inverse operator consists of a two-fold integration.

8.2.2 Selection of the linear operator

In general, the linear operator corresponds to an m^{th} derivative with respect to the independent variable

$$\mathscr{L} = \frac{\mathrm{d}^m}{\mathrm{d}t^m} \tag{8.11}$$

For initial value problems, the inverse operator $\mathscr{L}^{-1}$ is an m-fold integration from 0 to t, i.e.

$$\mathscr{L}^{-1} = \int_0^t \int_0^{\tau_m} \cdots \int_0^{\tau_2} \mathrm{d}\tau_1 \cdots \mathrm{d}\tau_{n-1} \mathrm{d}\tau_m \tag{8.12}$$

At the outset, we get

$$\mathscr{L}^{-1}\mathscr{L}y = y - y(0) - ty'(0) - \tfrac{1}{2}t^2y''(0) - \cdots = y - \sum_{k=0}^{m-1} \frac{t^k}{k!} \frac{\mathrm{d}^k y}{\mathrm{d}t^k}\bigg|_{t=0} \tag{8.13}$$

For instance, if $\mathscr{L}y = y''$, then

$$\mathscr{L}^{-1}\mathscr{L}y = y - y(0) - ty'(0) \tag{8.14}$$

For boundary value problems, the inverse operator is an m-fold indefinite integration. The constants of integration are then evaluated from the given boundary conditions

$$\mathscr{L}^{-1}\mathscr{L}y = y + C_0 + C_1t + \tfrac{1}{2}C_2t^2 + \cdots = y + \sum_{k=0}^{m-1} \frac{C_k}{k!}t^k \tag{8.15}$$

Evidently, the case with initial conditions may be determined from the general formula for a boundary value problem by setting

$$C_k = -\frac{\mathrm{d}^k y}{\mathrm{d}t^k}\bigg|_{t=0} \tag{8.16}$$

therefore, the form given by (8.15) will be adopted in subsequent discussions.

8.2.3 Decomposition

Now that the linear operator has been determined for a general case, (8.9) can be inverted. This procedure leads to

$$\mathscr{L}^{-1}\mathscr{L}y = \mathscr{L}^{-1}g(t) - \mathscr{L}^{-1}\mathscr{R}y - \mathscr{L}^{-1}\mathscr{N}y \tag{8.17}$$

or, by using (8.15) in (8.17) we get

$$y = \mathscr{L}^{-1}g(t) - \sum_{k=0}^{m-1}\frac{C_k}{k!}t^k - \mathscr{L}^{-1}\mathscr{R}y - \mathscr{L}^{-1}\mathscr{N}y \tag{8.18}$$

where m is the order of the linear operator. A close inspection of (8.18) clearly indicates that the first three terms may be easily determined. The difficulty, however, resides in inverting the nonlinear terms, as expected. To make further headway, Adomian (1984) proposed decomposing the dependent variable as a series of terms such that, the n^{th} term depends on the previous $(n-1)$ terms which subsequently depend on the initial term which is known. As such, we have

$$y = y_0 + y_1 + y_2 + \cdots = \sum_{n=0}^{\infty} y_n \tag{8.19}$$

Similarly, we assume that the nonlinear term can be decomposed into the following series

$$\mathscr{N}y = \sum_{n=0}^{\infty} A_n \tag{8.20}$$

The A_n's in (8.20) are known as the Adomian polynomials (Adomian 1988). These polynomials are constructed such that the determination of A_n requires knowledge of y_0 up to y_n only. We write this as

$$A_n \equiv A_n(y_0, y_1, \cdots, y_n) \tag{8.21}$$

Derivation of the Adomian polynomials will be considered at length in §8.2.4. For the present discussion, it is sufficient to know that such polynomials exist. Finally, inserting (8.19) and (8.20) in (8.18), one recovers

$$y_0+y_1+\cdots = \mathscr{L}^{-1}g(t)-\sum_{k=0}^{m-1}\frac{C_k}{k!}t^k-\mathscr{L}^{-1}\mathscr{R}(y_0+y_1+\cdots)-\mathscr{L}^{-1}(A_0+A_1+\cdots) \quad (8.22)$$

The final step consists in segregating terms in such a way that, starting with a base solution y_0, the n^{th} approximation y_n will only require knowledge of the previous terms. At the outset, this may be accomplished via

$$y_0 = \mathscr{L}^{-1}g(t) - \sum_{k=0}^{m-1}\frac{C_k}{k!}t^k \quad (8.23)$$

then

$$\begin{aligned} y_1 &= -\mathscr{L}^{-1}\mathscr{R}y_0 - \mathscr{L}^{-1}A_0 \\ y_2 &= -\mathscr{L}^{-1}\mathscr{R}y_1 - \mathscr{L}^{-1}A_1 \\ &\vdots \end{aligned} \quad (8.24)$$

Since, at every order, the previous order is known, then the solution is completely determined. At this point, we are to determine a proper expansion of the nonlinear operator by using the Adomian polynomials.

8.2.4 Adomian polynomials

The Adomian polynomials consist of a specific linearization of a general nonlinear operator $\mathscr{N}y$. They are constructed in such a way that the n^{th} polynomial requires the knowledge of the previous terms only. To illustrate this idea, we consider the following polynomial nonlinearity. Let

$$\mathscr{N}y = y^2 \quad (8.25)$$

Then, by employing the Adomian decomposition (8.19), we obtain

$$\mathscr{N}y = \mathscr{N}(y_0 + y_1 + y_2 + \cdots) = (y_0 + y_1 + y_2 + \cdots)^2 \tag{8.26}$$

or

$$\mathscr{N}y = A_0 + A_1 + A_2 + \cdots = y_0^2 + 2y_0y_1 + y_1^2 + 2y_0y_2 + 2y_1y_2 + y_2^2 + \cdots \tag{8.27}$$

According to the previous hypothesis, one can choose the Adomian polynomials to be

$$\begin{aligned} A_0 &= y_0^2 \\ A_1 &= 2y_0y_1 + y_1^2 \\ A_2 &= 2y_0y_2 + 2y_1y_2 + y_2^2 \\ &\vdots \end{aligned} \tag{8.28}$$

According to this arrangement, and given that y_0 is known via (8.23), the A_n's may be easily determined. This is not however the only option for the Adomian polynomials. In fact, one can posit

$$\begin{aligned} A_0 &= y_0^2 \\ A_1 &= 2y_0y_1 \\ A_2 &= y_1^2 + 2y_0y_2 \\ A_3 &= 2y_1y_2 + 2y_0y_3 \\ &\vdots \end{aligned} \tag{8.29}$$

The rationale here is to keep the sum of the indices of terms equal to the index of the polynomial (note that $y_1^2 = y_1y_1$, so that the sum of indices of this term is 2).

While this example is quite illuminating, the previous approach does not work well for functional nonlinearities, such as $\mathscr{N}y = \sin y$ or $\mathscr{N}y = e^y$. In this case, a parametrization is required and a functional formulation will guarantee extraction of the Adomian polynomials for a general nonlinearity. To this end, we introduce the parameter λ into the expansion for the dependent variable

$$y = y_0 + \lambda y_1 + \lambda^2 y_2 + \cdots = \sum_{n=0}^{\infty} \lambda^n y_n \tag{8.30}$$

Then, one can show that (Seng et al. 1996)

$$A_n = \frac{1}{n!} \frac{\mathrm{d}^n \mathscr{N}y(\lambda)}{\mathrm{d}\lambda^n}\bigg|_{\lambda=0} \tag{8.31}$$

This compact formula allows one to compute the Adomian polynomials for an arbitrary nonlinearity $\mathscr{N}y$. By way of example, (8.31) may be applied to the second order polynomial nonlinearity. We start by utilizing the parametric decomposition (8.30) in (8.25). This process gives

$$\mathscr{N}y = \mathscr{N}(y_0 + \lambda y_1 + \lambda^2 y_2 + \cdots) = (y_0 + \lambda y_1 + \lambda^2 y_2 + \cdots)^2 \tag{8.32}$$

or

$$\mathscr{N}y = y_0^2 + 2\lambda y_0 y_1 + \lambda^2(y_1^2 + 2y_0 y_2) + 2\lambda^3 y_1 y_2 + \lambda^4 y_2^2 + \cdots \tag{8.33}$$

Then, by applying (8.31) to (8.33), we recover

$$\begin{aligned} A_0 &= \mathscr{N}y(\lambda)|_{\lambda=0} = y_0^2 \\ A_1 &= \frac{\mathrm{d}\mathscr{N}y(\lambda)}{\mathrm{d}\lambda}\bigg|_{\lambda=0} = 2y_0 y_1 \\ A_2 &= \frac{1}{2!}\frac{\mathrm{d}^2\mathscr{N}y(\lambda)}{\mathrm{d}\lambda^2}\bigg|_{\lambda=0} = y_1^2 + 2y_0 y_2 \\ &\vdots \end{aligned} \tag{8.34}$$

It is interesting to note that (8.34) is identical to (8.29).

8.2.5 Boundary conditions

In the case of a boundary value problem, the Adomian Decomposition Method requires the evaluation of integration constants. There are three approaches to implementing the boundary conditions:

1. The zeroth order absorbs all boundary conditions while other orders have homogeneous boundary conditions

2. Obtain the solution to the desired order and then evaluate the constants

3. Evaluate the constants at every order

While the first item is the easiest to implement, it is generally not recommended due to the nature of the decomposition. By choosing to attach the boundary conditions to the base solution, the method will practically behave as a regular perturbation thus hindering its ability of capture the essential features of the problem without a small parameter.

The second approach seems to be a valid alternative, however, it works well only for linear operators. For the case of a nonlinear operator, one will have to solve a polynomial of order n to determine the constants. This requires the use a numerical technique thus outweighing the benefits of an analytical model.

We are only left with the final option that demands the evaluation of the integration constants at every order of the solution. This provides one with a relatively easy framework for the implementation of boundary conditions but consists of several evaluations at every order.

8.3 Application to regressing walls

We now turn our attention to the problem at hand and attempt a solution using the Adomian Decomposition Method. The ODE characteristic of this problem was given in the previous chapter as

$$\eta F'''' + \alpha(\eta F''' + 2F'') + \tfrac{1}{2}\mathrm{Re}(FF''' - F'F'') + 2F''' = 0 \tag{8.35}$$

To make an ADM solution accessible, we divide the above by η and write it in the following more convenient form

$$F'''' = -\alpha(F''' + 2\eta^{-1}F'') - \tfrac{1}{2}\mathrm{Re}\,\eta^{-1}(FF''' - F'F'') - 2\eta^{-1}F''' \tag{8.36}$$

Note that there is no condition on $F''(0)$. Provided that it is finite, the boundary condition $\sqrt{2\eta}F''(\eta)$ will be immediately satisfied at the centerline. We can easily identify the following operators

$$\mathscr{L}F = F'''' \tag{8.37a}$$

$$\mathscr{R}F = -\alpha(F''' + 2\eta^{-1}F'') - 2\eta^{-1}F''' \tag{8.37b}$$

$$\mathscr{N}F = -\tfrac{1}{2}\mathrm{Re}\,\eta^{-1}(FF''' - F'F'') \tag{8.37c}$$

or

$$\mathscr{L}F = \mathscr{R}F + \mathscr{N}F \tag{8.38}$$

The inverse operator is a four–fold indefinite integration

$$\mathscr{L}^{-1}F'''' = F + C_0 + C_1\eta + \tfrac{1}{2}C_2\eta^2 + \tfrac{1}{6}C_3\eta^3 \tag{8.39}$$

Then

$$\mathscr{L}^{-1}\mathscr{L}F = \mathscr{L}^{-1}\mathscr{R}F + \mathscr{L}^{-1}\mathscr{N}F \tag{8.40}$$

or

$$F = C_0 + C_1\eta + \tfrac{1}{2}C_2\eta^2 + \tfrac{1}{6}C_3\eta^3 + \mathscr{L}^{-1}\mathscr{R}F + \mathscr{L}^{-1}\mathscr{N}F \tag{8.41}$$

where negative signs have been absorbed into the constants. Now, we decompose F as follows

$$F = \sum_{n=0}^{\infty} F_n \tag{8.42}$$

then

$$\begin{aligned} F_0 + F_1 + F_2 + \cdots = C_0 + C_1\eta + \tfrac{1}{2}C_2\eta^2 + \tfrac{1}{6}C_3\eta^3 \\ + \mathscr{L}^{-1}\mathscr{R}(F_0 + F_1 + F_2 + \cdots) + \mathscr{L}^{-1}(A_0 + A_1 + A_2 + \cdots) \end{aligned} \tag{8.43}$$

8.3.1 Zeroth order solution

One selects

$$F_0(\eta) = C_0 + C_1\eta + \tfrac{1}{2}C_2\eta^2 + \tfrac{1}{6}C_3\eta^3 \tag{8.44}$$

Application of the boundary conditions yields

$$F_0(0) = C_0 = 0 \tag{8.45}$$

while

$$\lim_{\eta\to 0} \sqrt{2\eta}F''(\eta) = \sqrt{2\eta}C_2 = 0 \tag{8.46}$$

The above conditions is not very helpful since it is always satisfied as long as C_2 is finite. Given that we have no prior knowledge of C_2 we will have to evaluate it from the solution by substitution into the governing equation. For this, we assume that

$$F''(0) = \beta \tag{8.47}$$

and evaluate all other constants in terms of β. The remaining boundary conditions give

$$\begin{cases} F_0(\frac{1}{2}) & = C_1 + \frac{1}{4}\beta + \frac{1}{24}C_3 = 1 \\ F_0'(\frac{1}{2}) & = C_1 + \frac{1}{2}\beta + \frac{1}{8}C_3 = 0 \end{cases} \tag{8.48}$$

This operation yields

$$C_1 = -\tfrac{1}{8}\beta + 4; \quad C_3 = -3(\beta + 8) \tag{8.49}$$

At the outset, we have

$$F_0(\eta) = -\tfrac{1}{8}(\beta - 24)\eta + \tfrac{1}{2}\beta\eta^2 - \tfrac{1}{2}(\beta + 8)\eta^3 \tag{8.50}$$

At this juncture, one may evaluate β by substituting the F_0 into the governing equation and evaluating at the centerline. This yields

$$\tfrac{1}{16}\mathrm{Re}\beta^2 + \tfrac{1}{16}(16 - 24\mathrm{Re} + 32\alpha)\beta = 0 \tag{8.51}$$

the solution of which yields

$$\beta = 0; \quad \beta = 24 - 16\mathrm{Re}^{-1} - 32\alpha\mathrm{Re}^{-1} \tag{8.52}$$

Of course, the second solution for β will be the acceptable solution.

8.3.2 First order solution

At first order, we have

$$F_1 = \mathscr{L}^{-1}\mathscr{R}_0 + \mathscr{L}^{-1}A_0; \quad \mathscr{R}_0 \equiv \mathscr{R}(F_0) \tag{8.53}$$

where

$$\mathscr{R}_0 = -\eta^{-1}F_0''' - \alpha\eta^{-1}(\eta F_0''' + 2F_0'') \tag{8.54a}$$

$$A_0 = \tfrac{1}{2}\eta^{-1}\mathrm{Re}(F_0'F_0'' - F_0F_0''') \tag{8.54b}$$

Taking the inverse, we recover

$$F_1(\eta) = C_0 + C_1\eta + \tfrac{1}{2}C_2\eta^2 + \left(4\ln\eta + \tfrac{1}{6}C_3 - \frac{22}{3}\right)\eta^3 + 3\alpha\eta^4 + \tfrac{4}{15}\mathrm{Re}\,\eta^6 \tag{8.55}$$

In the present scheme, we apply homogeneous boundary conditions to all orders except the zeroth order. Then, we have

$$\lim_{\eta\to 0} F_1(\eta) = C_0 = 0 \tag{8.56a}$$

$$\lim_{\eta\to 0} F_1''(\eta) = C_2 = 0 \tag{8.56b}$$

$$F_1'(\tfrac{1}{2}) = 0 \tag{8.56c}$$

$$F_1(\tfrac{1}{2}) = 0 \tag{8.56d}$$

The last two conditions yield

$$\begin{cases} C_1 &= \tfrac{1}{80}(\mathrm{Re} + 15\alpha + 40) \\ C_2 &= -\tfrac{1}{2}(\mathrm{Re} + 27\alpha - 48\ln 2 - 64) \end{cases} \tag{8.57}$$

At the outset, we have

$$\begin{aligned} F_1(\eta) =& \tfrac{1}{80}(40 + \mathrm{Re} + 15\alpha)\eta + 3\alpha\eta^4 + \tfrac{4}{15}\mathrm{Re}\,\eta^6 \\ &+ \eta^3\left[-\tfrac{22}{3} + \tfrac{1}{12}(64 - \mathrm{Re} - 27\alpha + 48\ln 2) + 4\ln\eta\right] \end{aligned} \tag{8.58}$$

The higher order terms can be computed in a similar fashion.

8.3.3 Verification

The four term solution is plotted in Figures 8.1–8.2 for representative values of $\alpha = -1, -0.5, 0.5$, and 1. Unfortunately, the Adomian solution followed here fails to accurately reproduce the numerical results. The most intriguing results corresponds to the plot of the mean flow function $F(\eta)$ for Re ~ -1 in Figure 8.1b where near perfect matching with the numerical results is observed. However, this excellent matching appears to depreciate in the companion plot of $F'(\eta)$ in Figure 8.2b. The Re ~ 1 case shown in Figures 8.1a–8.2a displays the most disagreement with the numerical results. In fact, the curves corresponding to $\alpha < 0$ were omitted due to the large discrepancy in the data.

8.4 Summary

The results showcased in this section stress two important facts. Firstly, the problem at hand is an extremely complicated one and thus requires a more delicate treatment including a full numerical investigation and probably an extension of the decomposition method to allow for other base solutions. Secondly, the results indicate that even a method as powerful as the decomposition method has its peculiar pitfalls. The author hopes to address this problem in a future study using the Homotopy Analysis Method, a variant of Adomian's method that permits the use of arbitrary base functions.

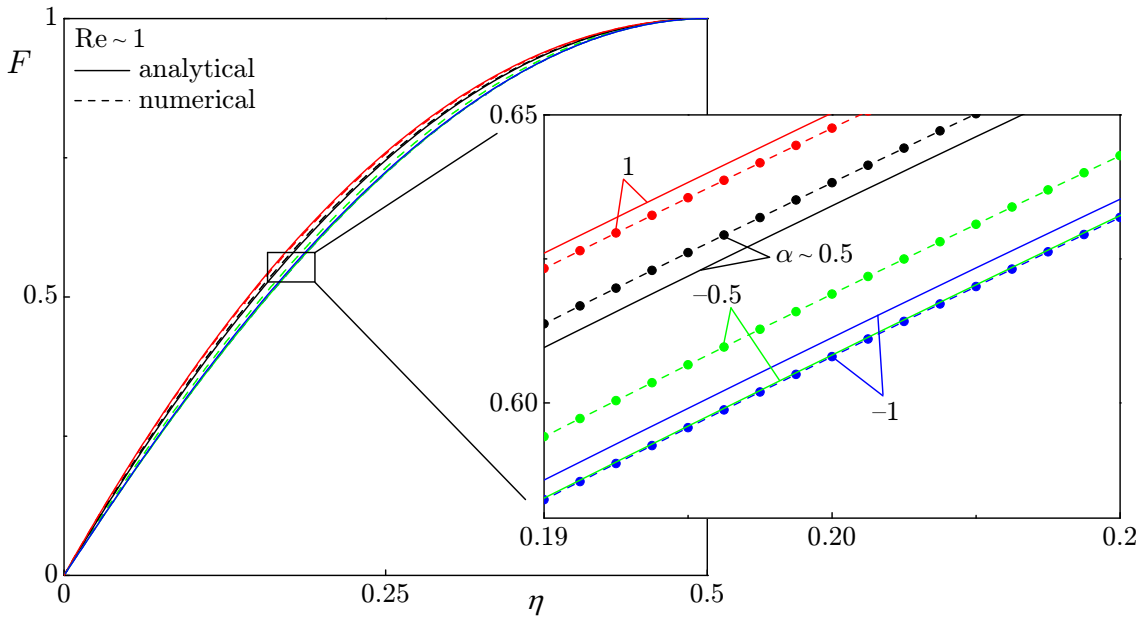

(a) Re ~ 1

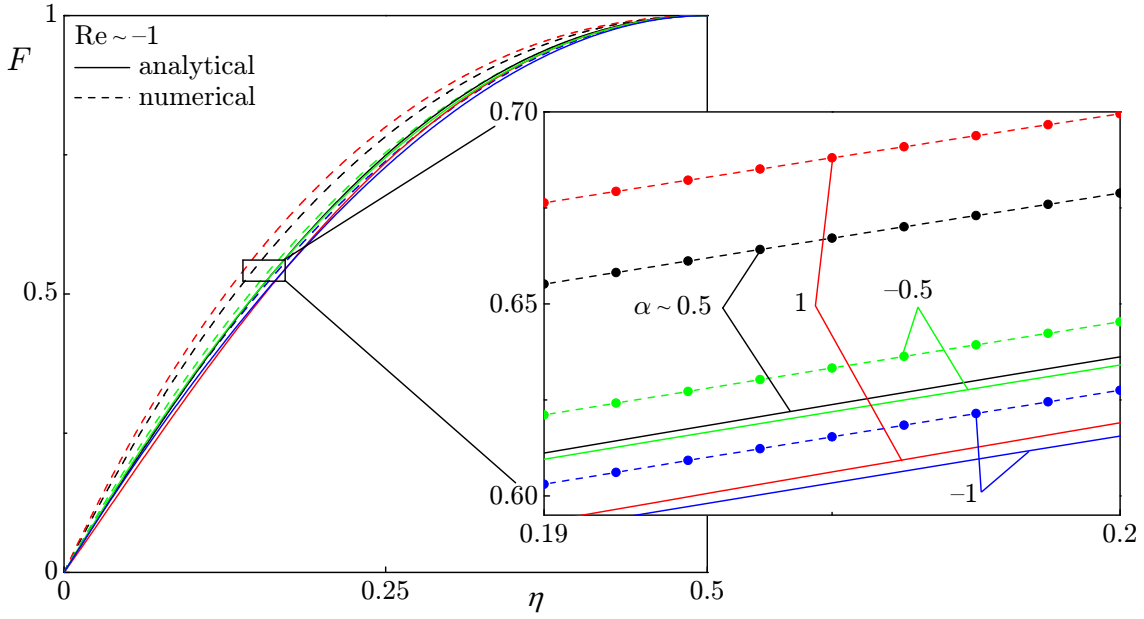

(b) Re ~ -1

Figure 8.1: Comparison between analytical (—) and numerical solutions (∘) for F using (a) Re ~ 1, and (b) Re ~ -1. Curves are shown for $\alpha \sim 0.5$, 1, -0.5, and -1.

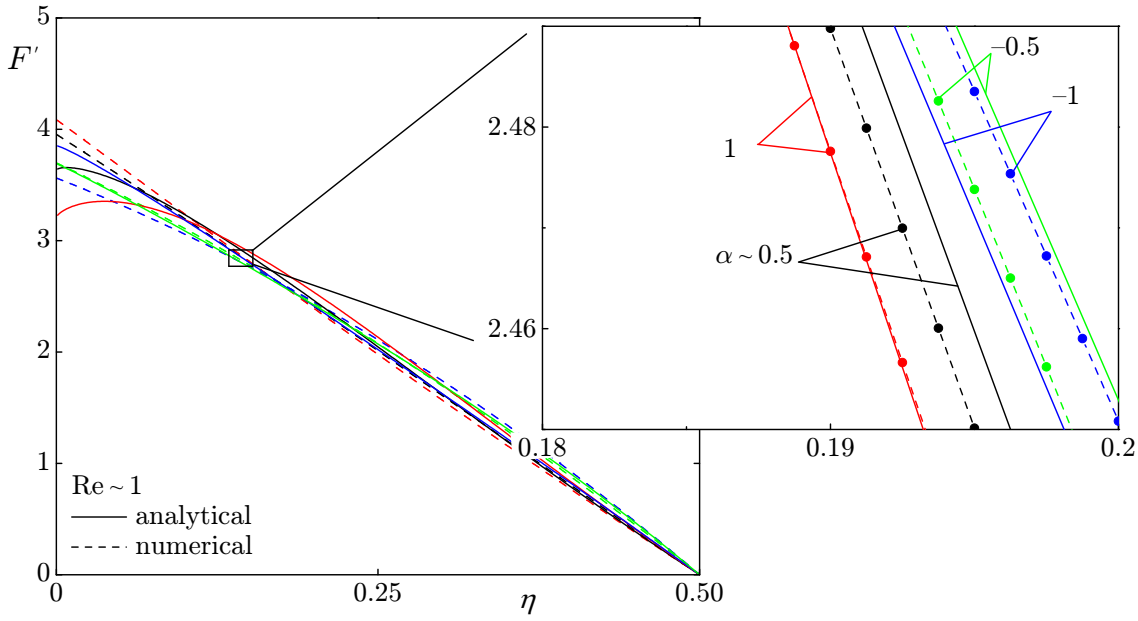

(a) Re ~ 1

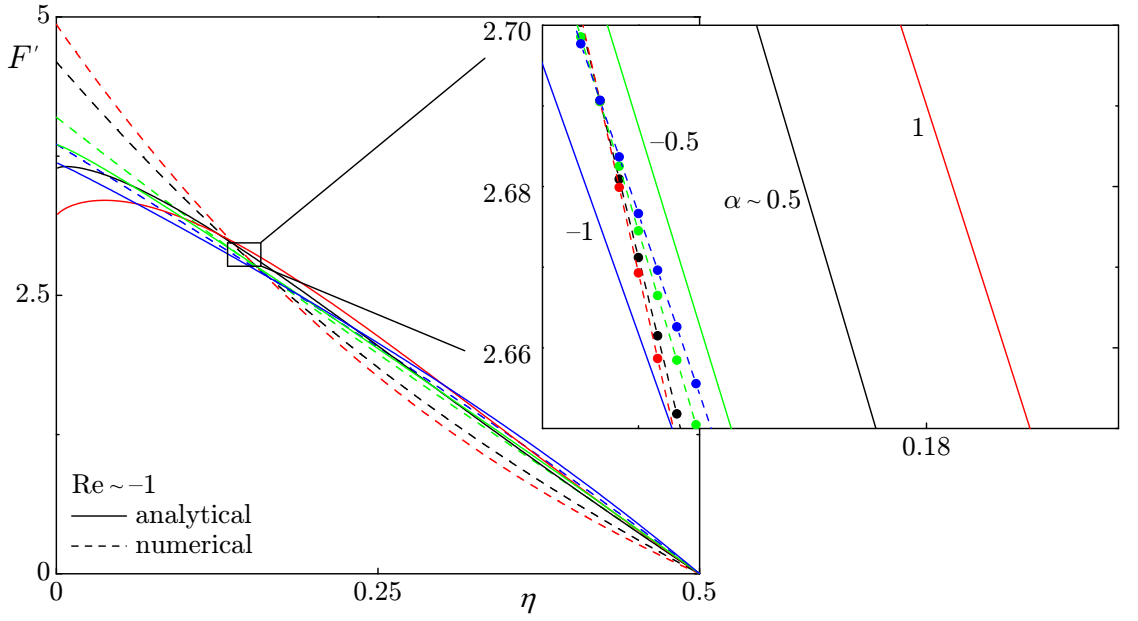

(b) Re ~ -1

Figure 8.2: Comparison between analytical (—) and numerical solutions (∘) for F' using (a) Re ~ 1, and (b) Re ~ -1. Curves are shown for $\alpha \sim 0.5$, 1, -0.5, and -1.

Chapter 9

Conclusions & Recommendations

In this chapter, we present a synthesis of the contributions made in this dissertation. We then conclude with an overview of the future work that would naturally extend the present research.

9.1 Principal contributions

Three principal contributions may be identified in this dissertation and they are briefly summarized in the following.

9.1.1 Variational formulation

The Taylor–Culick flow describing the gaseous motion in a porous cylinder is revisited using constrained optimization. In particular, the method of Lagrangian multipliers is utilized to identify a general form of the sidewall injection boundary condition. This boundary condition is written in the form of a constraint, $\sum(-1)^n\alpha_n = 1$ where α_n refers to the sidewall injection sequence. The resulting formulation helps us to establish two generic forms for α_n. The first Type I form is given by $\alpha_n^-(q) \sim (-1)^n(2n+1)^{-q}$ and generates solutions with kinetic energies that are less than Taylor–Culick's and that increase with increasing energy power index q. The

second or Type II form is conferred via $\alpha_n^+(q) \sim (2n+1)^{-q}$ and reproduces solutions with higher kinetic energies than their Taylor–Culick counterpart. These are found to decrease with increasing q. The most intriguing feature of the two families of motions is that they extend from purely irrotational motions with minimum energy signature to high rotational fields with maximum kinetic energy. Interestingly, the Taylor–Culick sinusoid is found to be at the confluence of both families as a special case.

9.1.2 Extension of Kelvin's theorem

Kelvin's minimum kinetic energy theorem is a famous principle in classic potential flow and aerodynamic lift theory. It assures that the irrotational motion of an incompressible fluid in a simply connected fluid region carries less kinetic energy than any other motion with the same velocity at its boundary. A boundary on which the velocity requirement is satisfied is referred to as a Kelvin surface while the term open is used to denote a boundary on which this requirement is breached. In Chapter 5, we extend Kelvin's classic theorem to compressible flows with open boundaries. The resulting generalization is embodied in an inequality that involves two volume integrals and a surface integral over the open boundary. This condition is then discussed and simplified in light of compressible flows with Kelvin boundaries and homogeneous incompressible flows with open boundaries. In the latter case, the criterion reduces to a simple evaluation of the surface integral of the rotational flux over the open boundary. This generalization takes us beyond Kelvin's classic constraints and grants it wider applicability in the theory of fluid motion.

9.1.3 Application of the Adomian Decomposition Method

The viscous flow in a porous cylinder with radially regressing walls may be represented by a fourth order nonlinear ordinary differential equation. This ODE poses many difficulties for a standard analytical treatment that beckons the use of advanced

nonlinear analytical methods. The classical approach has been perturbation theory and it proved to be very successful over a very wide range of Reynolds numbers. It is nonetheless quite informative to analyze this problem in light of other analytical methods that are suitable for nonlinear problems. In this respect, the Adomian Decomposition Method was chosen thanks to its simplicity and because it provides much of the infrastructure for other nonlinear methods such as the Homotopy Analysis Method. In Chapter 8, the Adomian Decomposition Method is systematically introduced and discussed in light of this nonlinear problem. The results for the cylindrical case were limited to the case of small Reynolds numbers because of the nature of the problem. The limitation in the choice of linear operator is the major pitfall for the method.

9.2 Future investigations

9.2.1 Multiple solutions

The flow in porous chambers has been extensively studied over the past few decades. The work of Berman (1953), Taylor (1956), Terrill and Thomas (1969) and many others provided the theoretical foundation for handling the nonlinearities in this problem. Terrill and Thomas (1969) were the first to explore multiple solutions for the flow in a porous pipe while Uchida and Aoki (1977) used a similarity transformation in space and time to derive the solution for the viscous flow in an impermeable pipe with moving walls. Later, Majdalani and coworkers (Majdalani and Zhou 2003; Dauenhauer and Majdalani 2003) combined both approaches and obtained analytical and numerical solutions for a porous channel with moving walls. Their work can be readily used in the study of solid rocket motors as it closely mimics propellant burning on the inner surface of the rocket. However, the exploration of multiple solutions for this problem has not been fully addressed yet. By using a transformation based on that proposed by Terrill and Thomas (1969) along with Runge–Kutta

integration, multiple branches of the flowfield can be captured and the admissible range of solutions can be obtained in terms of the wall Reynolds number and the wall permeability.

9.2.2 Homotopy Analysis Method

The Homotopy Analysis Method (HAM) is a novel analytical technique tailored for the solution of nonlinear differential equations. First introduced by Liao (1995), its roots can be traced back to the ideas of homotopy and the Adomian Decomposition Method. In fact, it may be viewed as a generalization of the Adomian Decomposition Method to the use of an arbitrary linear operator. Based on the results presented in Chapter 8, it is natural to seek a more accurate solution for the flow in a porous pipe with regressing walls. In fact, the method has been recently applied to the planar counterpart by Dinarvand and Rashidi (2009). Nonetheless, the case of the cylindrical configuration beckons a more detailed treatment given that one of the boundary conditions is always satisfied and thus must be computed at every solution order. By using the Homotopy Analysis Method, and by carefully choosing the "convergence–control parameter" $\hbar$ (Liao 2009), we also hope to capture multiple solutions analytically.

Bibliography

Bibliography

Adomian, G. (1984). A new approach to nonlinear partial differential equations. *Journal of Mathematical Analysis and Applications*, 102(2):420–434. doi:10.1016/0022-247X(84)90182-3. 124, 128

Adomian, G. (1988). A review of the decomposition method in applied mathematics. *Journal of Mathematical Analysis and Applications*, 135(2):501–544. doi:10.1016/0022-247X(88)90170-9. 124, 128

Adomian, G. (1994). *Solving frontier problems of physics: the decomposition method*. Kluwer Boston, MA. 124

Adomian, G. (1997). Explicit solutions of nonlinear partial differential equations. *Applied Mathematics and Computation*, 88(2-3):117–126. doi:10.1016/S0096-3003(96)00141-5. 125

Adomian, G. and Rach, R. (1992). Generalization of Adomian polynomials to functions of several variables. *Computers and Mathematics with Applications*, 24(5-6):11–24. doi:10.1016/0898-1221(92)90037-I. 125

Adomian, G. and Rach, R. (1996). Modified Adomian polynomials. *Mathematical and Computer Modelling*, 24(11):39–46. doi:10.1016/S0895-7177(96)00171-9. 125

Apte, S. and Yang, V. (2000). Effect of acoustic oscillation on flow development in a simulated nozzleless rocket motor. In *Solid Propellant Chemistry, Combustion, and Motor Interior Ballistics*, volume 185 of *Progress in Astronautics and Aeronautics*,

pages 791–822. AIAA Progress in Astronautics and Aeronautics, Washington, DC. 48

Apte, S. and Yang, V. (2001). Unsteady flow evolution in porous chamber with surface mass injection, part 1: free oscillation. *AIAA Journal*, 39(8):1577–1630. doi:10.2514/2.1483. 48

Apte, S. and Yang, V. (2002). Unsteady flow evolution in porous chamber with surface mass injection, part 2: acoustic excitation. *AIAA Journal*, 40(2):244–253. doi:10.2514/2.1666. 48

Batchelor, G. K. (1967). *An introduction to fluid dynamics*. Cambridge University Press, Cambridge. 79, 80, 85, 89

Berman, A. S. (1953). Laminar flow in channels with porous walls. *Journal of Applied Physics*, 24(9):1232–1235. doi:10.1063/1.1721476. 1, 2, 7, 18, 106, 142

Blank, B. E. and Krantz, S. G. (2006). *Calculus, multivariable*. Key College Publishing, Emeryville, CA. 38

Calero, J. S. (2008). *The genesis of fluid mechanics, 1640-1780*, volume 22 of *Studies in History and Philosophy of Science*. Springer Netherlands. doi:10.1007/978-1-4020-6414-2. 36

Chen, S., Eyink, G. L., Wan, M., and Xiao, Z. (2006). Is the Kelvin theorem valid for high Reynolds number turbulence? *Physical Review Letters*, 97:144505. doi:10.1103/PhysRevLett.97.144505. 79

Clairaut, A.-C. (1739). Recherches générales sur le calcul intégral. *Histoire de l'Académie Royale des Science avec les Mémoires de Mathématique et de Physiques*, 1:425–436. 36

Clairaut, A.-C. (1740). Sur l'intégration ou la construction des équations différentielles du premier ordre. *Histoire de l'Académie Royale des Science avec les Mémoires de Mathématique et de Physiques*, 1:293–323. 36

Clayton, C. D. (1996). Flow fields in solid rocket motors with tapered bores. In *32nd AIAA, ASME, SAE, and ASEE, Joint Propulsion Conference and Exhibit*, volume 96–2643. 6

Culick, F. E. C. (1966). Rotational axisymmetric mean flow and damping of acoustic waves in a solid propellant rocket. *AIAA Journal*, 4(8):1462–1464. doi:10.2514/3.3709. 1, 5, 12, 14, 16, 86, 110

Culick, F. E. C. (2006). Unsteady motions in combustion chambers for propulsion systems. Agardograph, Advisory Group for Aerospace Research and Development. 4, 5

Dauenhauer, E. C. and Majdalani, J. (1999). Unsteady flows in semi-infinite expanding channels with wall injection. In *30th AIAA Fluid Dynamics Conference, Norfolk, VA, 1999*. 7, 100

Dauenhauer, E. C. and Majdalani, J. (2003). Exact self-similarity solution of the navier–stokes equations for a porous channel with orthogonally moving walls. *Physics of Fluids*, 15(6):1485–1495. doi:10.1063/1.1567719. 7, 100, 103, 142

Dinarvand, S. and Rashidi, M. M. (2009). A reliable treatment of homotopy analysis method for two-dimensional viscous flow in a rectangular domain bounded by two moving porous walls. *Nonlinear Analysis: Real World Applications*, In Press, Accepted Manuscript. doi:10.1016/j.nonrwa.2009.03.006. 143

Doussineau, P. and Levelut, A. L. (2002). Differentiability breaking and Schwarz theorem violation in an aging material. *Physical Review B*, 66(2):024105. doi:10.1103/PhysRevB.66.024105. 38

Eckert, E. R. G., Donoughe, P. L., and Moore, B. J. (1957). Velocity and friction characteristics of laminar viscous boundary-layer and channel flow over surfaces with ejection or suction. Technical report, NACA Technical Note 4102. 4

Erdogan, M. E. and Imrak, C. E. (2008). On the flow in a uniformly porous pipe. *International Journal of Non-Linear Mechanics*, 43(4):292–301. doi:10.1016/j.ijnonlinmec.2007.12.006. 6

Euler, L. (1752). Principia motus fluidorum. *Novi Commentarii Academiae Scientiarum Petropolitanae*. 36, 47

Euler, L. (1755a). Continuation des rechèrches sur la théorie du mouvement des fluides. *Mémoires de lAcadémie de Sciences de Berlin*, 11:316–361. 36

Euler, L. (1755b). Principes généraux de l'état d'équilibre des fluides. *Mémoires de lAcadémie de Sciences de Berlin*, 11:217–273. 36

Euler, L. (1755c). Principes généraux du mouvement des fluides. *Mémoires de lAcadémie de Sciences de Berlin*, 11:274–315. 36

Eyink, G. L. (2006). Cascade of circulations in fluid turbulence. *Physical Review E (Statistical, Nonlinear, and Soft Matter Physics)*, 74(6):066302. doi:10.1103/PhysRevE.74.066302. 79

Flandro, G. A. (1967). *Rotating flows in acoustically unstable rocket motors*. PhD thesis, California Institute of Technology. 6

Flandro, G. A. (1983). Nonlinear combustion of a solid propellant with velocity coupling. In *19th AIAA Joint Propulsion Conference*, volume 83-1269. 6

Flandro, G. A. (1985). Energy balance analysis of nonlinear combustion instability. *Journal of Propulsion Power*, 1(3):210–221. 6

Flandro, G. A. (1986). Vortex driving mechanisms in oscillatory rocket flows. *Journal of Propulsion and Power*, 2(3):206–214. 6

Flandro, G. A. (1995a). Effects of vorticity on rocket combustion stability. *Journal of Propulsion Power*, 11(4):607–625. 6

Flandro, G. A. (1995b). On flow turning. In *31st ASME, SAE, and ASEE, Joint Propulsion Conference and Exhibit*, volume 95-2530 of *(AIAA Paper 1995-2730)*, San Diego, CA. 6

Goto, M. and Uchida, S. (1990). Unsteady flows in a semi–infinite expanding pipe with injection through wall. *Journal of the Japan Society for Aeronautical and Space Sciences*, 38:434. 7, 100, 101

Grad, H. (1949). Resonance burning in rocket motors. *Communications on Pure and Applied Mathematics*, 2(1):79–102. 5

Hart, R. and McClure, F. (1965). Theory of acoustic instability in solid-propellant rocket combustion. In *Tenth Symposium (International) on Combustion*, volume 10, pages 1047–1065. doi:10.1016/S0082-0784(65)80246-6. 5

Hart, R. W., Bird, J. F., and McClure, F. T. (1960). *The Influence of Erosive Burning on Acoustic Instability in Solid Propellant Rocket Motors*. Storming Media. 5

Hart, R. W. and Cantrell, R. H. (1963). Amplification and attenuation of sound by burning propellants. *AIAA Journal*, 1(2):398–404. 5

Hart, R. W. and McClure, F. T. (1959). Combustion instability: Acoustic interaction with a burning propellant surface. *The Journal of Chemical Physics*, 30(6):1501–1514. doi:10.1063/1.1730226. 5

Hughes, W. F. and Gaylord, E. W. (1964). *Basic equations of engineering science*. McGraw-Hill. 38

Janzen, O. (1913). Beitrag zu einer theorie der stationaren stromung kompressibler flussigkeiten (towards a theory of stationary flow of compressible fluids). *Phys. Zeitschr*, 14:639643. 6

Karamcheti, K. (1966). *Principles of ideal-fluid aerodynamics*. John Wiley & Sons Inc. 13, 14, 29

Kurdyumov, V. N. (2006). Steady flows in the slender, noncircular, combustion chambers of solid propellant rockets. *AIAA Journal*, 44(12):2979–2986. doi:10.2514/1.21125. 6

Lamb, H. (1895). *Hydrodynamics*. Cambridge University Press, Cambridge, UK. 79

Liao, S. (1995). An approximate solution technique not depending on small parameters: a special example. *International Journal of Non Linear Mechanics*, 30(3):371–380. 143

Liao, S.-J. (2009). Notes on the homotopy analysis method: Some definitions and theorems. *Communications in Nonlinear Science and Numerical Simulation*, 14(4):983–997. doi:10.1016/j.cnsns.2008.04.013. 143

Maicke, B. A. and Majdalani, J. (2008). On the rotational compressible Taylor flow in injection-driven porous chambers. *Journal of Fluid Mechanics*, 603:391–411. doi:10.1017/S0022112008001122. 6, 12

Maicke, B. A. and Majdalani, J. (2009). A constant shear stress core flow model of the bidirectional vortex. *Proceedings of the Royal Society A: Mathematical, Physical and Engineering Science*, 465(2103):915–935. doi:10.1098/rspa.2008.0342. 90

Majdalani, J. (2007). On steady rotational high speed flows: the compressible Taylor–Culick profile. *Proceedings of the Royal Society A: Mathematical, Physical and Engineering Science*, 463(2077):131–162. doi:10.1098/rspa.2006.1755. 6, 12

Majdalani, J. (2009). Exact eulerian solutions of the cylindrical bidirectional vortex. In *45th AIAA/ASME/SAE/ASEE Joint Propulsion Conference and Exhibit*, (AIAA Paper 2009-5307), Denver, Colorado. 90

Majdalani, J. and Chiaverini, M. J. (2009). On steady rotational cyclonic flows: The viscous bidirectional vortex. *Physics of Fluids*, 21(10):10360301–10360315. 90

Majdalani, J. and Rienstra, S. (2007). On the bidirectional vortex and other similarity solutions in spherical coordinates. *Zeitschrift für Angewandte Mathematik und Physik (ZAMP)*, 58(2):289–308. doi:10.1007/s00033-006-5058-y. 90

Majdalani, J. and Saad, T. (2007). The Taylor–Culick profile with arbitrary headwall injection. *Physics of Fluids*, 19(9):093601–10. doi:10.1063/1.2746003. 7, 12, 44, 45, 68

Majdalani, J., Vyas, A. B., and Flandro, G. A. (2002). Higher mean–flow approximation for a solid rocket motor with radially regressing walls. *AIAA Journal*, 40(9):1780–1788. 4, 8, 100, 109, 114

Majdalani, J., Vyas, A. B., and Flandro, G. A. (2009). Higher Mean-Flow approximation for a solid rocket motor with radially regressing walls - erratum. *AIAA Journal*, 47(1):286–286. doi:10.2514/1.40061. 8, 100, 114

Majdalani, J. and Zhou, C. (2003). Moderate-to-large injection and suction driven channel flows with expanding or contracting walls. *Journal of Applied Mathematics and Mechanics*, 83(3):181–196. doi:10.1002/zamm.200310018. 2, 8, 100, 142

McClure, F. T., Cantrell, R. H., and Hart, R. W. (1963). Interaction between sound and flow: Stability of T-Burners. *AIAA Journal*, 1(3):586–590. doi:10.2514/3.54846. 5, 63

McClure, F. T., Hart, R. W., and Bird, J. F. (1960). Acoustic resonance in solid propellant rockets. *Journal of Applied Physics*, 31(5):884–896. doi:10.1063/1.1735713. 5

Panton, R. (2005). *Incompressible Flow*. John Wiley & Sons INC., New York, third edition. 28

Price, B. (1857). *A treatise on infinitesimal calculus, containing differential and integral calculus, calculus of variations, applications to algebra and geometry, and analytical mechanics*, volume 2. Oxford University Press. 38, 41

Proudman, I. (1960). An example of steady laminar flow at large reynolds number. *Journal of Fluid Mechanics*, 9(4):593–602. doi:10.1017/S002211206000133X. 2

Rach, R. (1984). A convenient computational form for the Adomian polynomials. *Journal of Mathematical Analysis and Applications*, 102(2):415–419. doi:10.1016/0022-247X(84)90181-1. 125

Rayleigh, L. (1916). On the flow of compressible fluid past an obstacle. *Philosophical Magazine*, 32(1):1–6. 6

Robinson, W. A. (1976). The existence of multiple solutions for the laminar flow in a uniformly porous channel with suction at both walls. *Journal of Engineering Mathematics*, 10(1):23–40. doi:10.1007/BF01535424. 4

Rogawski, J. D. (2008). *Calculus : early transcendentals*. W.H. Freeman, New York. 38

Saad, T. and Majdalani, J. (2007). The Taylor profile in porous channels with arbitrary headwall injection. In *37th AIAA Fluid Dynamics Conference and Exhibit*, (AIAA Paper 2007-4120), Miami, Florida. AIAA. 89

Saad, T. and Majdalani, J. (2008a). Energy based mean flow solutions for slab hybrid rocket chambers. In *44th AIAA/ASME/SAE/ASEE Joint Propulsion Conference and Exhibit*, (AIAA Paper 2008-5021), Hartford, Connecticut. 7, 90

Saad, T. and Majdalani, J. (2008b). Energy based solutions of the bidirectional vortex. In *44th AIAA/ASME/SAE/ASEE Joint Propulsion Conference and Exhibit*, (AIAA Paper 2008-4832), Hartford, Connecticut. 7, 90, 93

Saad, T. and Majdalani, J. (2009a). Energy based solutions of the bidirectional vortex with multiple mantles. In *45th AIAA/ASME/SAE/ASEE Joint Propulsion Conference and Exhibit*, (AIAA Paper 2009-5305), Denver, Colorado. 7

Saad, T. and Majdalani, J. (2009b). Rotational flowfields in porous channels with arbitrary headwall injection. *Journal of Propulsion and Power*, 25(4):921–929. doi:10.2514/1.41926. 7, 44, 89

Saad, T. and Majdalani, J. (2010). On the Lagrangian optimization of wall-injected flows: from the Hart-McClure potential to the Taylor-Culick rotational motion. *Proceedings of the Royal Society A: Mathematical, Physical and Engineering Science*, 466(2114):331–362. doi:10.1098/rspa.2009.0326. 7

Saad, T., Sams, O. C., IV, and Majdalani, J. (2006). Rotational flow in tapered slab rocket motors. *Physics of Fluids*, 18(10):103601. doi:10.1063/1.2354193. 6

Sams, O. C., Majdalani, J., and Saad, T. (2007). Mean flow approximations for solid rocket motors with tapered walls. *Journal of Propulsion and Power*, 23(2):445–456. doi:10.2514/1.15831. 6

Sellars, J. R. (1955). Laminar flow in channels with porous walls at high suction reynolds numbers. *Journal of Applied Physics*, 26(4):489–490. doi:10.1063/1.1722024. 2

Seng, V., Abbaoui, K., and Cherruault, Y. (1996). Adomian's polynomials for nonlinear operators. *Mathematical and Computer Modelling*, 24(1):59–65. doi:10.1016/0895-7177(96)00080-5. 131

Sommerfeld, A. (1950). *Mechanics of Deformable Bodies*. Academic Press. 28

Sutton, G. and Biblarz, O. (2000). *Rocket propulsion elements*. Wiley-Interscience. 8

Taylor, G. (1956). Fluid flow in regions bounded by porous surfaces. *Proceedings of the Royal Society A: Mathematical, Physical and Engineering Sciences*, 234(1199):456–475. doi:10.1098/rspa.1956.0050. 1, 3, 5, 86, 142

Terrill, R. (1964). Laminar flow in a uniformly porous channel (Laminar flow in two-dimensional channel with porous walls assuming uniformly injected fluid). *Aeronautical Quarterly*, 15:299–310. 2, 3, 4

Terrill, R. M. (1965). Laminar flow in a uniformly porous channel with large injection (Laminar flow in two-dimensional channel with uniformly porous walls through which fluid is uniformly injected). *Aeronautical Quarterly*, 16:323–332. 3, 4

Terrill, R. M. and Thomas, P. W. (1969). On laminar flow through a uniformly porous pipe. *Applied Scientific Research*, 21(1):37–67. doi:10.1007/BF00411596. 1, 4, 103, 142

Thomson, W. (1849). Notes on hydrodynamics V: On the vis-viva of a liquid in motion. *Cambridge and Dublin Mathematical Journal*, 4:90–94. 79

Tsangaris, S., Kondaxakis, D., and Vlachakis, N. (2007). Exact solution for flow in a porous pipe with unsteady wall suction and/or injection. *Communications in Nonlinear Science and Numerical Simulation*, 12(7):1181–1189. doi:10.1016/j.cnsns.2005.12.009. 6

Uchida, S. and Aoki, H. (1977). Unsteady flows in a semi-infinite contracting or expanding pipe. *Journal of Fluid Mechanics*, 82(2):371–387. doi:10.1017/S0022112077000718. 7, 100, 142

Vyas, A. B. and Majdalani, J. (2006). Exact solution of the bidirectional vortex. *AIAA Journal*, 44(10):2208–2216. doi:10.2514/1.14872. 90, 92, 159

White, F. M. (2005). *Viscous fluid flow*. McGraw-Hill, New York, 3 edition. 2, 4, 18, 29, 86, 89

White, F. M., Barfield, B. F., and Goglia, M. J. (1958). Laminar flow in a uniformly porous channel. *J. Appl. Mech*, 25:613. 3

Wu, J. Z., Ma, H. Y., and Zhou, M. D. (2006). *Vorticity and vortex dynamics*. Springer-Verlag, New York. doi:10.1007/978-3-540-29028-5. 79

Yuan, S. W. (1956). Further investigation of laminar flow in channels with porous walls. *Journal of Applied Physics*, 27(3):267–269. doi:10.1063/1.1722355. 3

Zaturska, M., Drazin, P., and Banks, W. (1988). On the flow of a viscous fluid driven along a channel by suction at porous walls. *Fluid Dynamics Research*, 4(3):151–178. doi:10.1016/0169-5983(88)90021-4. 4

Appendix

Appendix A

Summary of Arbitrary Injection Solutions

This appendix lists a summary of the solutions for the inviscid flow in a porous channel or pipe with arbitrary headwall injection. Note that for the cylindrical configuration, u, v, and w stand for the radial (r), tangential (θ), and axial (z) components of the velocity field, respectively while for the channel case these denote the axial (x), transverse (y), and spanwise (z) components.

Planar

Table A.1: Summary of solutions for the inviscid flow in a porous channel with arbitrary headwall injection. Here, $\chi_n \equiv \frac{1}{2}(2n+1)\pi y$ and U_c is the centerline axial velocity at the headwall $x = 0$.

Headwall $u(0,y)$	Streamfunction $\psi(x,y)$	Axial Velocity $u(x,y)$
0	$\psi_\mathrm{ref} \equiv x\sin(\frac{1}{2}\pi y)$	$u_\mathrm{ref} \equiv \frac{1}{2}\pi x\cos(\frac{1}{2}\pi y)$
U_c	$\psi_\mathrm{ref} + \dfrac{8U_\mathrm{c}}{\pi^2}\displaystyle\sum_{n=0}^{\infty}\frac{(-1)^n\sin\chi_n}{(2n+1)^2}$	$u_\mathrm{ref} + \dfrac{4U_\mathrm{c}}{\pi}\displaystyle\sum_{n=0}^{\infty}\frac{(-1)^n\cos\chi_n}{(2n+1)}$
$U_\mathrm{c}\cos(\frac{1}{2}\pi y)$	$\psi_\mathrm{ref} + \dfrac{2U_\mathrm{c}}{\pi}\sin(\frac{1}{2}\pi y)$	$u_\mathrm{ref} + U_\mathrm{c}\cos(\frac{1}{2}\pi y)$
$U_\mathrm{c}(1-y^2)$	$\psi_\mathrm{ref} + \dfrac{64U_\mathrm{c}}{\pi^4}\displaystyle\sum_{n=0}^{\infty}\frac{(-1)^n\sin\chi_n}{(2n+1)^4}$	$u_\mathrm{ref} + \dfrac{32U_\mathrm{c}}{\pi^3}\displaystyle\sum_{n=0}^{\infty}\frac{(-1)^n\cos\chi_n}{(2n+1)^3}$

Cynlindrical

Table A.2: Summary of solutions for the inviscid flow in a porous pipe with arbitrary headwall injection. Here, $\chi_n \equiv \frac{1}{2}(2n+1)\pi r^2$ and W_c is the centerline axial velocity at the headwall $z = 0$.

Headwall $w(r,0)$	Streamfunction $\psi(r,z)$	Axial Velocity $w(r,z)$
0	$\psi_\mathrm{ref} \equiv z\sin(\frac{1}{2}\pi r^2)$	$w_\mathrm{ref} \equiv \pi z\cos(\frac{1}{2}\pi r^2)$
W_c	$\psi_\mathrm{ref} + \dfrac{4W_\mathrm{c}}{\pi^2}\displaystyle\sum_{n=0}^{\infty}\frac{(-1)^n\sin\chi_n}{(2n+1)^2}$	$w_\mathrm{ref} + \dfrac{4W_\mathrm{c}}{\pi}\displaystyle\sum_{n=0}^{\infty}\frac{(-1)^n\cos\chi_n}{(2n+1)}$
$W_\mathrm{c}\cos(\frac{1}{2}\pi r^2)$	$\psi_\mathrm{ref} + \dfrac{W_\mathrm{c}}{\pi}\sin(\frac{1}{2}\pi r^2)$	$w_\mathrm{ref} + W_\mathrm{c}\cos(\frac{1}{2}\pi r^2)$
$W_\mathrm{c}(1-r^2)$	$\psi_\mathrm{ref} + \dfrac{8W_\mathrm{c}}{\pi^3}\displaystyle\sum_{n=0}^{\infty}\frac{\sin\chi_n}{(2n+1)^3}$	$w_\mathrm{ref} + \dfrac{8W_\mathrm{c}}{\pi^2}\displaystyle\sum_{n=0}^{\infty}\frac{\cos\chi_n}{(2n+1)^2}$

Appendix B

Summary of Variational Solutions

This appendix contains a summary of the variational solutions for both planar and cylindrical configurations with arbitrary injection as well as the bidirectional vortex based on the complex lamellar solution. Note that for cylindrical configurations, u, v, and w stand for the radial (r), tangential(θ), and axial (z) components of the velocity field, respectively while for the channel case these denote the axial (x), transverse (y), and spanwise (z) components.

Bidirectional vortex

Table B.1: Solution with least or most kinetic energy for the bidirectional vortex. Here, $\chi_n \equiv (2n+1)\,\pi r^2$, $\kappa \equiv Q_i/(2\pi L)$, and Q_i is the normalized volumetric inlet flowrate.

Quantity	Type I (least KE)	Vyas-Majdalani (2006)	Type II (most KE)
ψ	$\dfrac{8\kappa}{\pi^2} z \displaystyle\sum_{n=0}^{\infty} \dfrac{(-1)^n \sin\chi_n}{(2n+1)^2}$	$\kappa z \sin(\pi r^2)$	$\dfrac{\kappa}{\mathscr{C}} z \displaystyle\sum_{n=0}^{\infty} \dfrac{\sin\chi_n}{(2n+1)^2}$
u	$-\dfrac{8\kappa}{\pi^2 r} \displaystyle\sum_{n=0}^{\infty} \dfrac{(-1)^n \sin\chi_n}{(2n+1)^2}$	$-\dfrac{\kappa}{r} \sin(\pi r^2)$	$-\dfrac{\kappa}{r\mathscr{C}} \displaystyle\sum_{n=0}^{\infty} \dfrac{\sin\chi_n}{(2n+1)^2}$
w	$\dfrac{16\kappa}{\pi} z \displaystyle\sum_{n=0}^{\infty} \dfrac{(-1)^n \cos\chi_n}{(2n+1)}$	$2\pi\kappa z \cos(\pi r^2)$	$\dfrac{2\pi\kappa}{\mathscr{C}} z \displaystyle\sum_{n=0}^{\infty} \dfrac{\cos\chi_n}{(2n+1)}$
ω_θ	0	$4\pi^2\kappa r z \sin(\pi r^2)$	$\dfrac{2\pi^2\kappa}{\mathscr{C}} r z \csc(\pi r^2)$

Channel

Table B.2: Least kinetic energy solutions for the porous channel with $\chi_n \equiv \frac{1}{2}(2n+1)\pi y$.

Headwall	Streamfunction	Axial Velocity
0	$\psi_0^- \equiv \dfrac{8}{\pi^2} x \displaystyle\sum_{n=0}^{\infty} \dfrac{(-1)^n \sin\chi_n}{(2n+1)^2} \mapsto xy$	$u_0^- \equiv \dfrac{4}{\pi} x \displaystyle\sum_{n=0}^{\infty} \dfrac{(-1)^n \cos\chi_n}{(2n+1)} \mapsto x$
U_c	$\psi_0^- + \dfrac{8U_\mathrm{c}}{\pi^2} \displaystyle\sum_{n=0}^{\infty} \dfrac{(-1)^n \sin\chi_n}{(2n+1)^2}$	$u_0^- + \dfrac{4U_\mathrm{c}}{\pi} \displaystyle\sum_{n=0}^{\infty} \dfrac{(-1)^n \cos\chi_n}{(2n+1)}$
$U_\mathrm{c}\cos(\frac{1}{2}\pi y)$	$\psi_0^- + \dfrac{2U_\mathrm{c}}{\pi}\sin(\frac{1}{2}\pi y)$	$u_0^- + U_\mathrm{c}\cos(\frac{1}{2}\pi y)$
$U_\mathrm{c}(1-y^2)$	$\psi_0^- + \dfrac{64U_\mathrm{c}}{\pi^4} \displaystyle\sum_{n=0}^{\infty} \dfrac{\sin\chi_n}{(2n+1)^4}$	$u_0^- + \dfrac{32U_\mathrm{c}}{\pi^3} \displaystyle\sum_{n=0}^{\infty} \dfrac{\cos\chi_n}{(2n+1)^2}$

Table B.3: Most kinetic energy solutions for the porous channel with $\chi_n \equiv \frac{1}{2}(2n+1)\pi y$.

Headwall	Streamfunction	Axial Velocity
0	$\psi_0^+ \equiv \dfrac{x}{\mathscr{C}} \displaystyle\sum_{n=0}^{\infty} \dfrac{\sin\chi_n}{(2n+1)^2}$	$u_0^+ \equiv \dfrac{\pi}{2\mathscr{C}} x \displaystyle\sum_{n=0}^{\infty} \dfrac{\cos\chi_n}{(2n+1)}$
U_c	$\psi_0^+ + \dfrac{8U_\mathrm{c}}{\pi^2} \displaystyle\sum_{n=0}^{\infty} \dfrac{(-1)^n \sin\chi_n}{(2n+1)^2}$	$u_0^+ + \dfrac{4U_\mathrm{c}}{\pi} \displaystyle\sum_{n=0}^{\infty} \dfrac{(-1)^n \cos\chi_n}{(2n+1)}$
$U_\mathrm{c}\cos(\frac{1}{2}\pi y)$	$\psi_0^+ + \dfrac{2U_\mathrm{c}}{\pi^2}\sin(\frac{1}{2}\pi y)$	$u_0^+ + U_\mathrm{c}\cos(\frac{1}{2}\pi y)$
$U_\mathrm{c}(1-y^2)$	$\psi_0^+ + \dfrac{64U_\mathrm{c}}{\pi^2} \displaystyle\sum_{n=0}^{\infty} \dfrac{(-1)^n \sin\chi_n}{(2n+1)^4}$	$u_0^+ + \dfrac{32U_\mathrm{c}}{\pi} \displaystyle\sum_{n=0}^{\infty} \dfrac{(-1)^n \cos\chi_n}{(2n+1)^3}$

Table B.4: Vorticity for the porous channel with least or most kinetic energy.

Headwall	Type I vorticity	Type II vorticity
0	0	$\omega_0^+ \equiv \dfrac{\pi^2}{8\mathscr{C}} x \csc(\frac{1}{2}\pi y)$
U_c	0	ω_0^+
$U_\mathrm{c}\cos(\frac{1}{2}\pi y)$	$\frac{1}{2}\pi U_\mathrm{c}\sin(\frac{1}{2}\pi y)$	$\omega_0^+ + \frac{1}{2}\pi U_\mathrm{c}\sin(\frac{1}{2}\pi y)$
$U_\mathrm{c}(1-y^2)$	$2U_\mathrm{c}\, y$	$\omega_0^+ + 2U_\mathrm{c}\, y$

Cylindrical

Table B.5: Least kinetic energy solutions for the porous cylinder with $\chi_n \equiv \frac{1}{2}(2n+1)\pi r^2$.

Headwall	Streamfunction	Axial Velocity
0	$\psi_0^- \equiv \dfrac{8}{\pi^2} z \displaystyle\sum_{n=0}^{\infty} \dfrac{(-1)^n \sin\chi_n}{(2n+1)^2} \mapsto r^2 z$	$w_0^- \equiv \dfrac{8}{\pi} z \displaystyle\sum_{n=0}^{\infty} \dfrac{(-1)^n \cos\chi_n}{(2n+1)} \mapsto 2z$
$W_{\rm c}$	$\psi_0^- + \dfrac{4W_{\rm c}}{\pi^2} \displaystyle\sum_{n=0}^{\infty} \dfrac{(-1)^n \sin\chi_n}{(2n+1)^2}$	$w_0^- + \dfrac{4W_{\rm c}}{\pi} \displaystyle\sum_{n=0}^{\infty} \dfrac{(-1)^n \cos\chi_n}{(2n+1)}$
$W_{\rm c}\cos(\frac{1}{2}\pi r^2)$	$\psi_0^- + \dfrac{W_{\rm c}}{\pi}\sin(\frac{1}{2}\pi r^2)$	$w_0^- + W_{\rm c}\cos(\frac{1}{2}\pi r^2)$
$W_{\rm c}(1-r^2)$	$\psi_0^- + \dfrac{8W_{\rm c}}{\pi^3} \displaystyle\sum_{n=0}^{\infty} \dfrac{\sin\chi_n}{(2n+1)^3}$	$w_0^- + \dfrac{8W_{\rm c}}{\pi^2} \displaystyle\sum_{n=0}^{\infty} \dfrac{\cos\chi_n}{(2n+1)^2}$

Table B.6: Most kinetic energy solutions for the porous cylinder with $\chi_n \equiv \frac{1}{2}(2n+1)\pi r^2$.

Headwall	Streamfunction	Axial Velocity
0	$\psi_0^+ \equiv \dfrac{z}{\mathscr{C}} \displaystyle\sum_{n=0}^{\infty} \dfrac{\sin\chi_n}{(2n+1)^2}$	$w_0^+ \equiv \dfrac{\pi}{\mathscr{C}} z \displaystyle\sum_{n=0}^{\infty} \dfrac{\cos\chi_n}{(2n+1)}$
$W_{\rm c}$	$\psi_0^+ + \dfrac{4W_{\rm c}}{\pi^2} \displaystyle\sum_{n=0}^{\infty} \dfrac{(-1)^n \sin\chi_n}{(2n+1)^2}$	$w_0^+ + \dfrac{4W_{\rm c}}{\pi} \displaystyle\sum_{n=0}^{\infty} \dfrac{(-1)^n \cos\chi_n}{(2n+1)}$
$W_{\rm c}\cos(\frac{1}{2}\pi r^2)$	$\psi_0^+ + \dfrac{W_{\rm c}}{\pi}\sin(\frac{1}{2}\pi r^2)$	$w_0^+ + W_{\rm c}\cos(\frac{1}{2}\pi r^2)$
$W_{\rm c}(1-r^2)$	$\psi_0^+ + \dfrac{8W_{\rm c}}{\pi^3} \displaystyle\sum_{n=0}^{\infty} \dfrac{\sin\chi_n}{(2n+1)^3}$	$w_0^+ + \dfrac{8W_{\rm c}}{\pi^2} \displaystyle\sum_{n=0}^{\infty} \dfrac{\cos\chi_n}{(2n+1)^2}$

Table B.7: Vorticity for the porous cylinder with least or most kinetic energy.

Headwall	Type I vorticity	Type II vorticity
0	0	$\omega_0^+ \equiv \dfrac{\pi^2}{2\mathscr{C}} r z \csc(\frac{1}{2}\pi r^2)$
$W_{\rm c}$	0	ω_0^+
$W_{\rm c}\cos(\frac{1}{2}\pi r^2)$	$\pi W_{\rm c} r \sin(\frac{1}{2}\pi r^2)$	$\omega_0^+ + \pi W_{\rm c} r \sin(\frac{1}{2}\pi r^2)$
$W_{\rm c}(1-r^2)$	$2W_{\rm c} r$	$\omega_0^+ + 2W_{\rm c} r$

Vita

Tony Saad was born in Hadath, a city at the outskirts of Beirut, Lebanon, on September 8, 1980. After receiving his education at the French Lasallian College in Lebanon, he went on to earn his Bachelor's degree in Mechanical Engineering from Notre Dame University where he graduated Magna Cum Laude. In 2002, he received the Litani River Project Award. In 2003, he joined the American University of Beirut (AUB) to pursue a Master of Engineering degree in Mechanical Engineering. Tony graduated from AUB with a 3.9 GPA; he subsequently joined the University of Tennessee Space Institute (UTSI) to pursue his doctoral studies in Mechanical Engineering. He is the recipient of the Lloyd W. Crawford fellowship for 2005 and 2007. He also received the UTSI Outstanding Graduate Research Assistant award in 2007. Tony is fluent in Arabic, French, and English and enjoys many extracurricular activities including volleyball, photography, and playing the guitar. He plans on pursuing a career dedicated to teaching and research in applied mathematics and engineering.